

Acknowledgements

This work was supported by USGS Contract 14-05-0001-21912.

My years at Caltech have been both rewarding and enjoyable. I have found the faculty to be genuinely interested in students' research and willing to treat us as **Source Characteristics of Recent and** advisor, got me interested in modeling **Historic Earthquakes in Central and** as come up with many good ideas. **Southern California: Results From** I help from Hiroo Kanamori and Dave Harkrath. **Forward Modeling** and Steve Pinnau reminded me how much fun physics can be.

I did enough of my own digging to **Thesis by** greatly appreciate the help I got from Cindy Arvesen, Will Freudenberger, and Steve Pinnau. Cindy also did the drafting for many of the figures in this thesis. Lian-Shu and Shawn's plotting programs made putting the last few figures together a lot easier.

In Partial Fulfillment of the Requirements

The students here have made my life more pleasant both in and out of the Seismo Lab. A few deserve special thanks: Joanne for spending many lunches listening to me blab on steam, the Promoters/Lovewaves softball team for lots of fun and for being patient while I was learning the intricacies of second base, my classmates (Horraine, Scott, Tom and Yu-Shen) for support and commiseration during Caltech and Philob. Barbara for being constantly helpful especially when I first arrived here and for "forcing" me to play softball, and Jon, who didn't protest too much when I dragged him to figure skating and the Philharmonic.

1990

(Submitted May 22, 1990)

And last, but not least, I would like to thank whoever it was who forgot to tell me that girls can't do math.

Acknowledgements

This work was supported by USGS Contract 14-08-0001-21912.

My years at Caltech have been both rewarding and enjoyable. I have found the faculty to be genuinely interested in students' research and willing to treat us as colleagues. Don Helmberger, my thesis advisor, got me interested in modeling earthquakes, and over the years has come up with many good ideas. At various times, I have also received help from Hiroo Kanamori and Dave Harkrider. Peter Goldreich and Sterl Phinney reminded me how much fun physics can be.

I did enough of my own digitizing to greatly appreciate the help I got from Cindy Arvesen, Will Freeman and Caroline Pinney. Cindy also did the drafting for many of the figures in this thesis. Lian-She and Shawn's plotting programs made putting the last few figures together a lot easier.

The students here have made my life more pleasant both in and out of the Seismo Lab. A few deserve special thanks: Joanne for spending many lunches listening to me blow off steam, the Tremors/Lovewaves softball team for lots of fun and for being patient while I was learning the intricacies of second base, my classmates (Lorraine, Scott, Tom and Yu-Shen) for support and commiseration during AMa101 and Ph106, Luciana for being constantly helpful especially when I first arrived here and for "forcing" me to play softball, and Jon, who didn't protest too much when I dragged him to figure skating and the Philharmonic.

And last, but not least, I would like to thank whomever it was who forgot to tell me that girls can't do math.

with non-identical subevents. **Abstract**

The long- and short-period body waves of a number of moderate earthquakes occurring in central and southern California recorded at regional (200 - 1400 km) and teleseismic ($> 30^\circ$) distances are modeled to obtain the source parameters—focal mechanism, depth, seismic moment, and source time history. The modeling is done in the time domain using a forward modeling technique based on ray summation. A simple layer over a half space velocity model is used with additional layers being added if necessary—for example, in a basin with a low velocity lid.

The earthquakes studied fall into two geographic regions: 1) the western Transverse Ranges, and 2) the western Imperial Valley. Earthquakes in the western Transverse Ranges include the 1987 Whittier Narrows earthquake, several offshore earthquakes that occurred between 1969 and 1981, and aftershocks to the 1983 Coalinga earthquake (these actually occurred north of the Transverse Ranges but share many characteristics with those that occurred there). These earthquakes are predominantly thrust faulting events with the average strike being east-west, but with many variations. Of the six earthquakes which had sufficient short-period data to accurately determine the source time history, five were complex events. That is, they could not be modeled as a simple point source, but consisted of two or more subevents. The subevents of the Whittier Narrows earthquake had different focal mechanisms. In the other cases, the subevents appear to be the same, but small variations could not be ruled out.

The recent Imperial Valley earthquakes modeled include the two 1987 Superstition Hills earthquakes and the 1969 Coyote Mountain earthquake. All are strike-slip events, and the second 1987 earthquake is a complex event

with non-identical subevents. *may have been more severely mislocated.* The *wave* In all the earthquakes studied, and particularly the thrust events, constraining the source parameters required modeling several phases and distance ranges. Teleseismic P waves could provide only approximate solutions. P_{nl} waves were probably the most useful phase in determining the focal mechanism, with additional constraints supplied by the SH waves when available. Contamination of the SH waves by shear-coupled PL waves was a frequent problem. Short-period data were needed to obtain the source time function.

In addition to the earthquakes mentioned above, several historic earthquakes were also studied. Earthquakes that occurred before the existence of dense local and worldwide networks are difficult to model due to the sparse data set. It has been noticed that earthquakes that occur near each other often produce similar waveforms implying similar source parameters. By comparing recent well studied earthquakes to historic earthquakes in the same region, better constraints can be placed on the source parameters of the historic events.

The Lompoc earthquake ($M=7$) of 1927 is the largest offshore earthquake to occur in California this century. By direct comparison of waveforms and amplitudes with the Coalinga and Santa Lucia Banks earthquakes, the focal mechanism (thrust faulting on a northwest striking fault) and long-period seismic moment (10^{26} dyne cm) can be obtained. The S-P travel times are consistent with an offshore location, rather than one in the Hosgri fault zone.

Historic earthquakes in the western Imperial Valley were also studied. These events include the 1942 and 1954 earthquakes. The earthquakes were relocated by comparing S-P and R-S times to recent earthquakes. It was found that only minor changes in the epicenters were required but that the

Coyote Mountain earthquake may have been more severely mislocated. The waveforms as expected indicated that all the events were strike-slip. Moment estimates were obtained by comparing the amplitudes of recent and historic events at stations which recorded both. The 1942 event was smaller than the 1968 Borrego Mountain earthquake although some previous studies suggested the reverse. The 1954 and 1937 earthquakes had moments close to the expected value. An aftershock of the 1942 earthquake appears to be larger than previously thought.

Abstract	1
Chapter 1: Source Complexity of the Whitby-Verde Earthquake	1
1.1 Method	8
1.2 Simple Source Solution	11
Solution	27
1.3 Stress Drop	28

	Table of Contents	
EQ2	109
4.4 Discussion and Conclusions	113
Acknowledgements	ii
Abstract	iii
General Introduction	1
5.3 Rebrations	121
Chapter 1: Source Complexity of the Whittier Narrows Earthquake	121
1.1 Introduction	5
1.2 Method	8
1.3 Simple Source Solution	11
1.4 Complex Source Solution	20
1.5 Stress Drop	26
1.6 Conclusions	28
References	144
Chapter 2: Source Characteristics of Earthquakes Occurring off the California Coast		
2.1 Introduction	30
2.2 Santa Lucia Banks Earthquakes	33
2.3 Point Mugu Earthquake	45
2.4 Santa Barbara Earthquake	50
2.5 Santa Barbara Island Earthquake	55
2.6 Crustal Thickness and Upper Mantle Velocity	56
2.7 Lompoc Earthquake	63
2.8 Discussion and Conclusions	70
Chapter 3: Aftershocks of the May 1983 Coalinga Earthquake		
3.1 Introduction	76
3.2 22 July	76
3.3 11 June	82
3.4 9 July	84
3.5 Station Studies	84
3.6 Discussion and Conclusions	88
Chapter 4: The 1987 Superstition Hills Earthquakes		
4.1 Introduction	90
4.2 Data Set	90
4.3 Teleseismic Modeling	100
EQ1	100

EQ2	105
4.4 Discussion and Conclusions.....	113
Chapter 5: Historic Earthquakes in the San Jacinto Fault Zone	
5.1 Introduction	117
5.2 Coyote Mountain Earthquake.....	119
5.3 Relocations.....	121
Teleseismic Data.....	121
Local Data.....	133
5.4 Moment Estimates	136
5.5 Discussion and Conclusions.....	138
Summary	142
References	144

General Introduction

at continuously operating stations. The historic earthquakes to recent ones which have been modeled at a large number of stations, more information about the historic earthquakes can be obtained than by direct modeling. Waveform modeling through the use of synthetic seismograms has, over the years, proven to be a useful tool in the study of earthquake sources and earth structure. In this thesis, a forward modeling technique based on ray summation is used to study earthquake sources. By modeling the waveforms and amplitudes of a large number of seismograms covering several distance and frequency ranges and including several phases when available, a small number of earthquake source parameters (focal mechanism, depth, seismic moment, and source time history) can be very well constrained. To obtain the best overall solution, trade-offs between the source parameters are sometimes necessary, but the effects of small changes in any of the source parameters are well known.

Two seismically active regions of California are studied. The western Transverse Ranges of south-central California and their offshore extension are dominated by thrust faulting on more or less east-west striking faults. The western Imperial Valley, in contrast, is dominated by strike-slip faulting on northwest striking faults with some additional events occurring on conjugate faults. An earthquake that occurred on 1 October 1987 is modeled. This earthquake, a complex

thrust event, is modeled. Because historic earthquakes were often recorded by only a few seismic stations, it is often difficult to tightly constrain the source parameters by modeling the available records. Historic earthquakes are those that occurred before the installation of the World Wide Standardized Seismic Network (WWSSN) in the early 1960's. The waveforms of historic and recent earthquakes that occurred in the same region are often very similar. By using data

at continuously operating stations and comparing the historic earthquakes to recent ones which have been modeled at a large number of stations, more information about the historic earthquakes can be obtained than by direct modeling.

Most of the earthquakes included in this thesis are in the magnitude 5 to 6.5 range or what are commonly referred to as moderate earthquakes. Although they rarely generate as much excitement as larger earthquakes, they are nevertheless important and can provide much information about the seismic nature of a region. One of the primary advantages of studying moderate earthquakes is that they are usually well recorded over a wide range of distances. They are small enough to be recorded on scale at regional distances, yet large enough to be seen teleseismically. Since moderate earthquakes are much more frequent than large earthquakes, they provide a larger data set for studies of the seismic characteristics of a particular region or fault. Since earthquakes of all sizes in a particular region are often very similar, understanding moderate earthquakes can lead to better forecasts of what to expect during a large earthquake, which is particularly important in regions where the last large earthquake was not well recorded.

In Chapter 1, the Whittier Narrows earthquake that occurred in the Los Angeles basin on 1 October 1987 is modeled. This earthquake, a complex thrust event, shows the pitfalls of using only teleseismic P-wave data or relying on local first motion data, and also illustrates the importance of using both long- and short-period data in determining the source time history.

In Chapter 2, five moderate offshore earthquakes that occurred between 1969 and 1981 are modeled. They are predominantly thrust events, and at least three have complex source time histories. Many regional and a few

teleseismic stations recorded all or most of these events. Travel time and amplitude data at these stations was used to obtain the crustal thickness and moho velocity along a number of paths, and to determine whether amplitude mismatches between data and synthetics show any consistency at a given station.

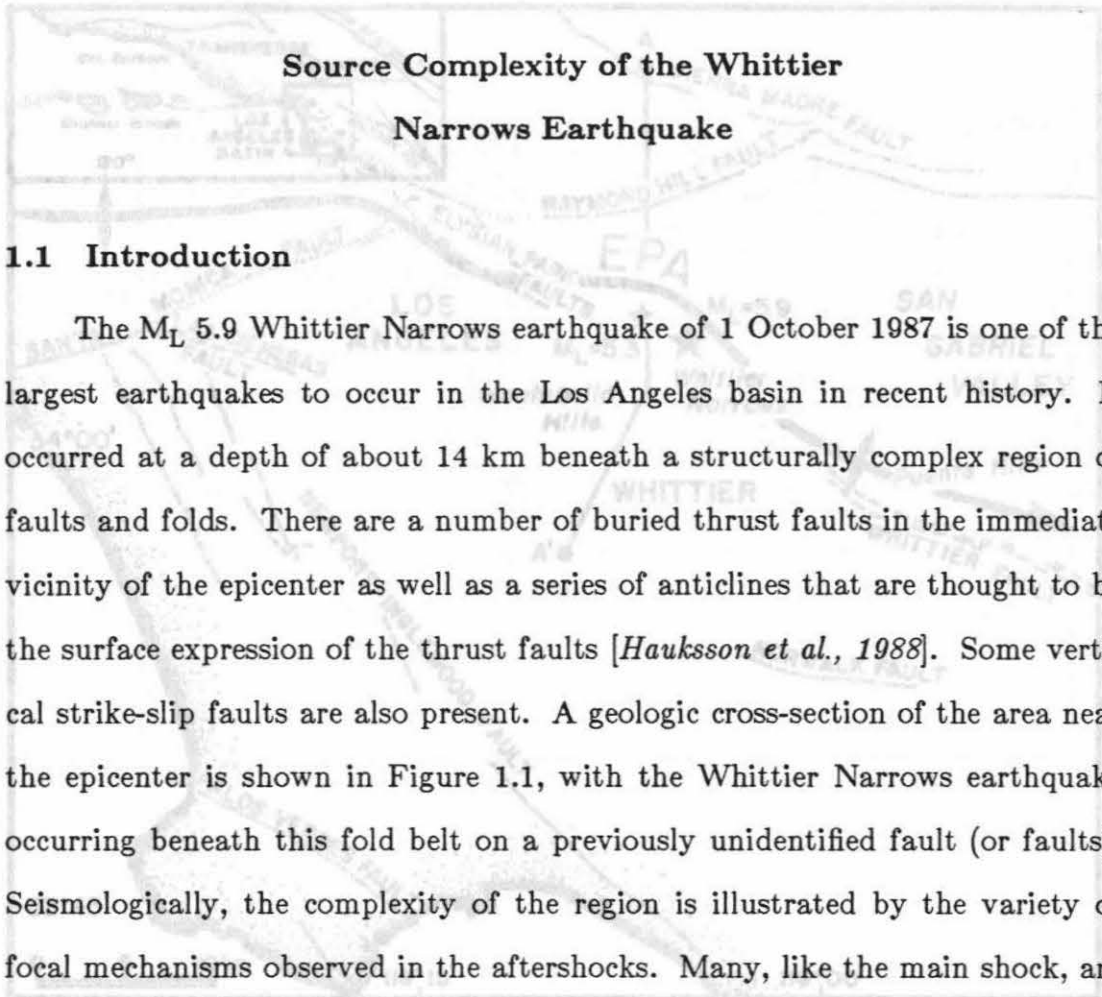
The 1927 Lompoc earthquake, whose location and magnitude have been the source of much debate, is also included in Chapter 2. Travel time data calibrated to recent well located events suggest that it occurred offshore and not on the Hosgri fault. The amplitudes, again calibrated to recent events, imply a magnitude of no more than 7.0. The waveforms are very similar to some recent thrust events, in particular the Coalinga and Santa Lucia Banks earthquakes.

Chapter 3 concentrates on three of the larger aftershocks of the May 1983 Coalinga earthquake. All are thrust events. Only the largest, which occurred on 22 July 1983, had sufficient short-period data to obtain a detailed source time function. It appears to be a northwest propagating rupture with the short-period energy release concentrated on two asperities. Moho velocities to regional stations were determined as in Chapter 2, and station amplitude patterns were also studied.

The two November 1987 Superstition Hills earthquakes are discussed in Chapter 4. The first is a simple left-lateral strike-slip event on a northeast trending fault. The second and larger event is a complex right-lateral strike-slip event on a northwest trending fault. The use of empirical Green's functions is demonstrated, in that to a first order, the waveforms of the complex event can be reproduced by adding the simple event to itself with a time delay.

The fifth and final chapter deals with historic earthquakes in the San Jacinto fault zone. The earthquakes are relocated by comparing the travel time differences of two or more phases (for example, S-P time) of the historic and recent well located earthquakes. Moment estimates for the historic events are determined by comparing the amplitudes to recent events at continuously operating stations. The 1942 and 1954 events appear to have been fairly well located, while the 1969 Coyote Mountain event which had been intended as a calibration event may have been mislocated. The amplitude data show that the magnitude of the 1942 event was overestimated while one of its aftershocks was greatly underestimated.

Chapter 1



1.1 Introduction

The M_L 5.9 Whittier Narrows earthquake of 1 October 1987 is one of the largest earthquakes to occur in the Los Angeles basin in recent history. It occurred at a depth of about 14 km beneath a structurally complex region of faults and folds. There are a number of buried thrust faults in the immediate vicinity of the epicenter as well as a series of anticlines that are thought to be the surface expression of the thrust faults [Hauksson *et al.*, 1988]. Some vertical strike-slip faults are also present. A geologic cross-section of the area near the epicenter is shown in Figure 1.1, with the Whittier Narrows earthquake occurring beneath this fold belt on a previously unidentified fault (or faults). Seismologically, the complexity of the region is illustrated by the variety of focal mechanisms observed in the aftershocks. Many, like the main shock, are on moderately dipping thrust faults, but there are also a number of strike-slip events on steeply dipping faults. The thrust faults are predominantly east-west striking but exhibit a variety of strikes including some that strike north-south. The strike-slip faults generally strike NNW [Hauksson and Jones, 1989]. Because the Whittier Narrows earthquake occurred near the edge of the Los Angeles basin and was a fairly deep event, the diving phases, P and S, should be virtually unaffected by the basin structure. The reflected phases, such as pP, sP and sS, may be distorted by the complex low-velocity layers near the surface. For this reason, we focus more attention on fitting the

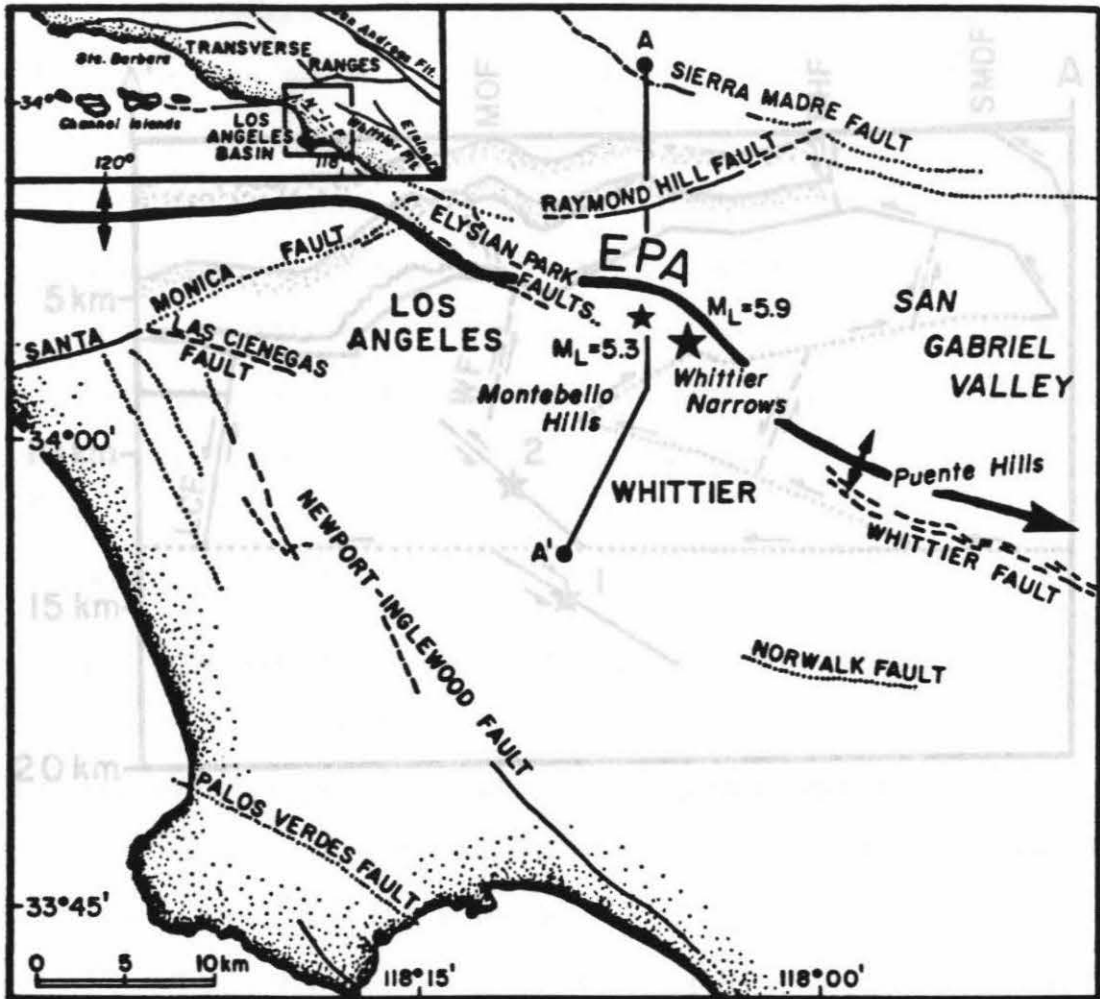


Figure 1.1b

An approximate cross-section along A-A'. LCF is the Las Cienegas fault, WF is the Whittier fault, RHF is the Raymond Hill fault, and SMDF is the Sierra Madre fault (modified from *Hauksson et al., 1988* and *Davis and Hayden, 1988*). The numbers 1 and 2 indicate the approximate locations of the first and second subevents which comprise the Whittier Narrows earthquake. Note that subevent 1 appears to occur below the detachment surface of *Davis and Hayden [1988]*.

direct arrivals initially and then add the basin structure to refine the solution.

A relatively large number of strong-motion records were obtained in the

Los Angeles area for this earthquake. The records are complex and vary

greatly in character. The records are complex and vary greatly in character.

The strong-motion records are complex and vary greatly in character.

The teleseismic records are complex and vary greatly in character.

The teleseismic records are complex and vary greatly in character.

The teleseismic records are complex and vary greatly in character.

The teleseismic records are complex and vary greatly in character.

The teleseismic records are complex and vary greatly in character.

The teleseismic records are complex and vary greatly in character.

The teleseismic records are complex and vary greatly in character.

The teleseismic records are complex and vary greatly in character.

The teleseismic records are complex and vary greatly in character.

The teleseismic records are complex and vary greatly in character.

The teleseismic records are complex and vary greatly in character.

The teleseismic records are complex and vary greatly in character.

The teleseismic records are complex and vary greatly in character.

The teleseismic records are complex and vary greatly in character.

The teleseismic records are complex and vary greatly in character.

The teleseismic records are complex and vary greatly in character.

The teleseismic records are complex and vary greatly in character.

The teleseismic records are complex and vary greatly in character.

The teleseismic records are complex and vary greatly in character.

The teleseismic records are complex and vary greatly in character.

The teleseismic records are complex and vary greatly in character.

The teleseismic records are complex and vary greatly in character.

The teleseismic records are complex and vary greatly in character.

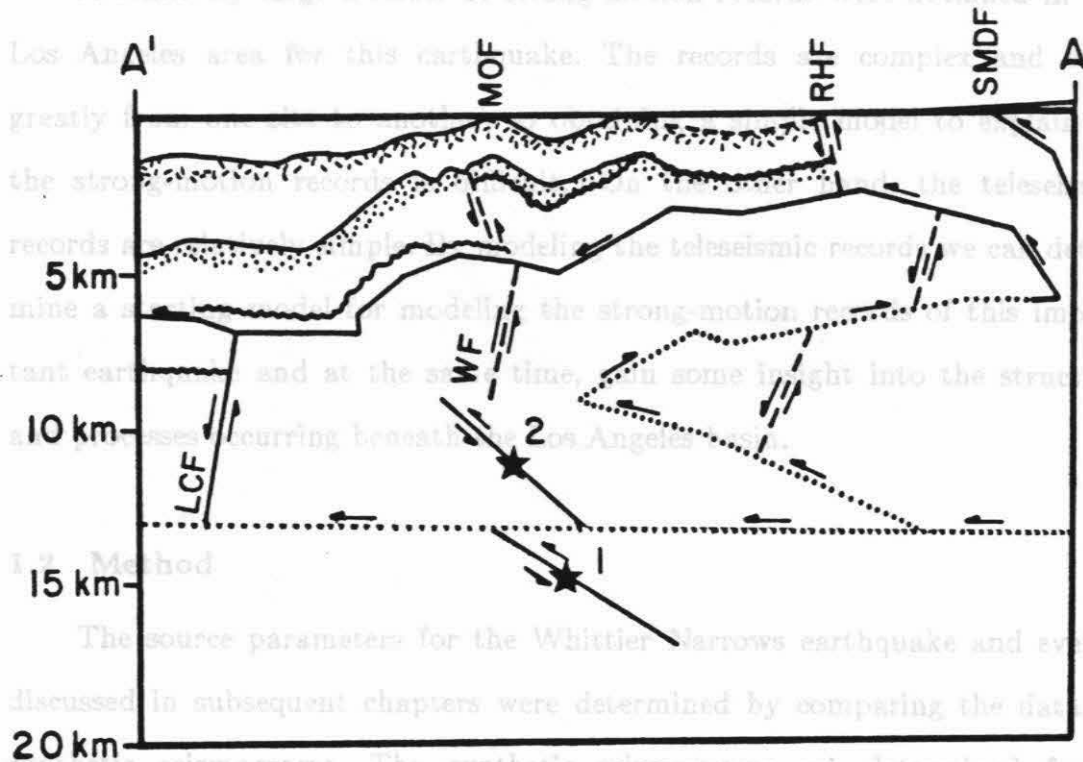


Figure 1.1b

An approximate cross-section along A-A'. LCF is the Las Cienegas fault, WF is the Whittier fault, RHF is the Raymond Hill fault, and SMDF is the Sierra Madre fault (modified from *Hauksson et al., 1988* and *Davis and Hayden, 1988*). Solid lines with arrows are thrust faults, dashed lines with arrows are other faults, and dotted lines with arrows are faults inferred from geologic data [*Davis and Hayden, 1988*]. The numbers 1 and 2 indicate the approximate locations of the first and second subevents which comprise the Whittier Narrows earthquake. Note that subevent 1 appears to occur below the detachment surface of *Davis and Hayden [1988]*.

direct arrivals initially and then add the basin structure to refine the solution.

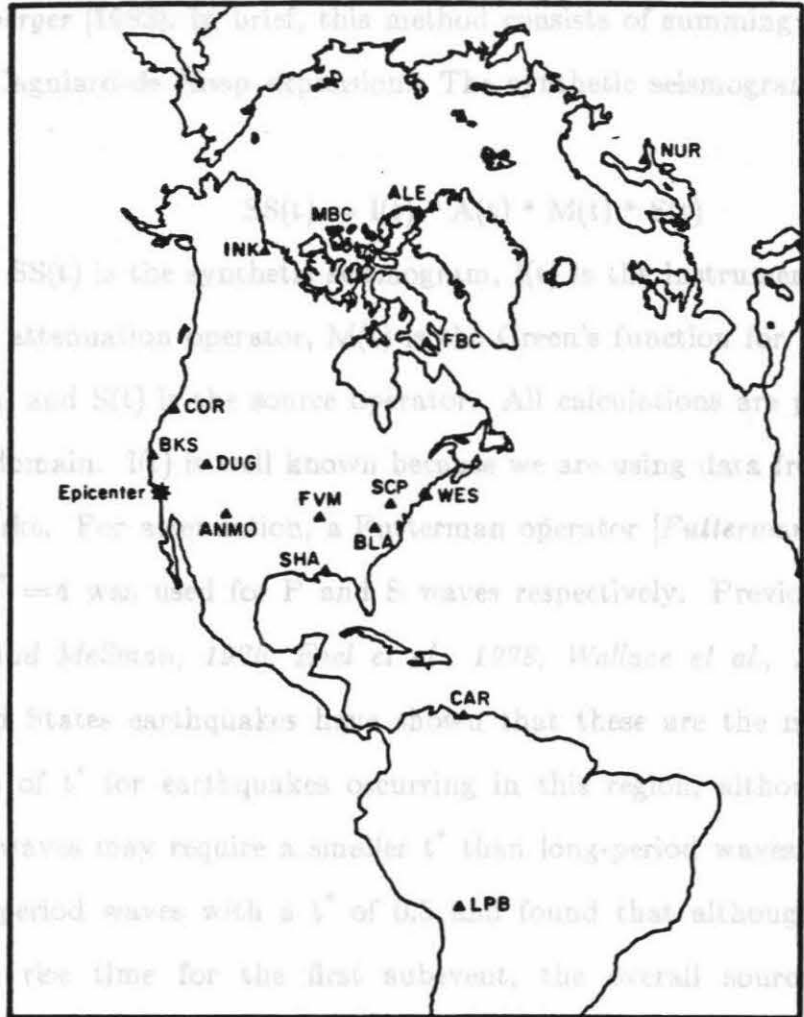
A relatively large number of strong-motion records were obtained in the Los Angeles area for this earthquake. The records are complex and vary greatly from one site to another, so obtaining a simple model to explain all the strong-motion records is difficult. On the other hand, the teleseismic records are relatively simple. By modeling the teleseismic records we can determine a starting model for modeling the strong-motion records of this important earthquake and at the same time, gain some insight into the structure and processes occurring beneath the Los Angeles basin.

1.2 Method

The source parameters for the Whittier Narrows earthquake and events discussed in subsequent chapters were determined by comparing the data to synthetic seismograms. The synthetic seismograms are determined for a number of sources until the fit in waveform and amplitude of the synthetics to the data cannot be further improved.

The Whittier Narrows earthquake was well recorded at both regional (2° - 12°) and teleseismic ($> 30^{\circ}$) distances. A broad sample of long- and short-period body wave data recorded by World-Wide Standard Seismograph Network (WWSSN), Canadian (Cdn), and Global Digital Seismograph Network (GDSN) stations (Figure 1.2) was collected and analyzed in this study. We have relatively good azimuthal coverage for this event. The analog data from the older networks (WWSSN and Cdn) were hand digitized and rotated to complement the GDSN data set. Stations within 10° of being naturally rotated were assumed to be already rotated.

The synthetic seismograms were calculated using a technique discussed in detail by Longston and Helmberger [1975], Helmberger and Engen [1980], and Helmberger [1982]. In brief, this method consists of summing generalized rays in a Cagniard-type ray-trace scheme. The synthetic seismograms are expressed as



where $SS(t)$ is the synthetic seismogram, $M(t)$ is the source function, $A(t)$ is the acceleration operator, $G(r, t)$ is Green's function, r is the wave propagation distance, and SCG is the source duration. All calculations are performed in the time domain. The source function $M(t)$ is known because we are using data from standardized networks. For station location, we use the IASPEI operator [Falterus, 1962] of $t^* = 1$ and $t^* = 4$ was used for P and S waves respectively. Previous studies [Burdick and McSwain, 1978; Engen et al., 1978; Wallace et al., 1981] of western United States earthquakes have shown that these are the most appropriate values of t^* for earthquakes occurring in this region, although short-period body waves may require a smaller t^* than long-period waves. We tested the short-period waves with a t^* of 0.5 and found that although we required a longer rise time for the first subevent, the overall source duration was unaffected. Hence we used the same values for both long- and short-period waves. The regional Green's functions are determined as by Helmberger and Engen [1980]. The teleseismic Green's functions are as described by Burdick and Helmberger [1978] for P waves and by Helmberger et al. [1985] for S waves.

Figure 1.2

Map of stations modeled. The star is at the earthquake epicenter.

Initially, we ignore the complex basin velocity structure and use a simple half-space crustal model as experience [Harzell and Helmberger, 1982] has shown that long-period body waves do not appear to be seriously affected by

The synthetic seismograms were calculated using a technique discussed in detail by *Langston and Helmberger [1975]*, *Helmberger and Engen [1980]*, and *Helmberger [1983]*. In brief, this method consists of summing generalized rays in a Cagniard-de Hoop expansion. The synthetic seismograms are expressed as

$$SS(t) = I(t) * A(t) * M(t) * S(t)$$

where $SS(t)$ is the synthetic seismogram, $I(t)$ is the instrument response, $A(t)$ is the attenuation operator, $M(t)$ is the Green's function for the wave propagation, and $S(t)$ is the source operator. All calculations are performed in the time domain. $I(t)$ is well known because we are using data from standardized networks. For attenuation, a Futterman operator [*Futterman, 1962*] of $t^* = 1$ and $t^* = 4$ was used for P and S waves respectively. Previous studies [*Burdick and Mellman, 1976; Ebel et al., 1978; Wallace et al., 1981*] of western United States earthquakes have shown that these are the most appropriate values of t^* for earthquakes occurring in this region, although short-period body waves may require a smaller t^* than long-period waves. We tested the short-period waves with a t^* of 0.5 and found that although we required a longer rise time for the first subevent, the overall source duration was unaffected. Hence we used the same values for both long- and short-period waves. The regional Green's functions are determined as by *Helmberger and Engen [1980]*. The teleseismic Green's functions are as described by *Burdick and Helmberger [1978]* for P waves and by *Helmberger et al. [1985]* for S waves.

Initially, we ignore the complex basin velocity structure and use a simple half-space crustal model as experience [*Hartzell and Helmberger, 1982*] has shown that long-period body waves do not appear to be seriously affected by

the basins. Short-period reflected phases, however, can be affected by the presence of a basin. We model the long- and then the short-period data using the half-space model. This solution is used as the starting point in remodeling the short-period data with the basin structure included. Finally, the long-period waves are rechecked to make sure they are compatible with the short-period and basin structure solution. The P wave velocities and layer thicknesses used in the basin velocity model are those of *Hauksson and Jones* [1989] determined by a refraction experiment performed shortly after the Whittier Narrows earthquake. We added densities and S wave velocities which should be appropriate for these P wave velocities, but which have not been verified experimentally. The velocity model is shown in Table 1.1.

1.3 Simple Source Solution

The focal mechanism for the Whittier Narrows earthquake determined from first motion data recorded by the local Caltech and USC networks is strike (θ)= 270° , dip (δ)= 25° N and rake (λ)= 90° [*Hauksson et al., 1988*]. I used this mechanism as a starting point and, by following a trial-and-error procedure, made adjustments in this model to obtain the best fit to the data.

Frequently, source parameters are determined from teleseismic P waves only. As was noted by *Wallace and Helmberger* [1982], teleseismic P waves are not particularly useful in determining the source parameters of moderately dipping thrust or normal faults, as they are relatively insensitive to changes in the fault geometry. Due to the moderate dip and predominantly dip-slip motion, all teleseismic P waves observed have the same first motion and none are near enough to the nodal lines of the focal sphere to be affected by small to moderate changes in dip or rake or even larger changes in strike. Figure

Table 1.1
Velocity Model

P-Wave Velocity (km/sec)	S-Wave Velocity (km/sec)	Density (g/cm ³)	Thickness (km)
3.3	2.0	2.0	2.0
4.1	2.5	2.4	3.5
6.0	3.2	2.6	7.5
6.4	3.5	2.7	3.0
6.7	3.7	2.9	14.0
7.9	4.6	3.6	-

1.3 shows the synthetic, data and station distribution for long-period P waves. The synthetics were calculated using the best point source solution determined by P_{nl} and SH modeling, but any moderately dipping roughly E-W thrust mechanism would give equally good P waveform results. Note that the teleseismic P waves were very useful, however, in estimating the source strength and in determining the depth of the source. Based on the timing of the zero crossovers at the beginning of the record (width 'ab' in Figure 1.4), a depth of 14 km was obtained for a source duration of 2 sec. The calculated depth increases as we decrease the source duration but will be within 2 km of our estimated depth unless an unreasonably large or small source duration is assumed.

The P_{nl} waves can be diagnostic in distinguishing not only between strike-slip and dip-slip events but also in determining the relative amounts of each [Helmberger and Engen, 1980]. This technique has proven useful in constraining the source parameters of the Whittier Narrows earthquake. P_{nl} first motions at stations north of the epicenter (COR and BKS) constrain the maximum dip of the fault plane to be between 40° and 45° , but all P_{nl} data are compatible with a shallower dip. The P_{nl} waves are less sensitive to strike but suggest a roughly east-west strike. The P_{nl} synthetics and data for the best point source solution are shown in Figure 1.5. (upper trace).

SH waves were used to further constrain the solution. Unfortunately, the SH data set is much smaller than the P data set because most stations to the north and NNW of the epicenter (COL, MBC, INK) have strong shear-coupled PL waves which obscure the small SH arrivals. The same problem occurred in an earlier study of the 1971 San Fernando earthquake [Langston, 1978] and is a common difficulty in modeling thrust events. At most other azimuths,

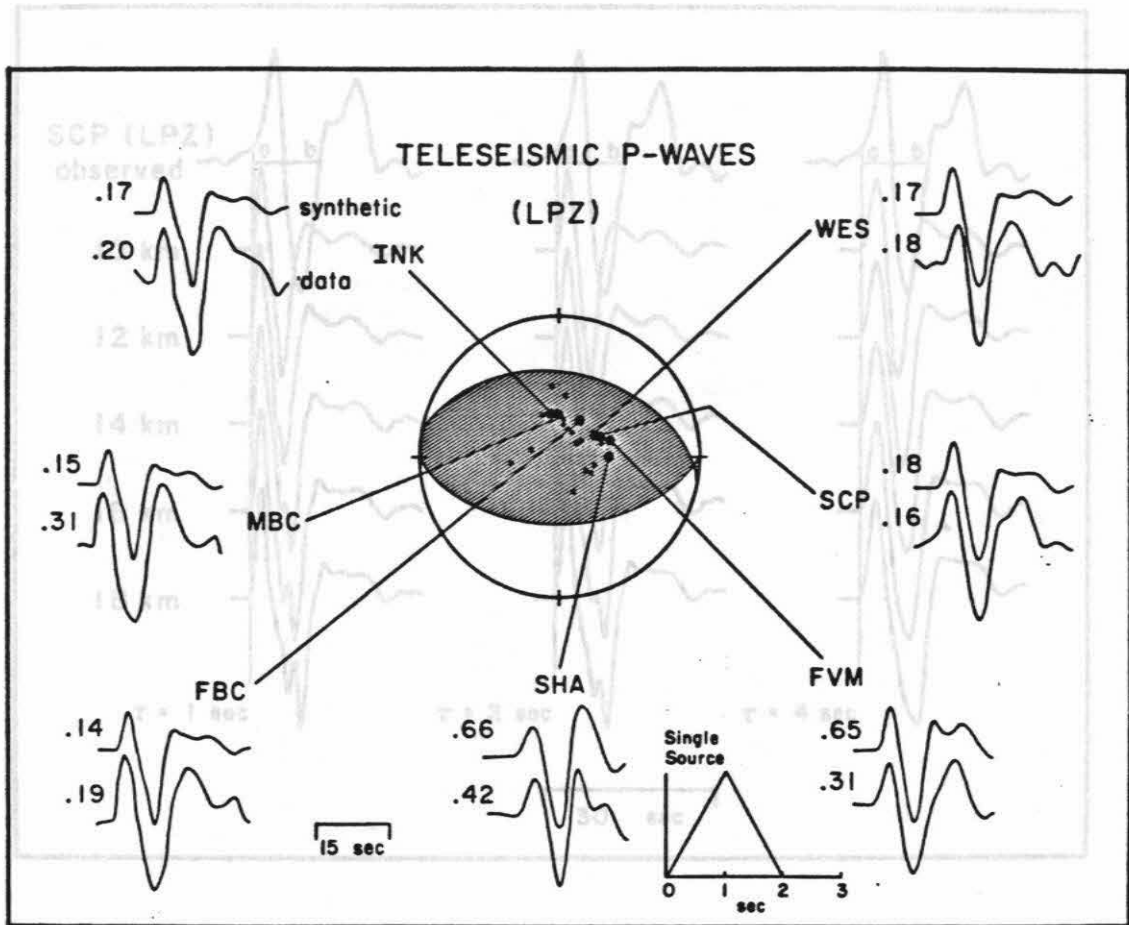


Figure 1.3

Teleseismic P data (lower trace) and synthetics (upper trace). The double source solutions are not shown as they are not significantly different from the single source solutions. The large dots represent stations for which we show results. The small dots represent stations for which we have data but have not modeled in detail as they contain no new information. Amplitudes are in units of 10^{-3} cm and are computed for a moment of 1.1×10^{25} dyne cm with the instrument gain removed. The source time function shown is for the single source mechanism.

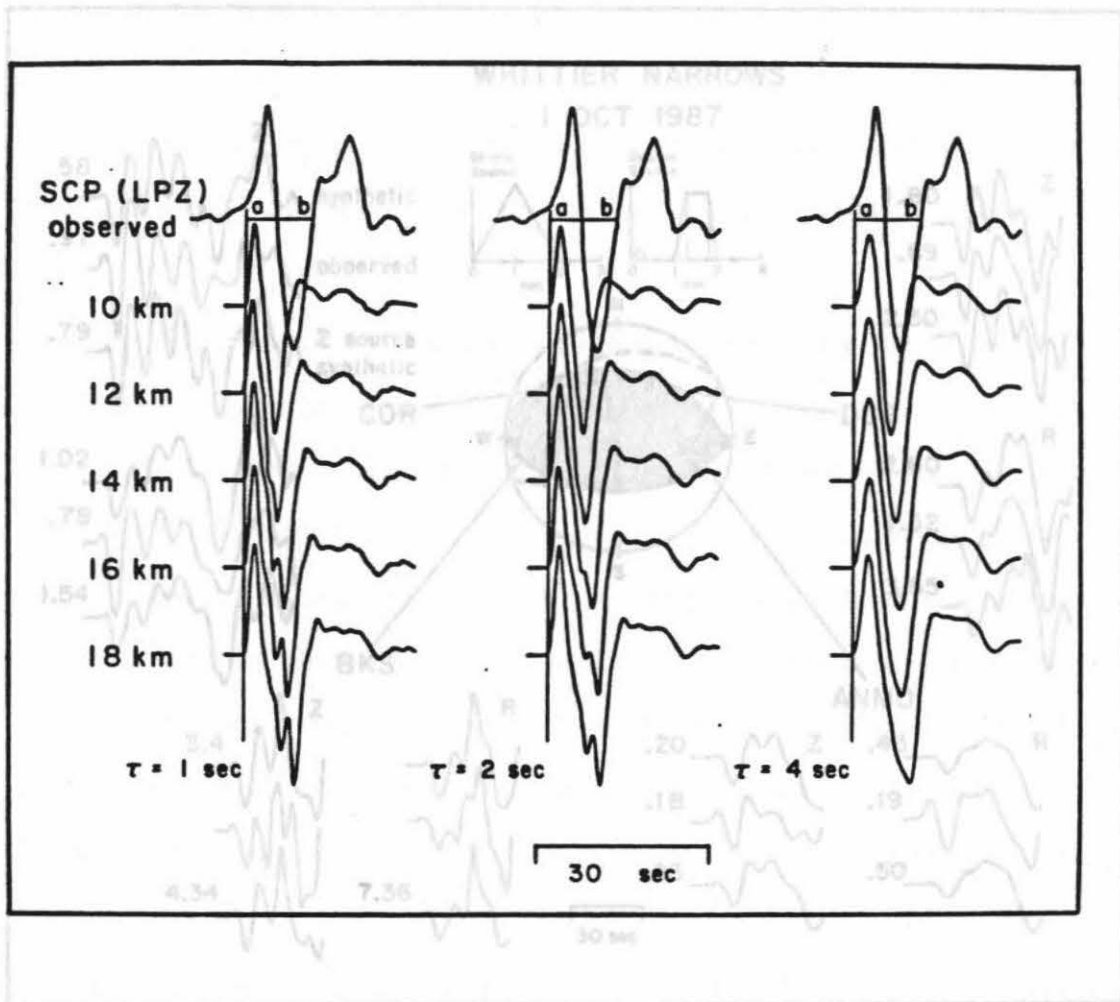


Figure 1.4

Teleseismic P waves (at SCP) modeled for various depths and source durations (τ). Depth increases from top to bottom; duration increases from left to right. In all cases, the time function used was an isosceles triangle with a rise and fall each equal to 0.5τ . The source depth is determined by fitting the width ab .

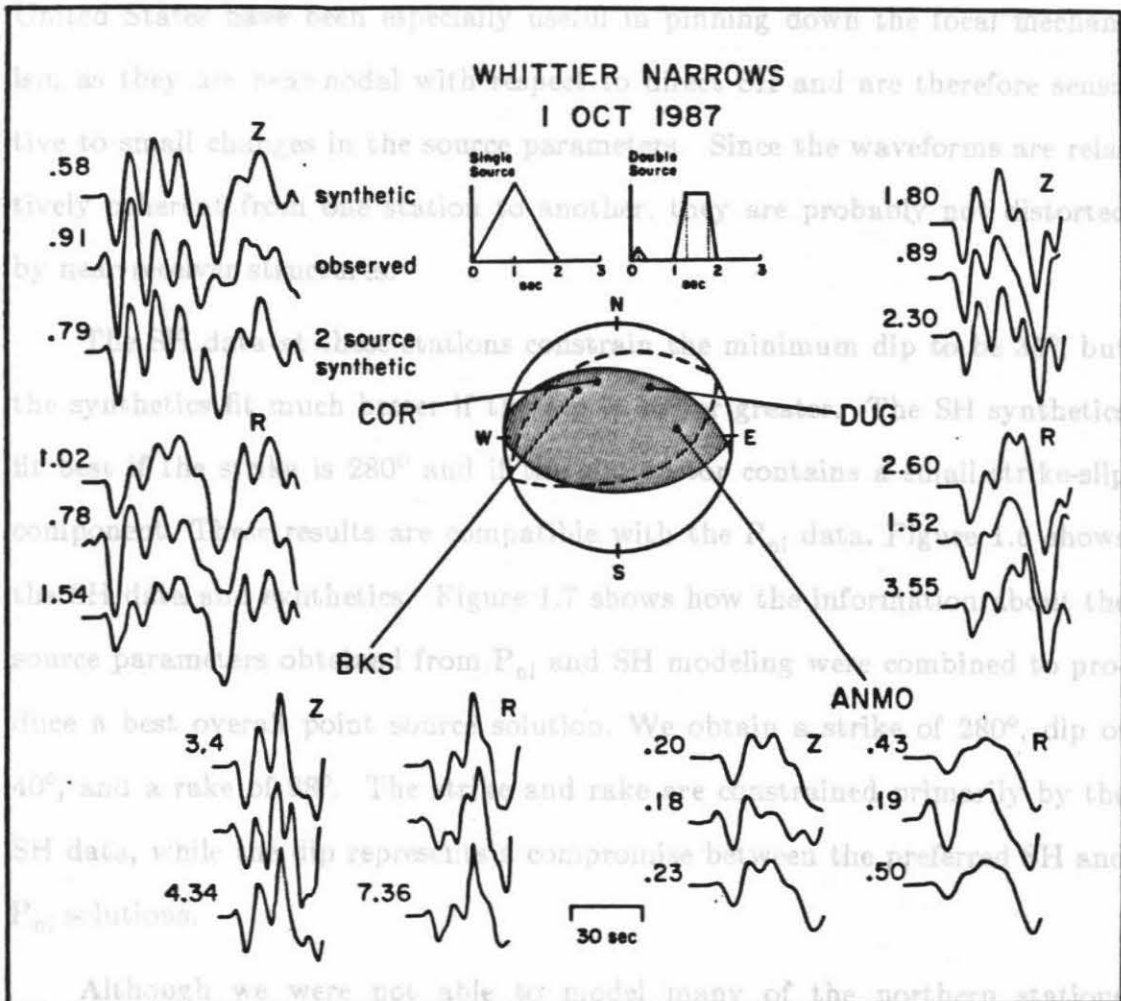


Figure 1.5

P_{nl} data and synthetics. The upper trace is the single source synthetic, the middle is the data, and the lower is the double source synthetic. All amplitudes are given as 10^{-3} cm and have the instrument gain removed. The solid focal mechanism is for the single source or second subevent. The dotted focal mechanism is for the first subevent. The single source time function is an approximate solution; the double source time function was obtained by modeling short-period records.

point source solution we obtain a seismic moment of 1.1×10^{25} dyne cm. We obtain a similar moment whether we use the complete data set or only one phase. The moment determined from only

however, we do have reasonably good SH data. Stations in the eastern United States have been especially useful in pinning down the focal mechanism as they are near-nodal with respect to direct SH and are therefore sensitive to small changes in the source parameters. Since the waveforms are relatively coherent from one station to another, they are probably not distorted by near-receiver structures.

The SH data at these stations constrain the minimum dip to be 35° , but the synthetics fit much better if the dip is 40° or greater. The SH synthetics fit best if the strike is 280° and if the slip vector contains a small strike-slip component. These results are compatible with the P_{nl} data. Figure 1.6 shows the SH data and synthetics. Figure 1.7 shows how the information about the source parameters obtained from P_{nl} and SH modeling were combined to produce a best overall point source solution. We obtain a strike of 280° , dip of 40° , and a rake of 98° . The strike and rake are constrained primarily by the SH data, while the dip represents a compromise between the preferred SH and P_{nl} solutions.

Although we were not able to model many of the northern stations because of PL contamination, the SV/SH ratios did provide an additional check on the strike. If we assume a dip of 40° , then based solely on the SV/SH amplitude ratio at all available stations we obtain a mean strike of 275° and a median strike of 279° , which is close to what is predicted by the waveform modeling.

By comparing the observed peak body wave amplitudes with the synthetic amplitudes for the best point source solution we obtain a seismic moment of 1.1×10^{25} dyne cm. We obtain a similar moment whether we use the complete data set or only one phase. The moment determined from only

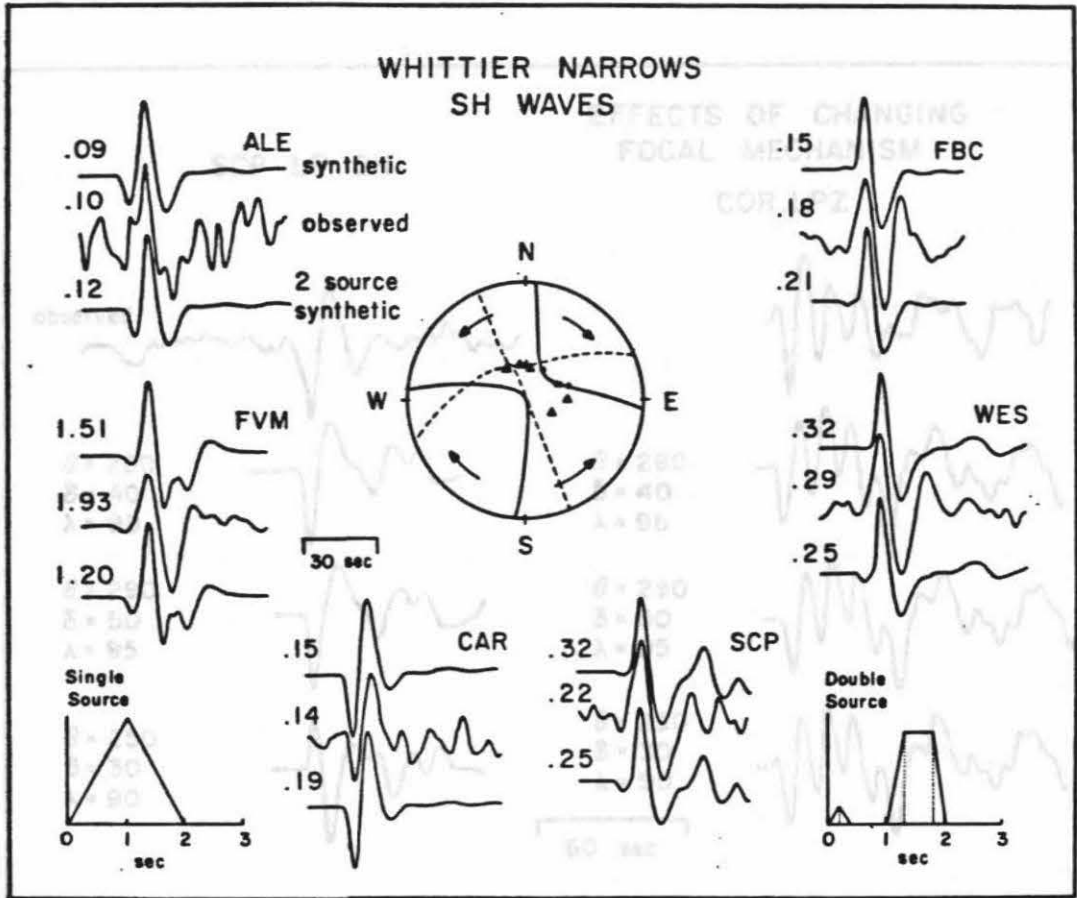


Figure 1.6

The effect of various focal mechanisms on the observed waveform at CAR and SCP. The upper trace is the observed waveform. The first synthetic is the best point source solution. The second synthetic gives reasonably good results at SCP, but the steep dip results in an incorrect first motion at CAR. The final synthetic is a relatively

Telesismic SH data and synthetics. The format is the same as for Fig. 1.5.

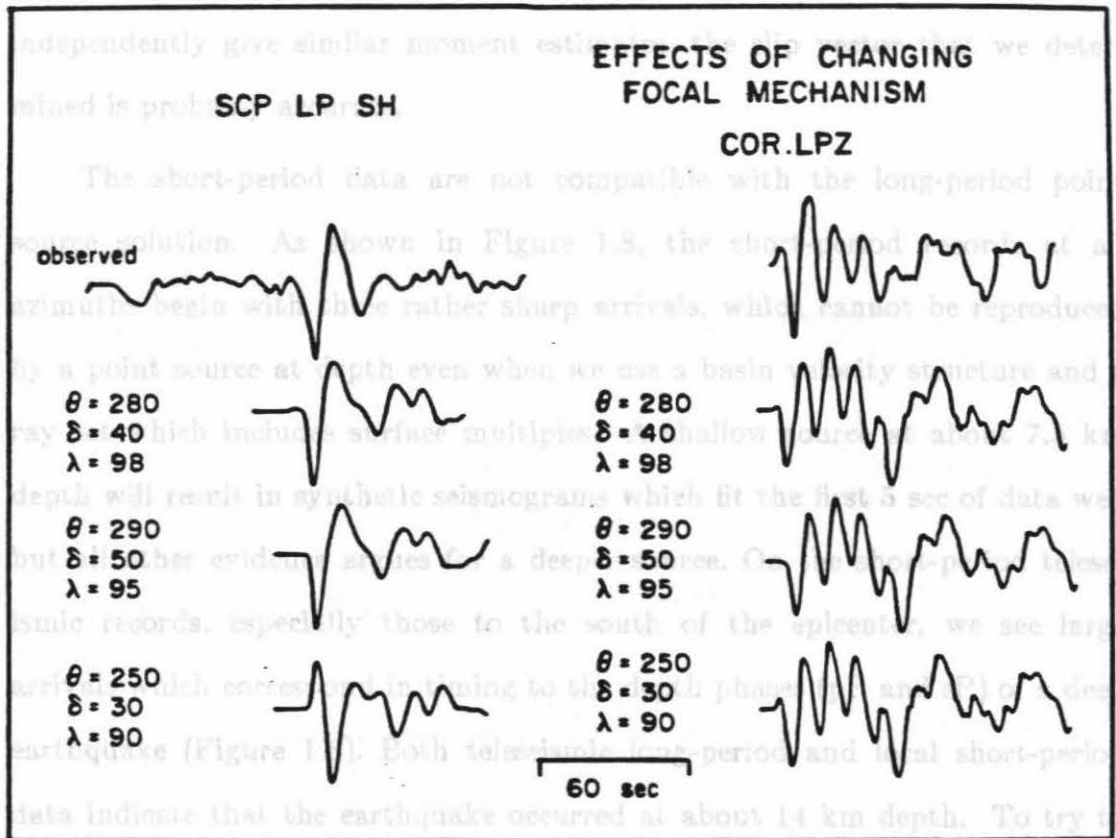


Figure 1.7

The effect of various focal mechanisms at COR and SCP. The upper trace is the observed waveform. The first synthetic is the best point source solution. The second synthetic gives reasonably good results at SCP, but the steep dip results in an incorrect first motion at COR. The final synthetic is a solution which fit all the P_{nl} data well but gave very poor SH fits due to the shallow dip and southwesterly strike.

teleseismic P waves is 1.2×10^{25} . That determined from teleseismic SH waves is 1.1×10^{25} and that from P_{nl} waves is 0.94×10^{25} (1.1×10^{25} if we consider only the vertical component). Since teleseismic and regional waves considered independently give similar moment estimates, the slip vector that we determined is probably accurate.

The short-period data are not compatible with the long-period point source solution. As shown in Figure 1.8, the short-period records at all azimuths begin with three rather sharp arrivals, which cannot be reproduced by a point source at depth even when we use a basin velocity structure and a ray set which includes surface multiples. A shallow source at about 7.5 km depth will result in synthetic seismograms which fit the first 5 sec of data well but all other evidence argues for a deeper source. On the short-period teleseismic records, especially those to the south of the epicenter, we see large arrivals which correspond in timing to the depth phases (pP and sP) of a deep earthquake (Figure 1.8). Both teleseismic long-period and local short-period data indicate that the earthquake occurred at about 14 km depth. To try to improve the fit of the short-period synthetics, we modeled the Whittier Narrows earthquake as a double event.

Figure 1.8

1.4 Complex Source Solution

By using a two source solution, we are able to obtain a solution which explains the short-period data and which also models the long-period data better than does a single source solution. The first subevent has a pure thrust mechanism: $\theta=250^\circ$, $\delta=30^\circ$, $\lambda=90^\circ$, $h=17-18$ km, and $M_0=0.23 \times 10^{25}$ dyne cm. The second subevent occurred 1.2 sec later and has the following parameters: $\theta=280^\circ$, $\delta=40^\circ$, $\lambda=98^\circ$, $h=11-12$ km, and $M_0=1.2 \times 10^{25}$ dyne cm.

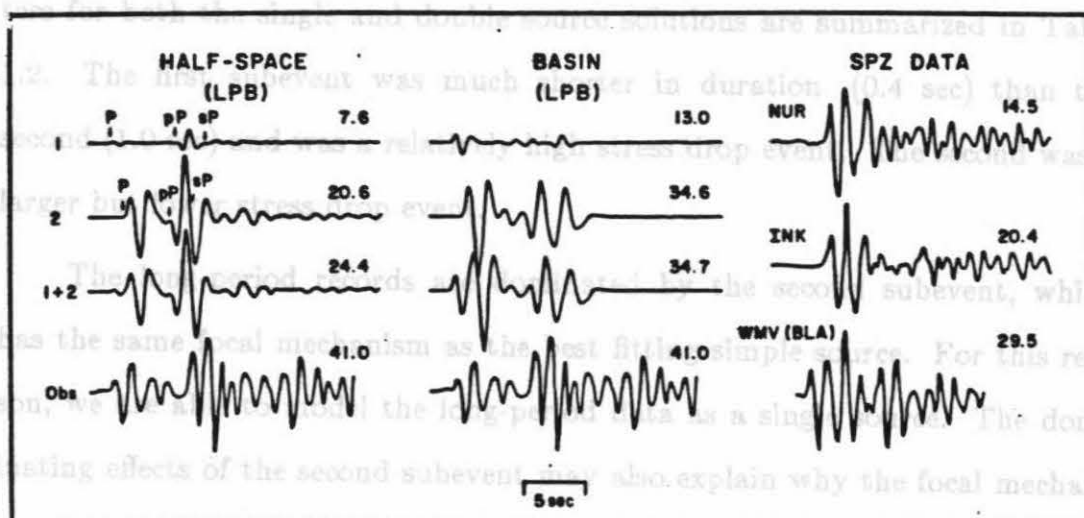


Figure 1.8

Two source solution at LPB (Bolivia). The amplitudes of the subevents are at the correct relative scale and are given in units of 10^{-6} cm. The far left synthetics are for a half-space velocity model; the center model is for a basin velocity structure. The far right column shows the short-period data at other stations.

1.8 shows synthetics for the two subevents as well as the combination of the

These results were obtained for the half-space model. When we add the low-velocity layers of the Los Angeles basin, the depth of the first subevent decreases to 15 km, which is in close agreement with the depth determined from local data [Hauksson and Jones, 1989], while the depth of the second subevent is unchanged but better constrained- 12 km gives a better fit than does 11 km. The time separation is decreased to 1.0 sec. The source parameters for both the single and double source solutions are summarized in Table 1.2. The first subevent was much shorter in duration (0.4 sec) than the second (1.0 sec) and was a relatively high stress drop event. The second was a larger but lower stress drop event.

The long-period records are dominated by the second subevent, which has the same focal mechanism as the best fitting simple source. For this reason, we are able to model the long-period data as a single source. The dominating effects of the second subevent may also explain why the focal mechanism from local first motion data is incapable of reproducing the overall characteristics of the teleseismic data event though it produces correct first motions at teleseismic distances. A double source solution improves some synthetics and does not adversely affect any. At regional distances the amplitude of the synthetic P_n or first arrival fits the observed P_n arrival more closely (Figure 1.5) for the complex source solution. At teleseismic distances, the S/sS relative amplitudes are improved at stations on the east coast. Teleseismic P waves are not noticeably changed when a two source solution is used. Figure 1.9 shows synthetics for the two subevents as well as the combination of the two at SCP(SH) and DUG(P_{nl}).

Because of the dominance of the second source, the first source is probably not as well constrained as the second. A strike rotation of slightly less

Table 1.2

Source Parameters

	strike (deg)	dip (deg)	rake (deg)	depth (km)	M_0 (10^{26} dyne cm)	δ_1 (sec)	δ_2 (sec)	δ_3 (sec)	delay (sec)
single source	280	40	98	14	1.1	1.0	0.0	1.0	0
subevent 1	250	30	90	15	0.23	0.2	0.0	0.2	0
subevent 2	280	40	98	12	1.2	0.32	0.52	0.17	1

than 30° will produce reasonably good synthetics at most stations. A 30° rotation is the minimum rotation that will produce the correct first motion at TUC, the only observed dilatational first motion. A greater rotation starts to produce SH synthetics which do not fit well. A dip of 30° produces better P_{nl} first motion amplitudes than a steeper dip, while a shallower dip causes the SH first motions to be too large. The subevent is mainly thrust, but it could have a small strike-slip component.

At short periods the early part of the record is dominated by the first subevent; the later part is dominated by the second. Because of the sharpness of the first P arrival (Figure 1.9), the first source is required to have a short rise time. We obtain a triangular time function with a rise and fall of 0.2 sec each. A longer rise time does not give the sharp first arrival that is observed, although a shorter rise time does not have any noticeable effect. The time function for the second source was determined by beginning with the $\delta t_1 : \delta t_2 : \delta t_3$ ratio of an Italian earthquake with similar short-period waveforms [Cipar, 1981] and adjusting the absolute values to obtain the best fit. We obtained a trapezoidal time function with $\delta t_1 = 0.32$ sec, $\delta t_2 = 0.52$ sec, $\delta t_3 = 0.17$ sec. The depths of the two subevents are constrained by the arrival times of pP and sP on the short-period records. The addition of the two sources for the short-period waves is shown in Figure 1.8.

The moment ratio of the subevents has two primary constraints. First, if the moment of the first subevent is any greater than $1/5$ that of the second, many of the SH synthetics will not fit the data. For example, at east coast stations the direct S phase will be much too large with respect to sS. Second, if the ratio is smaller than $1/5$, the initial P arrival will be too small at short periods. The total moment for the double source is approximately 27% larger

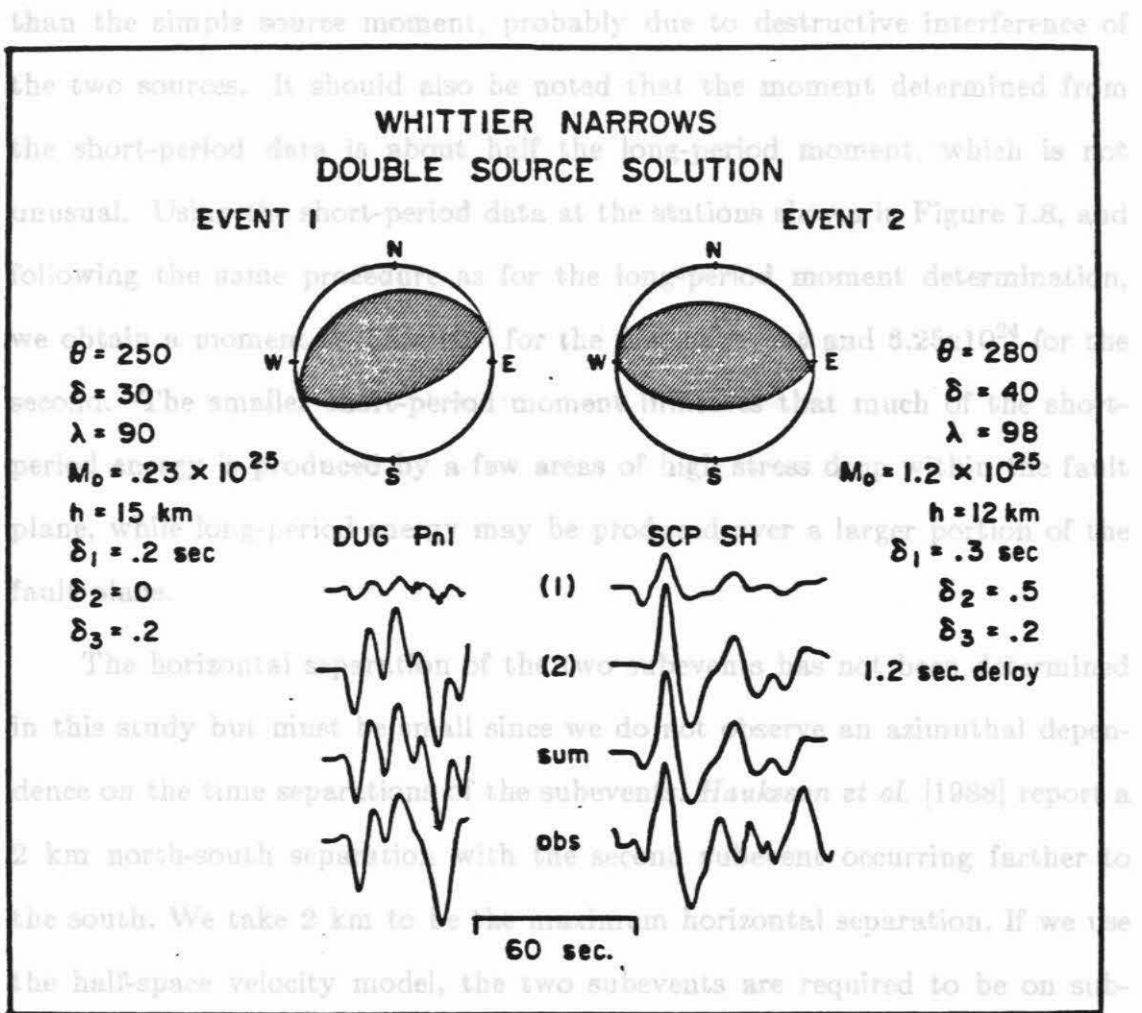


Figure 1.9

Two source solution at DUG and SCP. The amplitudes of the subevents are at the correct relative scale.

than the simple source moment, probably due to destructive interference of the two sources. It should also be noted that the moment determined from the short-period data is about half the long-period moment, which is not unusual. Using the short-period data at the stations shown in Figure 1.8, and following the same procedure as for the long-period moment determination, we obtain a moment of 1.25×10^{24} for the first subevent and 6.25×10^{24} for the second. The smaller short-period moment indicates that much of the short-period energy is produced by a few areas of high stress drop within the fault plane, while long-period energy may be produced over a larger portion of the fault plane.

The horizontal separation of the two subevents has not been determined in this study but must be small since we do not observe an azimuthal dependence on the time separations of the subevents. *Hauksson et al.* [1988] report a 2 km north-south separation with the second subevent occurring farther to the south. We take 2 km to be the maximum horizontal separation. If we use the half-space velocity model, the two subevents are required to be on sub-parallel faults due to the moderate dip of the fault planes and the relatively large vertical separation compared to the horizontal separation. When we add the basin velocity structure, the vertical separation decreases, and it is possible to place both subevents on a single listric fault.

1.5. Stress Drop

Due to the difficulty in directly determining fault area and dislocation by the forward modeling technique used to determine the other source parameters, we have made only preliminary attempts to calculate stress drop. We define the fault area as the area of the aftershock zone and calculate

dislocation using the relation $M_0 = \mu Sd$ while the complete rupture process $M_0 = \mu Sd$ where M_0 is the seismic moment, μ is the rigidity, S is the fault area, and d is the average dislocation. We use $\mu = 3 \times 10^{11}$ dyne cm^{-2} since the earthquake was deep and probably occurred in bedrock. The aftershock zone defines a circular plane roughly 4 km in diameter [Hauksson and Jones, 1989] which gives a fault area of 12.6 km^2 . From Kanamori and Anderson [1975] and Keilis-Borok [1959] we obtain the equation for stress drop on a circular fault $\Delta\sigma = 7\pi\mu d/16a$ where $\Delta\sigma$ is the stress drop and a is the fault radius. We obtain a stress drop of 750 bars for the double source combined moment (600 bars if we use the simple source moment).

Similar stress drop estimates are obtained if we compare the moment and source duration of the Whittier Narrows earthquake to other southern California earthquakes for which the stress drop is known. This estimate is independent of the choice of fault area. By extrapolating from the moment versus duration plot of Cohn *et al.*, [1982] we obtain a stress drop of 500-600 bars for the earthquake as a whole, and estimates for the subevents considered separately are in the kilobar range.

The stress drop obtained from the short-period time function or from the aftershock zone is not necessarily representative of the complete rupture process. Lin and Stein [1989] obtain a geodetic stress drop of 155 ± 43 bars for a fault area of 27 ± 7.5 km^2 as their preferred solution. Note that if we use their fault area determination we obtain a stress drop level similar to theirs.

A review of detailed short-period modeling efforts indicates that it is common to find disparities in the fault parameters of subevents. Earthquakes

often begin with one or more asperity ruptures (or high stress drop subevents) while the complete rupture process is a lower stress drop event. Stress drop estimates of southern California earthquakes differ by as much as an order of magnitude depending on whether the whole event or subevents are considered. Examples include the 1968 Borrego Mountain [Ebel and Helmberger, 1982], 1978 Santa Barbara [Wallace et al., 1981], and 1979 Imperial Valley [Hartzell and Helmberger, 1982] events. Although subevents do not necessarily give good stress drop estimates for the overall rupture process, they have proven essential in explaining the strong-motion data in previous efforts and we expect the Whittier Narrows event to yield similar results.

1.6 Conclusions

The Whittier Narrows earthquake consisted of two subevents separated in time by 1.0 sec. The best fitting fault plane solution for the first subevent has a strike of 250° , a dip of 30° and a rake of 90° . It had a moment of 0.23×10^{25} dyne cm and occurred at a depth of 15 km. The second subevent had a strike of 280° , a dip of 40° , and rake of 98° . It was five times larger than the first subevent ($M_0 = 1.2 \times 10^{25}$) and occurred at a depth of 12 km. The subevents probably occurred on a north-dipping listric fault. The depth and location of the first subevent determined in this study are similar to those determined in other studies [Hauksson and Jones, 1989] from analysis of high-frequency array data. The local array solution will not reproduce the observed teleseismic waveforms although it does give the correct first motions. Since the second subevent dominates the waveforms and the time separation of the two subevents is an order of magnitude smaller than the periods studied, the long-period data can be modeled as a single event with a focal

mechanism identical to that of the second subevent but with a depth of 14 km and a moment of 1.1×10^{25} . The short-period data require a double source solution, and in retrospect, it was found that the long-period synthetic waveforms were improved by the two source solution. The source parameters should be well constrained due to the number of phases modeled and stations used, but there are some trade-offs involved in the modeling procedure.

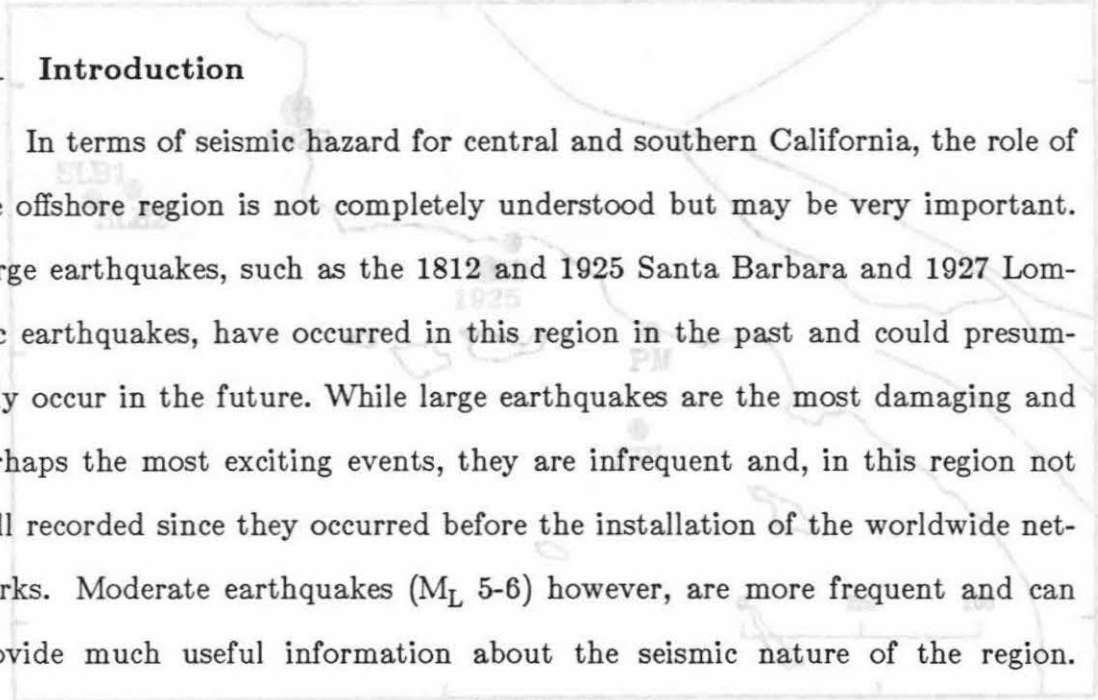
The depth and source separation are influenced by the velocity model used. Our final solution is based on a layered velocity structure appropriate for the area in which the earthquake occurred [*Hauksson and Jones, 1989*]. The initial modeling procedure employed a less complex model and obtained source depths of 17-18 km and 11-12 km respectively for the first and second subevents and a source separation of 1.2 sec. The dip of the second subevent represents a compromise between the preferred dips of the SH and P_{nl} waveforms. Although both can be well modeled by a 40° dip, the P_{nl} waveforms fit slightly better with a shallower dip and the SH waveforms with a slightly steeper dip.

In this chapter I will discuss the results of the modeling procedure.

Chapter 2

Source characteristics of earthquakes occurring off the California coast

2.1 Introduction



In terms of seismic hazard for central and southern California, the role of the offshore region is not completely understood but may be very important. Large earthquakes, such as the 1812 and 1925 Santa Barbara and 1927 Lompoc earthquakes, have occurred in this region in the past and could presumably occur in the future. While large earthquakes are the most damaging and perhaps the most exciting events, they are infrequent and, in this region not well recorded since they occurred before the installation of the worldwide networks. Moderate earthquakes (M_L 5-6) however, are more frequent and can provide much useful information about the seismic nature of the region. Often these earthquakes are not studied in detail.

In this chapter, I model the body waves of five moderate nearshore earthquakes which occurred in the western extension of the Transverse Ranges (roughly at the latitude of the 'big bend' in the San Andreas fault) to determine their source parameters. The events consist of the 1973 Point Mugu, 1978 Santa Barbara, 1981 Santa Barbara Island, and two 1969 Santa Lucia Banks earthquakes. Their locations are shown in Figure 2.1 and their source parameters summarized in Table 2.1. All except the Santa Barbara Island earthquake are thrust events. The 1927 Lompoc earthquake is also modeled by comparing the seismograms with recent well modeled earthquakes at stations which recorded both.

Table 2.1
Summary of Source Parameters

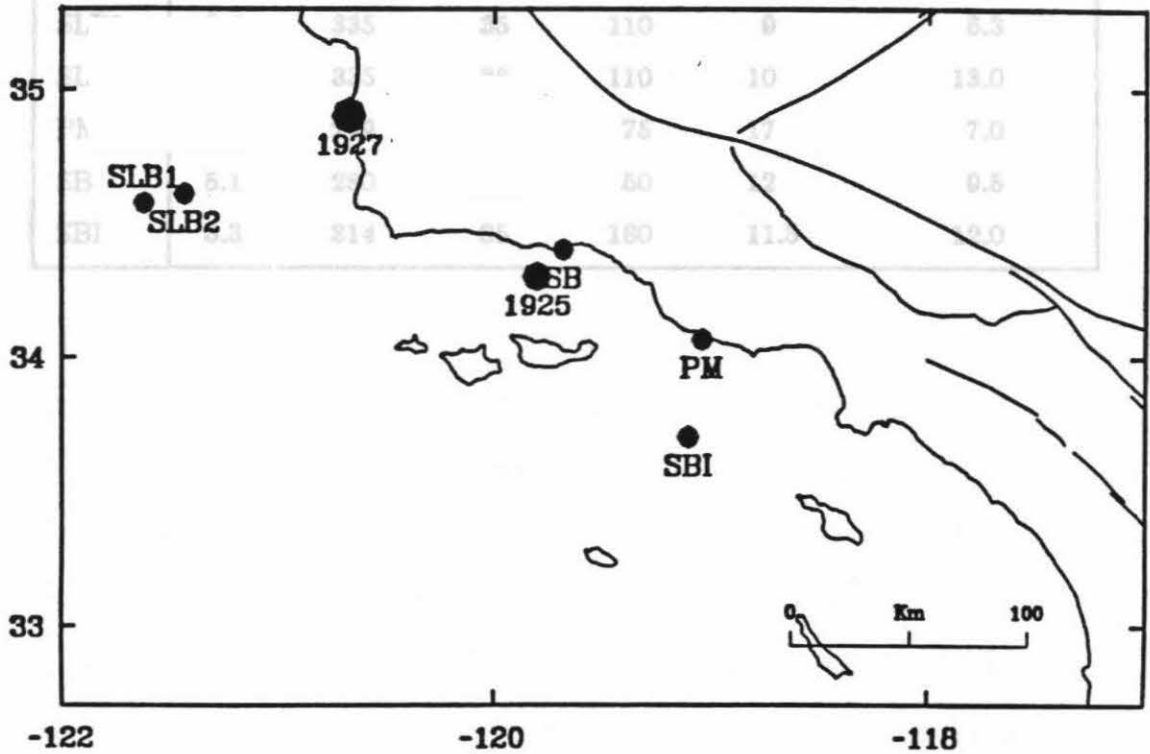


Figure 2.1

Map of recent and historic earthquakes in the western Transverse Ranges nearshore region. The symbol size increases with each order of magnitude. SLB1 and SLB2 are the Santa Lucia Banks earthquakes, SB is Santa Barbara, PM is Point Mugu, and SBI is Santa Barbara Island. The historic events are labeled by date.

Table 2.1
Summary of Source Parameters

Event	M_L	Strike (deg)	Dip (deg)	Rake (deg)	Depth (km)	Moment (10^{24} dyne cm)
SLB1	5.4	335	35	110	9	6.3
SLB2	5.8	335	38	110	10	13.0
PM	6.0	249	49	75	17	7.0
SB	5.1	280	25	50	12	9.5
SBI	5.3	314	85	180	11.5	12.0

We use regional and teleseismic data recorded by the WWSSN and Canadian networks to model the earthquakes. Because the earthquakes occurred to the west of most California stations, the data recorded by local arrays do not provide good azimuthal coverage. By using worldwide data we are able to improve the azimuthal coverage although data to the southwest are still lacking. We hand digitize the data and match the waveforms and amplitudes to synthetic seismograms obtained by a forward modeling technique discussed in detail by *Langston and Helmberger [1975]* and *Helmberger and Engen [1980]*. This technique gives us the faulting parameters, depth of hypocenter, and seismic moment. We concentrate on P waves as the SH waves for the thrust events tend to be contaminated by shear-coupled PL waves and the Santa Barbara Island event was not well recorded at teleseismic distances. Travel time data at regional distances provide us with information about the crustal thickness and upper mantle velocity along the path from source to receiver.

Initially we used a simple layer over a half-space velocity model (Table 2.2). This model worked well for regional data, but not for teleseismic data. To better fit the amplitudes of reflected phases (pP and sP) at teleseismic distances we added a low velocity layer at the surface (Table 2.3).

2.2 Santa Lucia Banks Earthquakes

In 1969, two moderate earthquakes occurred in the Santa Lucia Banks region. The first, with an estimated M_L of 5.4 [*Gawthrop, 1978a*], occurred on 22 October. The second (M_L 5.8 [*Gawthrop, 1978a*]) occurred on 5 November. We refer to these events as SLB1 and SLB2 respectively.

At long periods, the waveforms for both events at stations which recorded both are almost identical, suggesting similar source parameters. At

Table 2.2

Regional Velocity Model

Layer	P velocity km/s	S velocity km/s	Density g/cm ³	Thickness km
1	6.2	3.5	2.7	24-42
2	8.2	4.5	3.4	

Table 2.3

Teleseismic Velocity Model

Layer	P velocity km/s	S velocity km/s	Density g/cm ³	Thickness km
1	3.5	2.1	1.6	2
2	6.2	3.5	2.7	22-30
3	8.2	4.5	3.4	

short periods, the waveforms for SLB2 are somewhat more complex than those for SLB1 (Figure 2.2), indicating that either SLB2 has a complex source time history or that there is some difference in the very near-source structure between the two hypocenters. The former is the more likely cause of the observed waveform complexity since the two events are separated by less than 15 km.

The regional and teleseismic data and synthetic seismograms for these events are shown in Figures 2.3, 2.4, 2.5, and 2.6. Figure 2.4 also illustrates the improvement in the fit of the teleseismic waveforms to the data if a low velocity near-surface layer is included in the velocity model. The source parameters except for seismic moment are similar for both events. For both we obtain a strike of 335° and rake of 10° . SLB1 has a dip of 35° and depth of 9 km, while SLB2 has a dip of 38° and a depth of 8 km. The long-period seismic moment for SLB1 is 6.3×10^{24} dyne cm; SLB2 has a long-period moment of 1.3×10^{25} dyne cm, roughly twice that of SLB1.

Figure 2.7 shows the short-period data and synthetics for SLB1. A triangular source time function with a 0.75 second rise time and a 0.25 second fall-off was used to make the synthetics. In general the fit of the synthetic waveforms to the data is very good. In some cases the synthetic P arrival is too sharp. This can be corrected by increasing the rise time, but using a longer source time function worsens the overall fit by increasing the period of the waves. The solution we have used represents the best compromise between amplitude and frequency.

At short periods SLB2 (Figure 2.8) can be modeled by three subevents with identical focal mechanisms which are the same as the long-period solution. The first two occurred at a depth of 6 km and the third at 4 km. The

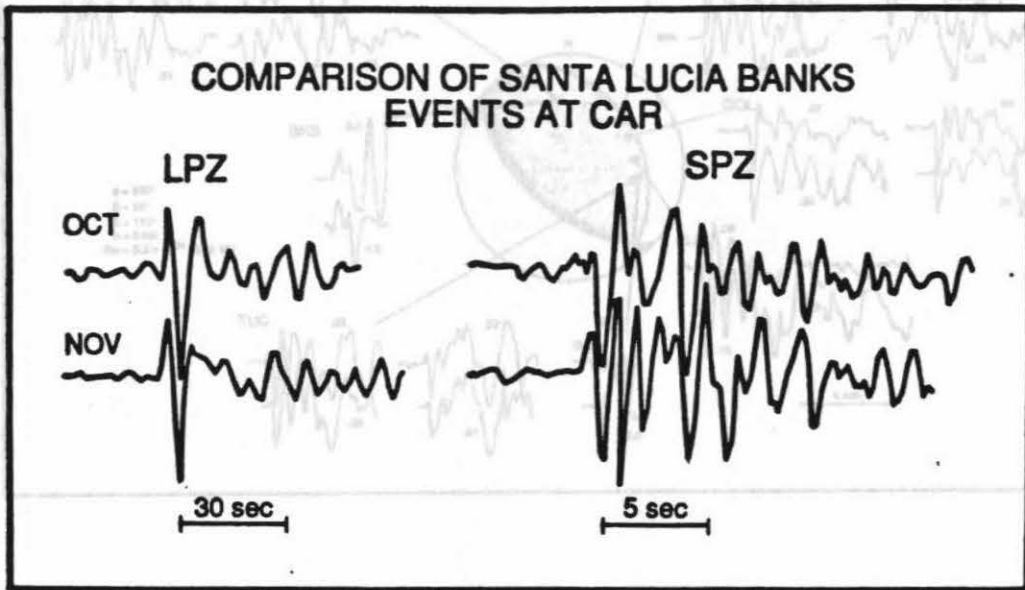


Figure 2.3
Regional data and synthetics for Figure 2.2 Santa Lucia Banks event. The Long- and short-period data of the Santa Lucia Banks earthquakes recorded at Caracas.

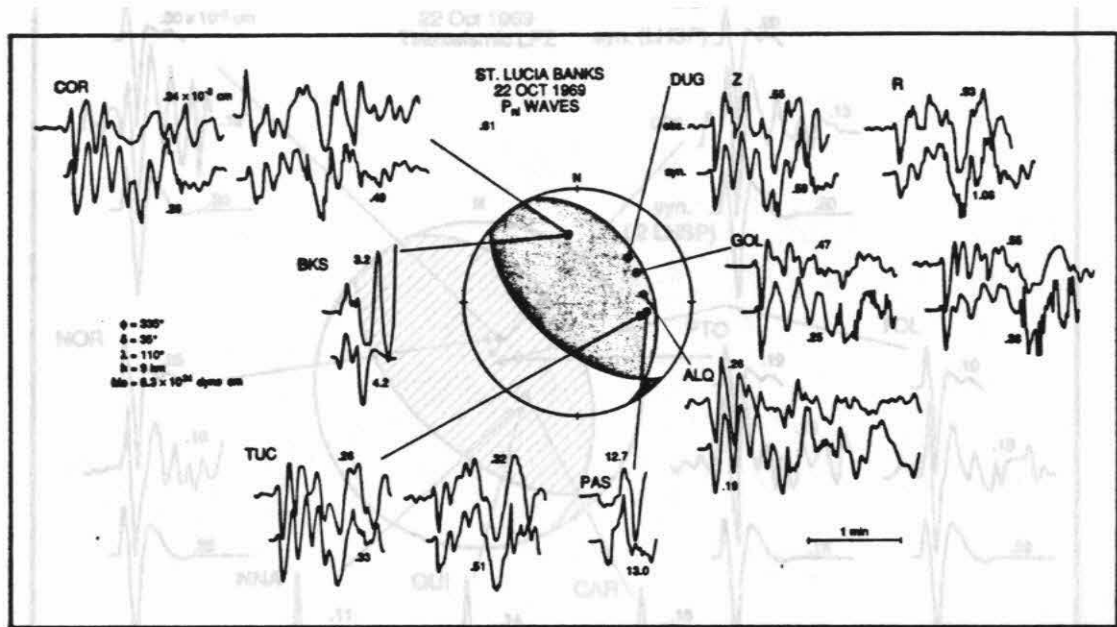


Figure 2.3

Regional data and synthetics for the Oct. Santa Lucia Banks event. The upper trace is the data and the lower is the synthetic. When more than one component is available the vertical is shown on the left and the radial on the right. The seismograms have been normalized to the same maximum peak-to-peak amplitude. Amplitudes are given in units of 10^{-3} cm and have the instrument magnification removed.

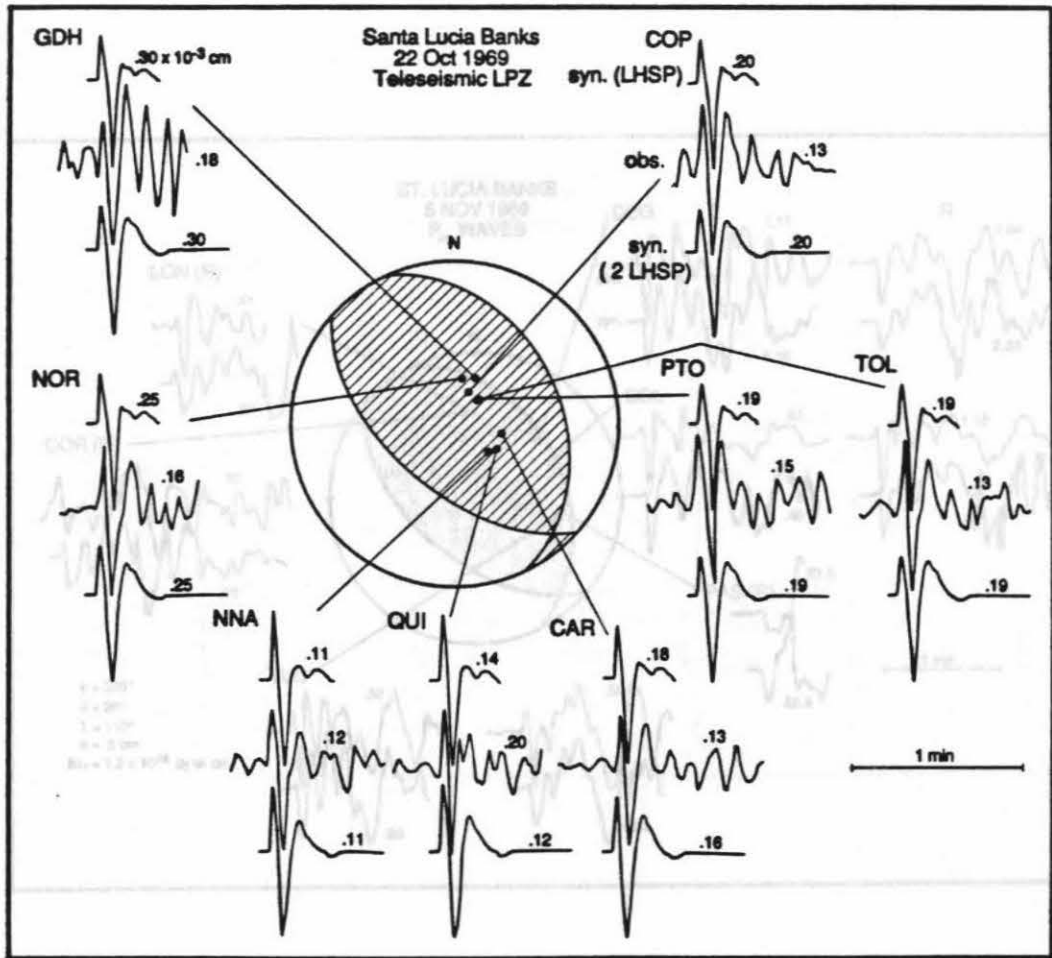


Figure 2.4

Teleaseismic P data and synthetics for the Oct. Santa Lucia Banks earthquake. Only the vertical component is shown. The upper trace is the synthetic for the single layer over half-space model (Table 2.2); the middle trace is the data; the lower trace is the synthetic for the 2 layer over half-space model (Table 2.3). The amplitudes are as in Figure 2.3.

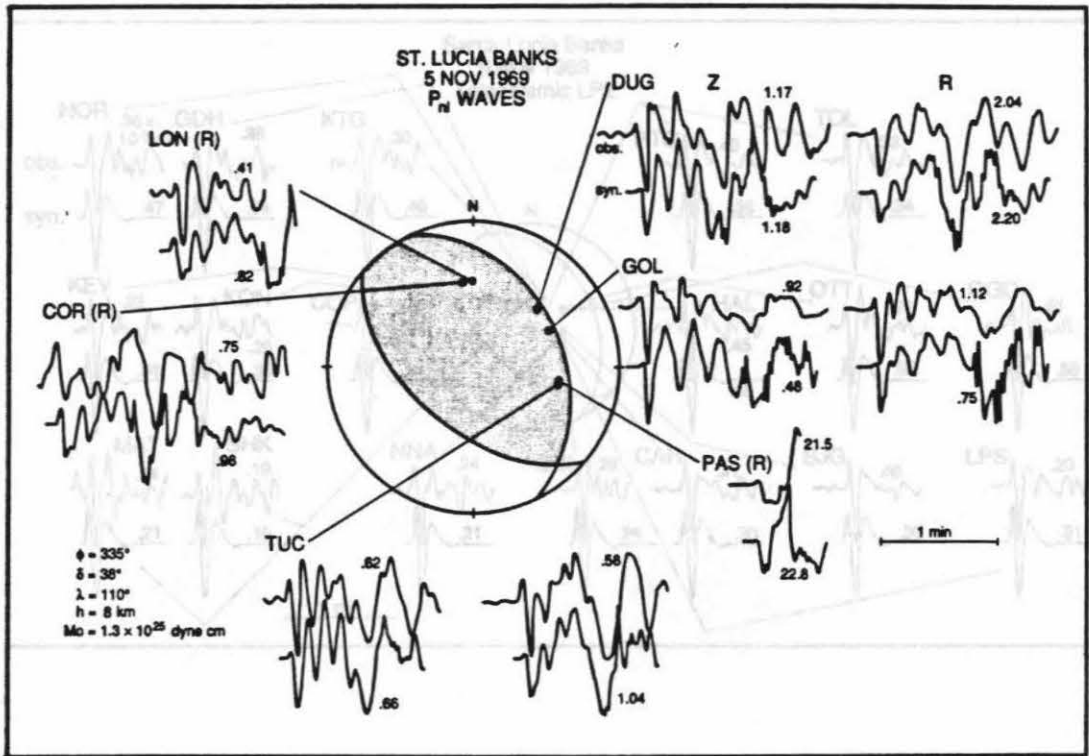


Figure 2.5

Regional data and synthetic seismograms for the Nov. Santa Lucia Banks earthquake. The format is the same as Figure 2.3.

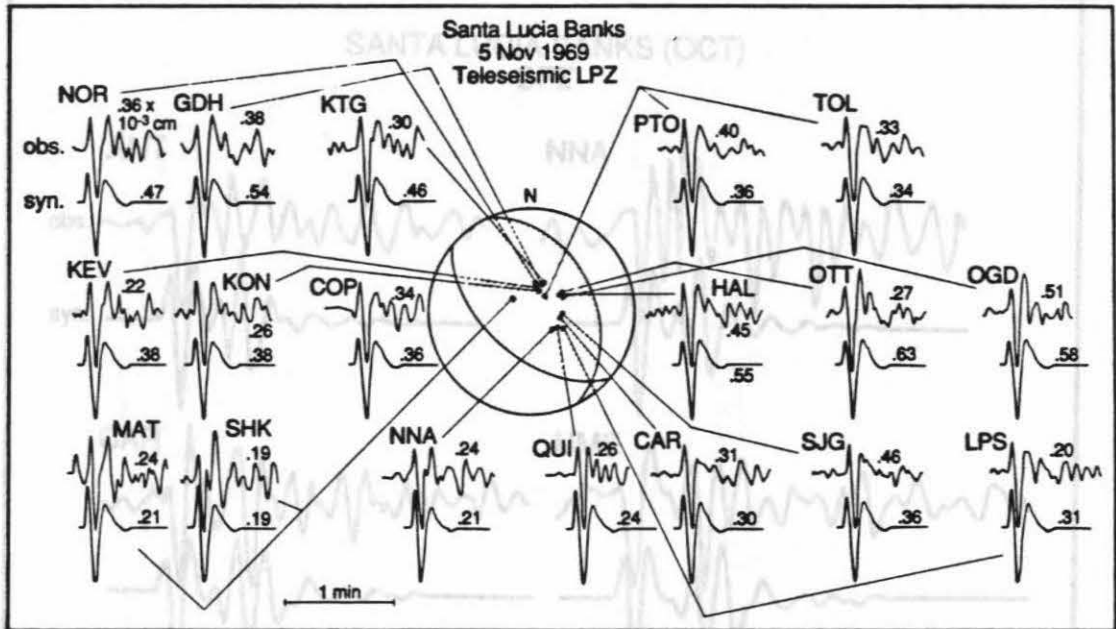


Figure 2.6

Teleseismic P data and synthetics for the Nov. Santa Lucia Banks earthquake. The format is the same as Figure 2.4. $\Delta t_x = 0$, and $\Delta t_y = 0.25$ seconds.

NOV. SANTA LUCIA (SPZ)

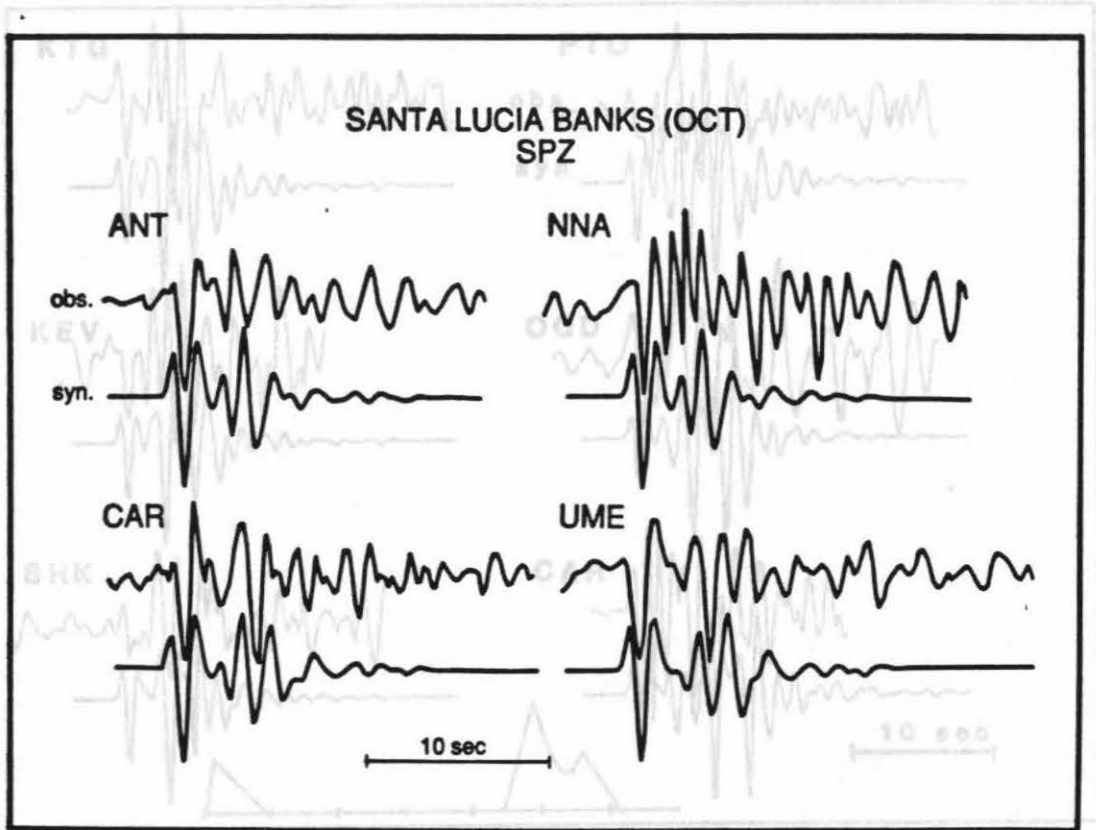


Figure 2.7

Short-period data and synthetics for SLB1. The synthetics were calculated using a source time function of $\Delta t_1 = 0.75$, $\Delta t_2 = 0$, and $\Delta t_3 = 0.25$ seconds. Tick marks at 1 sec. intervals.

NOV. SANTA LUCIA (SPZ)

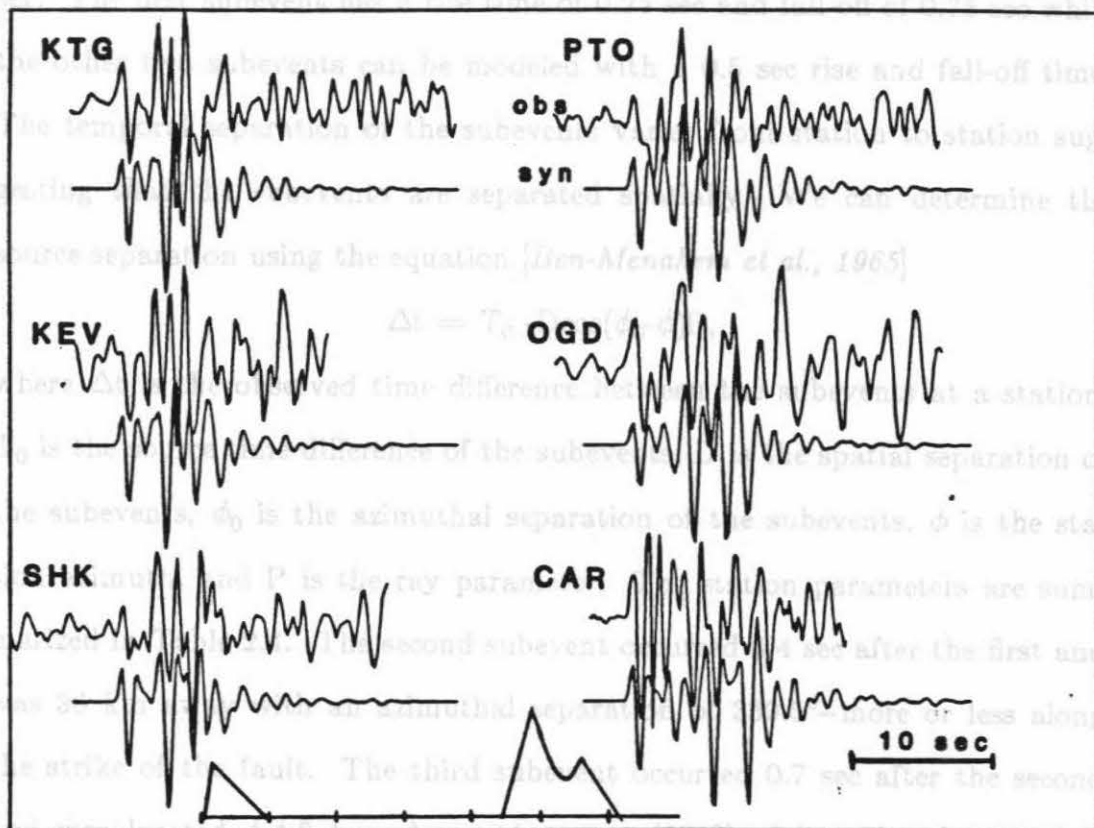


Figure 2.8
Short-period data and synthetics for SLB2. The stations are arranged clockwise according to azimuth. The time function is shown at the bottom, with tic marks at 1 sec. intervals.

The rupture velocity should be equal to D/T_0 . For this earthquake the apparent rupture velocity is 8 km/sec which is not physically reasonable (rupture velocities are normally on the order of 3 km/sec) suggesting that the earthquake did not occur as a single propagating rupture. The large spatial

first and third subevents have approximately equal moments, while the second one is 1.5 to 2 times larger--small changes in the size of this subevent result in only minor variations in the waveforms. All subevents have a duration of 1 sec. The first subevent has a rise time of 0.25 sec and fall-off of 0.75 sec while the other two subevents can be modeled with a 0.5 sec rise and fall-off time. The temporal separation of the subevents varies from station to station suggesting that the subevents are separated spatially. We can determine the source separation using the equation [Ben-Menahem *et al.*, 1965]

$$\Delta t = T_0 - D \cos(\phi_0 - \phi) P,$$

where Δt is the observed time difference between the subevents at a station, T_0 is the source time difference of the subevents, D is the spatial separation of the subevents, ϕ_0 is the azimuthal separation of the subevents, ϕ is the station azimuth, and P is the ray parameter. The station parameters are summarized in Table 2.4. The second subevent occurred 4.4 sec after the first and was 36 km away with an azimuthal separation of 339.5° --more or less along the strike of the fault. The third subevent occurred 0.7 sec after the second and was located 4-4.5 km almost due west (272°) of it. The short period records can be read with an uncertainty of less than 0.2 sec, which results in a distance error of less than 5 km in the spatial separation of the subevents. Modeling the long-period records with this solution we obtain a combined moment of 2.2×10^{25} dyne cm, or 5.5×10^{24} for the first and third subevents and 1.1×10^{25} for the second.

The rupture velocity should be equal to D/T_0 . For this earthquake the apparent rupture velocity is 8 km/sec which is not physically reasonable (rupture velocities are normally on the order of 3 km/sec) suggesting that the earthquake did not occur as a single propagating rupture. The large spatial

Table 2.4
Station Parameters for SLB2

Station	Δt_1 (sec)	Δt_2 (sec)	ϕ (deg)	P (km/sec) ⁻¹
CAR	5.7	1.0	102.1	0.065
KEV	2.8	0.7	10.9	0.053
KTG	2.8	0.8	22.3	0.062
OGD	4.2	1.0	65.8	0.077
PTO	3.7	0.8	44.5	0.047
SHK	3.0	0.5	306.9	0.047

Δt_1 is the separation between the 1st and 2nd subevents

Δt_2 is the separation between the 2nd and 3rd subevents

separation and small time separation may imply that the second subevent was triggered by the first subevent, possibly by its P waves. More work needs to be done before the triggering hypothesis can be verified.

In modeling the short period records, it was noticed that the first arrivals were later than expected based on the Caltech catalog location and origin time for SLB2. Further inspection showed that direct P was consistently on the order of 5.5 sec late at all stations. We also timed the corresponding long-period records and found the same trend but with a bit more scatter in the data. Since we have good azimuthal coverage (180°) for this event, the consistency of the differences between the theoretical and observed travel times suggests that the origin time is more likely to be the cause of the error than is the location. The ISC catalog lists the USGS origin time as 5.7 sec later than the PAS time making it more consistent with the observations. The locations are also slightly different, but not large enough to compensate for the difference in origin times.

2.3 Point Mugu Earthquake

The Point Mugu earthquake of 21 February 1973 (M_L 6.0, [Ellsworth *et al.*, 1973]) is the deepest of the events studied, occurring at a depth of 17 km. It is primarily a thrust event with a strike of 249° , dip of 49° , and rake of 75° . This mechanism is in good agreement with that of Ellsworth *et al.* [1973] obtained from local first motion data. The regional and teleseismic data and synthetics are shown in Figures 2.9 and 2.10 respectively. The north-dipping nodal plane is well constrained by the observed first motions. While the first motions at COR and EDM are somewhat ambiguous, DUG and SES are definitely compressional, and BKS and VIC are definitely dilatational. The

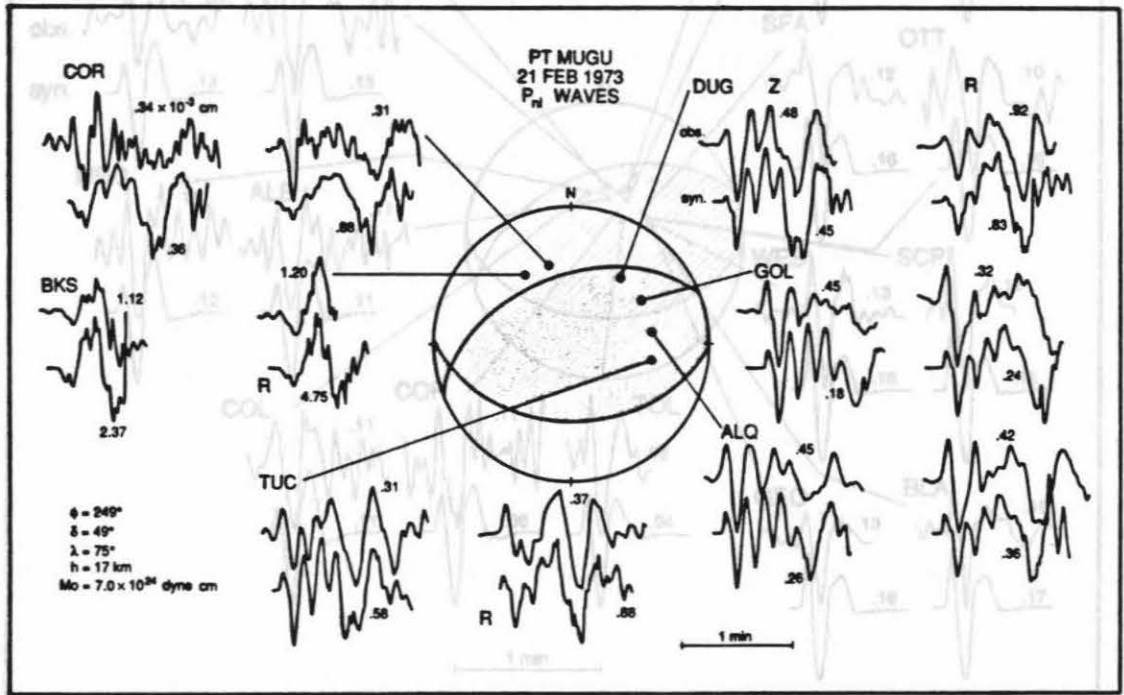
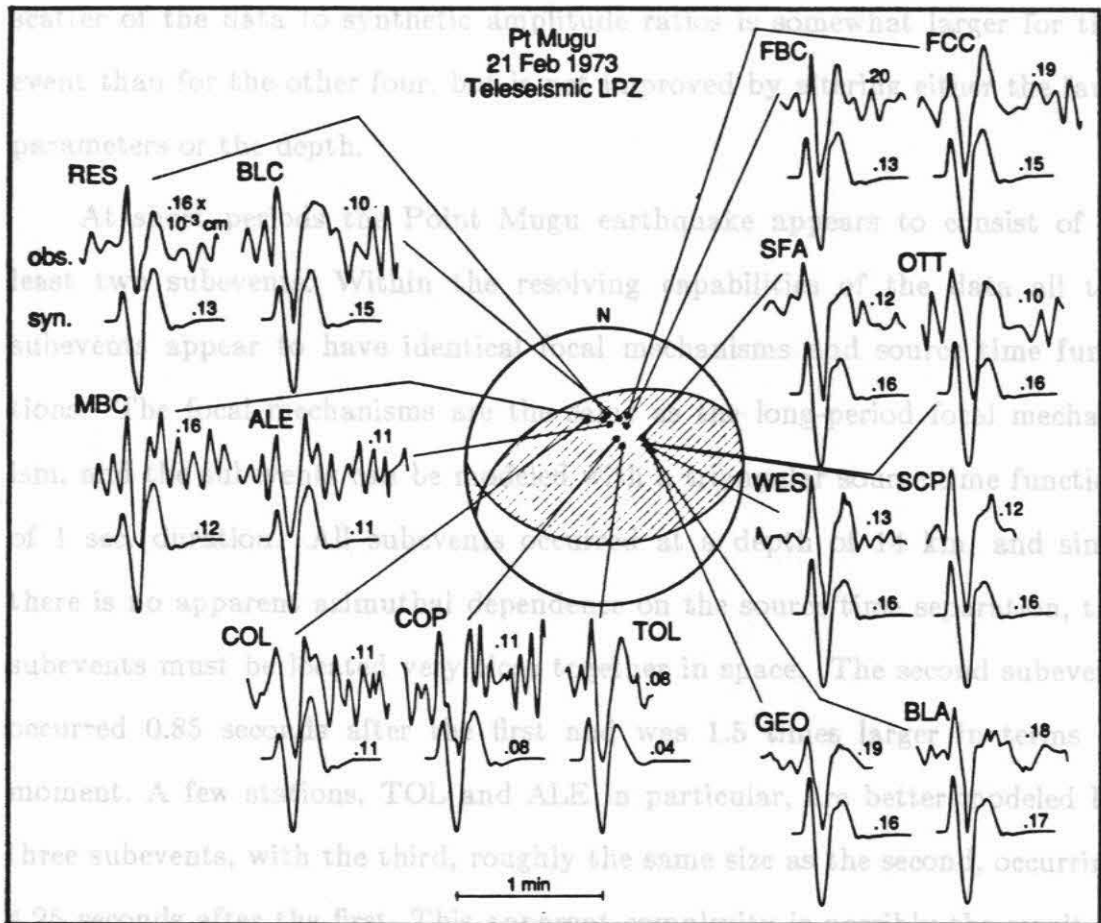


Figure 2.9

Regional long-period data and synthetics for the Point Mugu earthquake. The format is the same as Figure 2.3.

auxiliary plane is obtained from the rake which best fits the overall waveforms. We obtain a long-period seismic moment of 7×10^{24} dyne cm. The



near-receiver structure. ALE is on an island and near the coast, while TOL also has more and larger late arrivals than other stations for the Santa Barbara earthquake as well possibly indicating some near-receiver structural com-

Figure 2.10
Long-period teleseismic data and synthetics for the Point Mugu earthquake.
The format is the same as Figure 2.4.

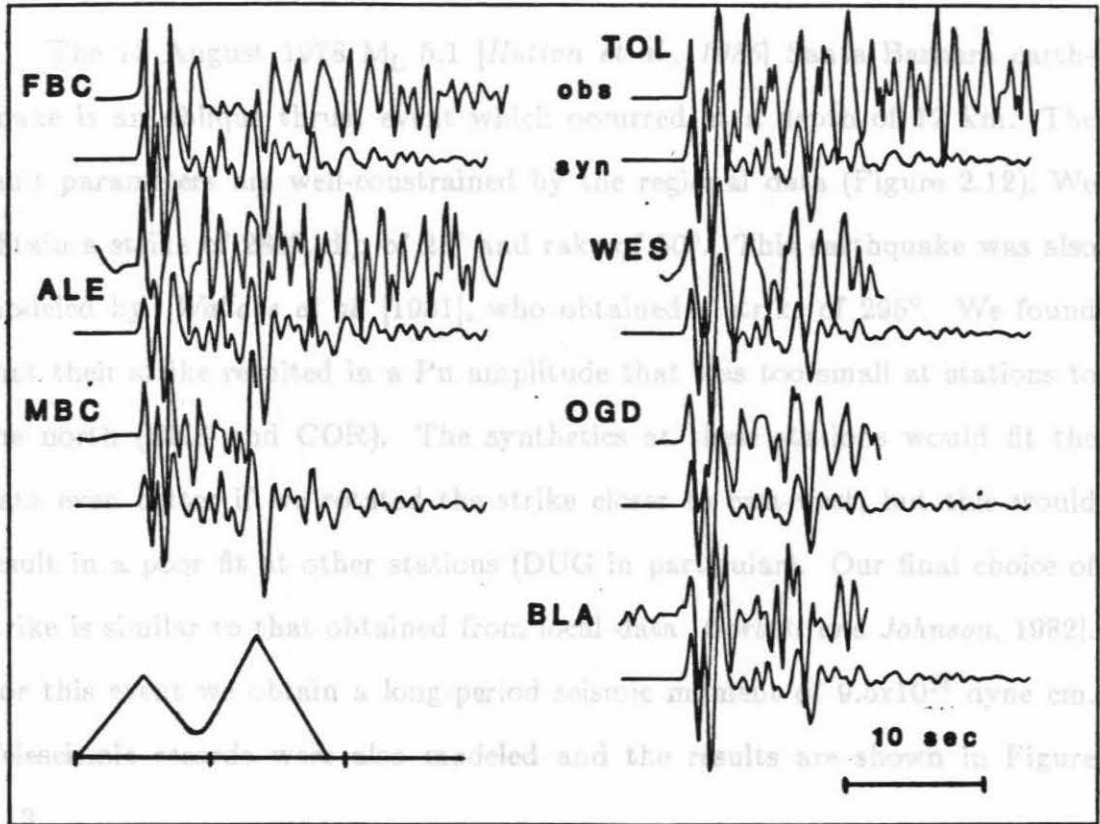
Using the two source solution to model the long-period records we obtain seismic moments of 2.9×10^{24} and 4.3×10^{24} dyne cm for the first and second subevents respectively. When we remodel the long-period records using the three source short-period solution, we obtain a seismic moment of 9×10^{24} dyne cm or 2.2×10^{25} for the first subevent and 3.4×10^{24} each for the

auxiliary plane is obtained from the rake which best fits the overall waveforms. We obtain a long-period seismic moment of 7×10^{24} dyne cm. The scatter of the data to synthetic amplitude ratios is somewhat larger for this event than for the other four, but is not improved by altering either the fault parameters or the depth.

At short periods the Point Mugu earthquake appears to consist of at least two subevents. Within the resolving capabilities of the data all the subevents appear to have identical focal mechanisms and source time functions. The focal mechanisms are the same as the long-period focal mechanism, and the subevents can be modeled with a triangular source time function of 1 sec. duration. All subevents occurred at a depth of 14 km, and since there is no apparent azimuthal dependence on the source time separation, the subevents must be located very close together in space. The second subevent occurred 0.85 seconds after the first and was 1.5 times larger in terms of moment. A few stations, TOL and ALE in particular, are better modeled by three subevents, with the third, roughly the same size as the second, occurring 4.25 seconds after the first. This apparent complexity is possibly the result of near-receiver structure. ALE is on an island and near the coast, while TOL also has more and larger late arrivals than other stations for the Santa Barbara earthquake as well possibly indicating some near-receiver structural complexity. The short-period data and synthetic seismograms are shown in Figure 2.11. Using the two source solution to model the long-period records we obtain seismic moments of 2.9×10^{24} and 4.3×10^{24} dyne cm for the first and second subevents respectively. When we remodel the long-period records using the three source short-period solution, we obtain a seismic moment of 9×10^{24} dyne cm or 2.2×10^{24} for the first subevent and 3.4×10^{24} each for the

PT MUGU SPZ

2.4 Santa Barbara Earthquake



The Santa Barbara earthquake also appears to be a complex event at short periods. The short-period waveforms are best modeled by two

Figure 2.11

Short-period teleseismic data and synthetics for the Point Mugu earthquake. The tic marks on the time function are at 1 sec intervals.

but the variation is not azimuthally dependent, so this is unlikely to be

second and third.

2.4 Santa Barbara Earthquake

The 13 August 1978 M_L 5.1 [Hutton *et al.*, 1985] Santa Barbara earthquake is an oblique thrust event which occurred at a depth of 12 km. The fault parameters are well-constrained by the regional data (Figure 2.12). We obtain a strike of 280° , dip of 25° and rake of 50° . This earthquake was also modeled by Wallace *et al.* [1981], who obtained a strike of 295° . We found that their strike resulted in a Pn amplitude that was too small at stations to the north (BKS and COR). The synthetics at these stations would fit the data even better if we rotated the strike closer to east-west, but this would result in a poor fit at other stations (DUG in particular). Our final choice of strike is similar to that obtained from local data [Corbett and Johnson, 1982]. For this event we obtain a long-period seismic moment of 9.5×10^{24} dyne cm. Teleseismic records were also modeled and the results are shown in Figure 2.13.

The Santa Barbara earthquake also appears to be a complex event at short periods. The short-period waveforms are best modeled by two subevents separated in time by 1.5 seconds (Figure 2.14). Some stations are better modeled with slightly longer or shorter (± 0.25 sec) source separations, but the variation is not azimuthally dependent, so this is unlikely to be caused by spatial separation of the subevents. Both have mechanisms identical to the long-period solution, and can be modeled with triangular source-time functions--the first with a duration of 0.5 sec. and the second with a duration of 1.0 sec. Although we prefer identical focal mechanisms for both subevents, we cannot completely rule out different sources. Figure 2.15

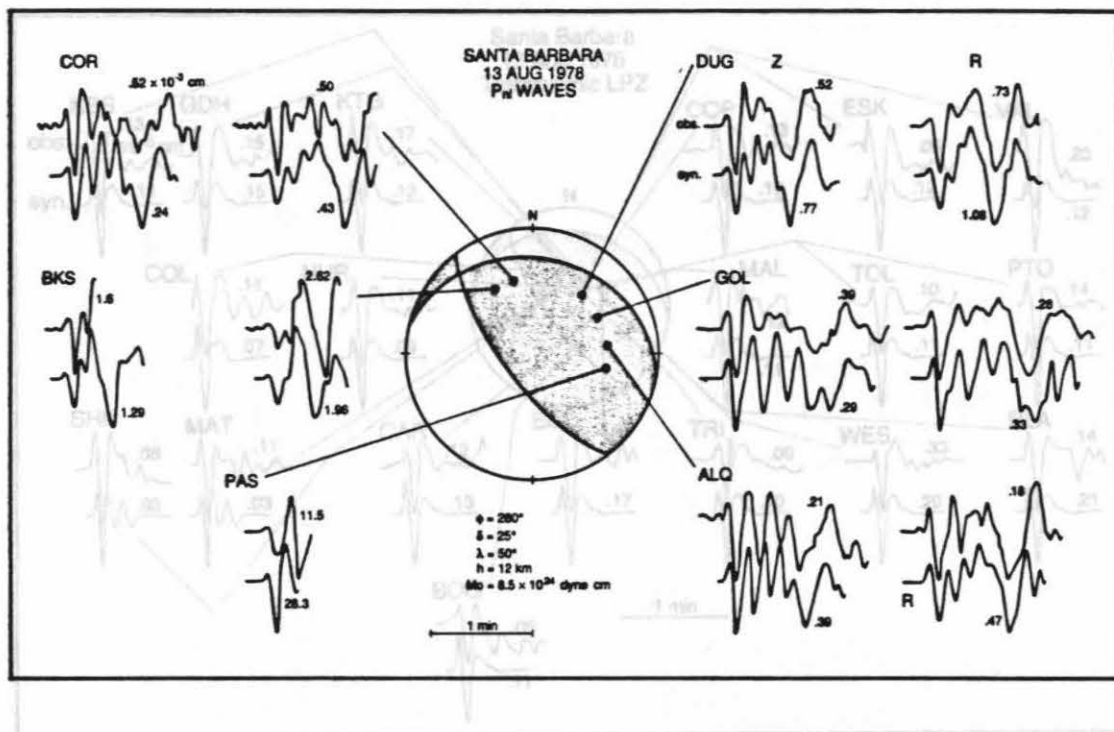


Figure 2.12
Long-period regional data and synthetics for the Santa Barbara earthquake.
The format is the same as Figure 2.3.

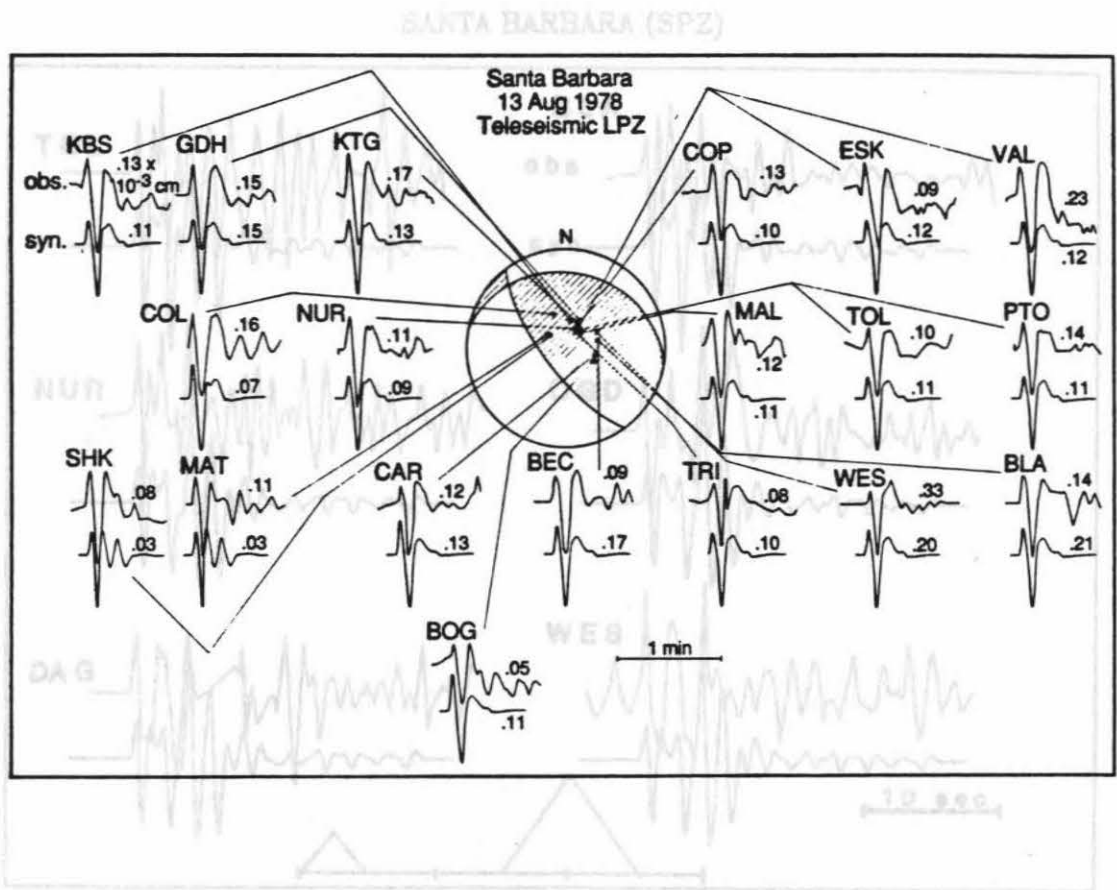


Figure 2.13

Long-period teleseismic data and synthetics for the Santa Barbara earthquake. The format is the same as Figure 2.4.

SANTA BARBARA (SPZ)

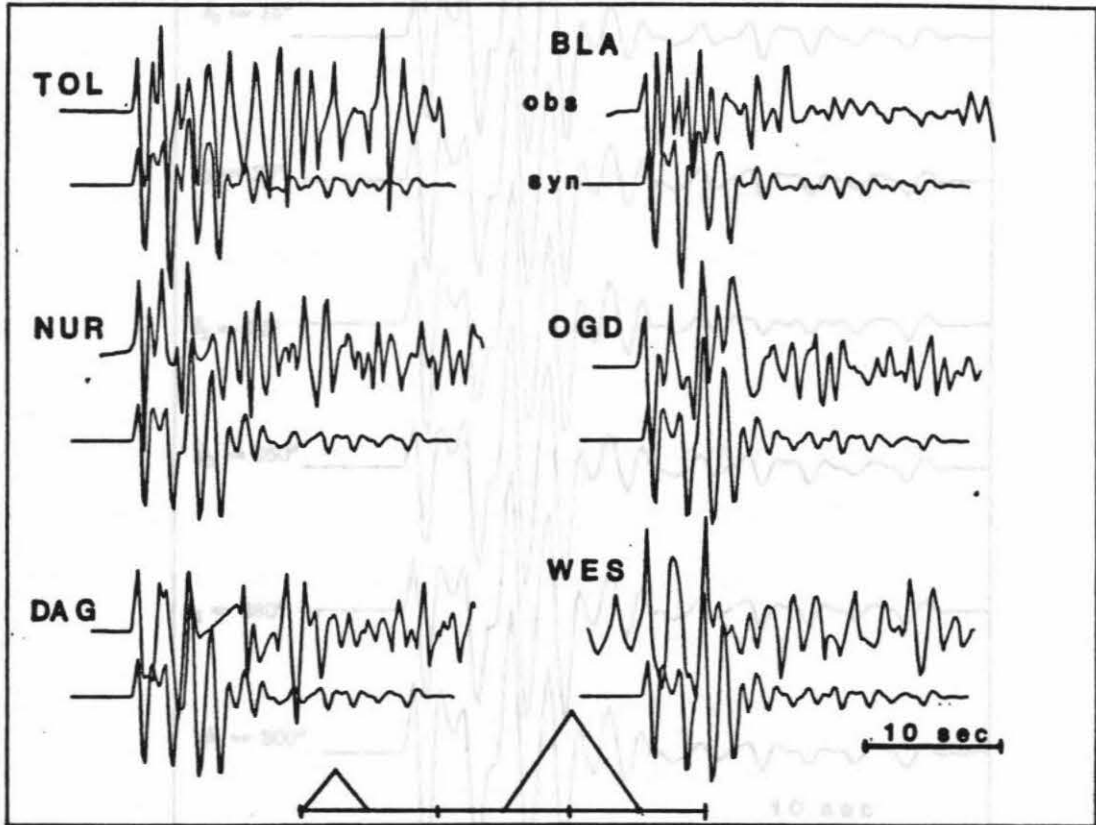


Figure 2.14

Short-period teleseismic data and synthetics for the Santa Barbara earthquake. Tic marks on the time function are at 1 sec intervals.

SANTA BARBARA -NUR.SPZ

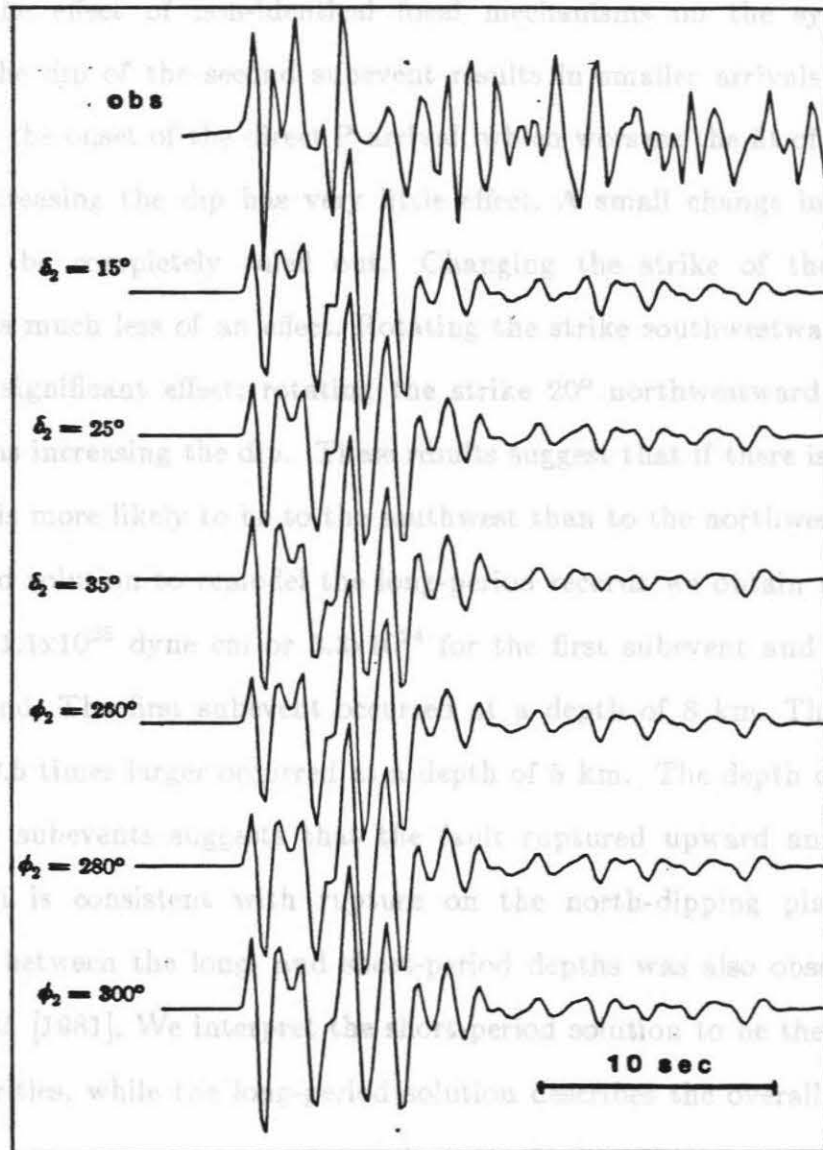


Figure 2.15

Short-period data and synthetics for the Santa Barbara earthquake recorded at NUR (Finland) showing the effects of the focal mechanism on the synthetics. Except for the changes indicated, the synthetics were made using the preferred short-period solution.

four, is a strike-slip event. This event is also the most southern and farthest offshore of the five earthquakes studied and has an M_L of 5.3 [Walton et al. 1985]. Because only a few stations recorded this event teleseismically, the source parameters were obtained solely by modeling the regional data shown

illustrates the effect of non-identical focal mechanisms on the synthetics. Increasing the dip of the second subevent results in smaller arrivals 2.5 and 5.5 sec after the onset of the direct P arrival, which worsens the fit of the synthetics. Decreasing the dip has very little effect. A small change in dip ($< 10^\circ$) cannot be completely ruled out. Changing the strike of the second subevent has much less of an effect. Rotating the strike southwestward up to 20° has no significant effect; rotating the strike 20° northwestward has the same effect as increasing the dip. These results suggest that if there is a strike rotation, it is more likely to be to the southwest than to the northwest. Using our preferred solution to remodel the long-period records we obtain a seismic moment of 1.1×10^{25} dyne cm or 3.3×10^{24} for the first subevent and 8.1×10^{24} for the second. The first subevent occurred at a depth of 8 km. The second which was 2.5 times larger occurred at a depth of 5 km. The depth difference between the subevents suggests that the fault ruptured upward and southward, which is consistent with rupture on the north-dipping plane. The discrepancy between the long- and short-period depths was also observed by *Wallace et al.* [1981]. We interpret the short-period solution to be the rupture of two asperities, while the long-period solution describes the overall rupture process.

2.5 Santa Barbara Island Earthquake

The 4 September 1981 Santa Barbara Island earthquake, unlike the other four, is a strike-slip event. This event is also the most southern and farthest offshore of the five earthquakes studied and has an M_L of 5.3 [*Hutton et al.*, 1985]. Because only a few stations recorded this event teleseismically, the source parameters were obtained solely by modeling the regional data shown

in Figure 2.16. We obtain a strike of 314° , a dip of 85° , and rake of 180° . The strike is roughly parallel to the main trend of the San Andreas Fault and also corresponds to that of the Santa Cruz-Catalina Ridge along which the aftershocks of this event lined up, and which is believed to be a fault [Corbett, 1984]. The long-period seismic moment is 1.1×10^{25} dyne cm. Our teleseismic data were insufficient for us to determine the depth. In our modeling we used a depth of 11.5 km, which is the depth determined by Corbett [1984]. Using this depth we obtain synthetic seismograms which fit the data well, but long-period P_{n1} waves for strike-slip earthquakes are not very sensitive to depth so we cannot determine how well constrained this depth is.

2.6 Crustal Thickness and Upper Mantle Velocity

To better fit the synthetic seismograms to the data we use Green's functions which are appropriate for the path from source to receiver rather than assuming a constant structure for all events and stations. The depth of the hypocenter can be constrained from the pP-P and sP-P times. Once the depth is known we use the P1-Pn time to constrain the crustal thickness. The crustal thickness used to model a given path may represent the average crustal thickness from source to receiver, but may also be strongly influenced by the near-source or near-receiver structure. The crustal thicknesses used in the P_{n1} modeling are shown in Figure 2.17. For the thrust events, the crustal thickness tends to increase as the epicenters move southward although the exact value varies from station to station. This trend does not necessarily mean that the crust actually thickens from north to south since the distance of the epicenter from the coast decreases southward. The apparent thickening may be a reflection of the difference between continental and oceanic crust.

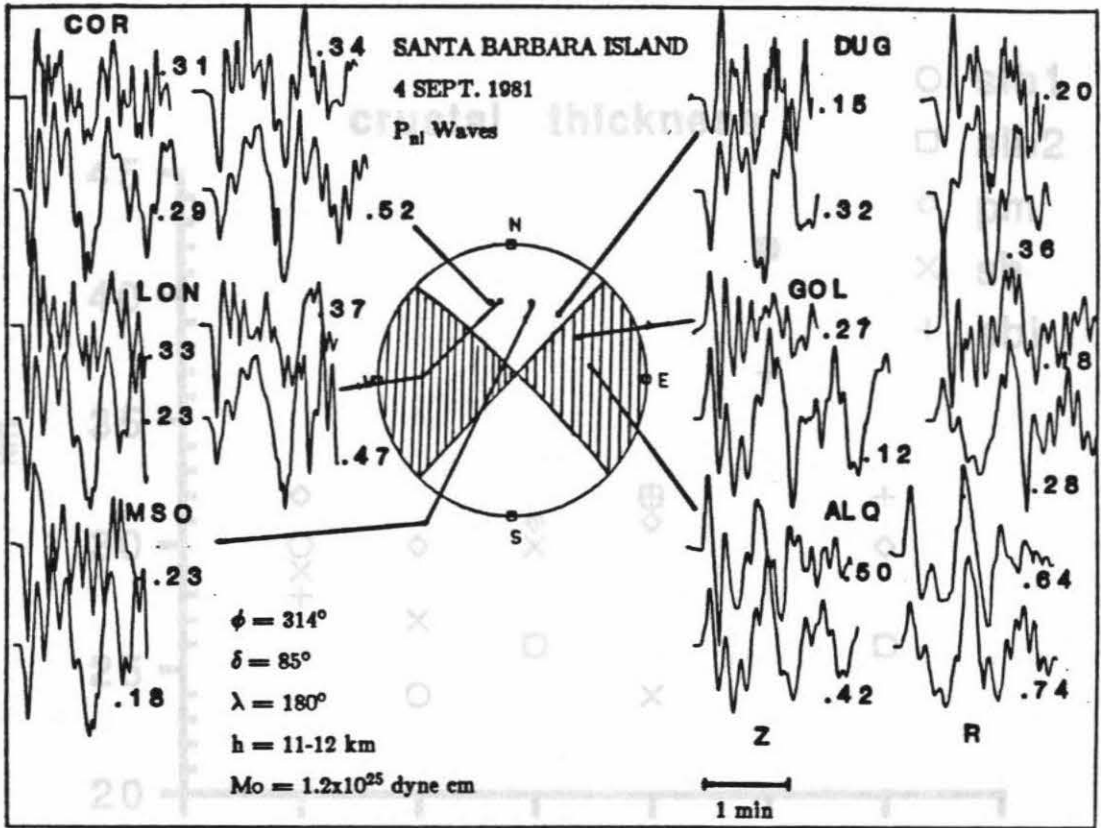


Figure 2.16
Long-period regional data and synthetics for the Santa Barbara Island earthquake. The format is the same as Figure 2.3.

this trend to the station GOL, ...
of 42 km. Santa Barbara Island
at GOL, but the data can be satisfied by a thick
GOL, all across the Colorado plateau and southern

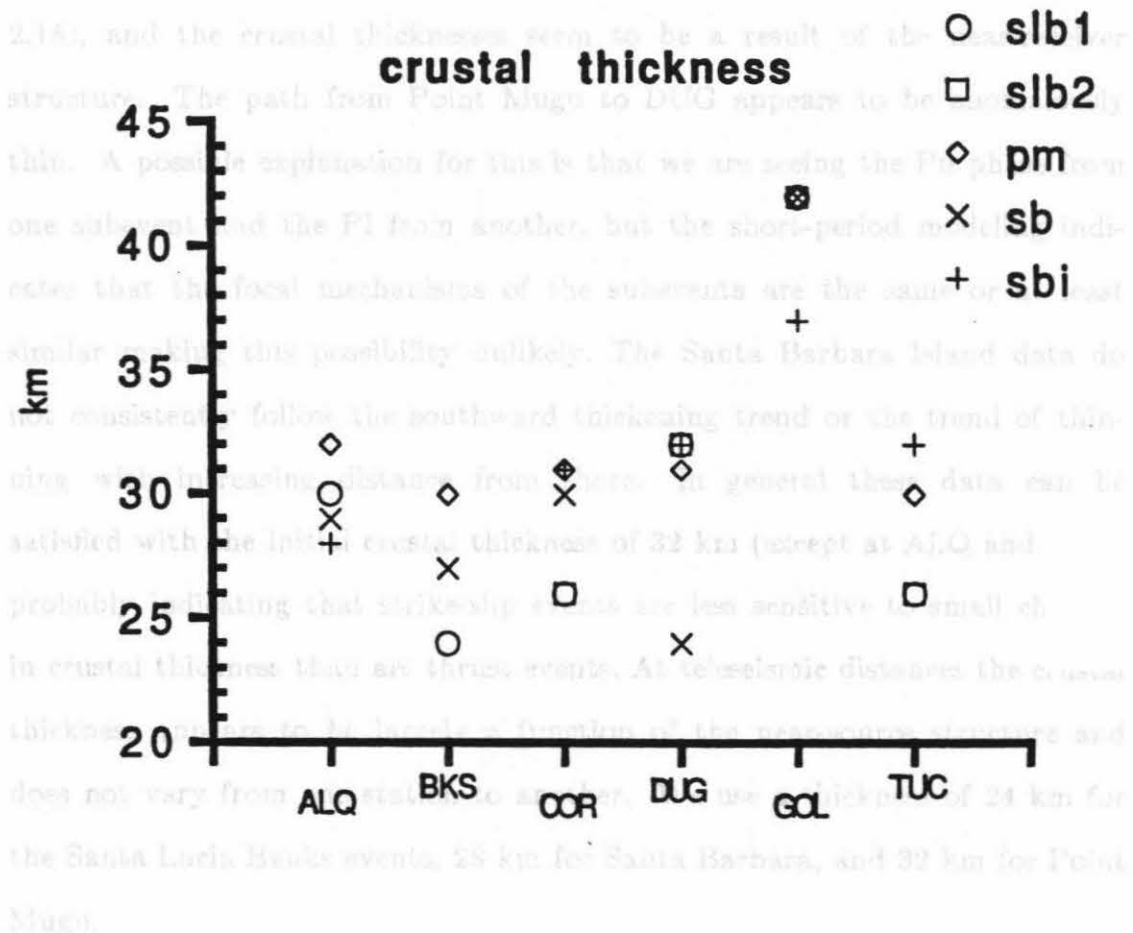


Figure 2.17
Crustal thicknesses (in km) which best fit the data. The uncertainty is 1-2 km. The events are labeled as in Figure 2.1.

One exception to this trend is the station GOL. All four thrust events require a very thick crust of 42 km. Santa Barbara Island also requires a thick crust at GOL, but the data can be satisfied by a thickness of 37 km. The paths to GOL all cross the Colorado plateau and southern Rocky Mountains (Figure 2.18), and the crustal thicknesses seem to be a result of the near-receiver structure. The path from Point Mugu to DUG appears to be anomalously thin. A possible explanation for this is that we are seeing the Pn phase from one subevent and the P1 from another, but the short-period modeling indicates that the focal mechanisms of the subevents are the same or at least similar making this possibility unlikely. The Santa Barbara Island data do not consistently follow the southward thickening trend or the trend of thinning with increasing distance from shore. In general these data can be satisfied with the initial crustal thickness of 32 km (except at ALQ and GOL) probably indicating that strike-slip events are less sensitive to small changes in crustal thickness than are thrust events. At teleseismic distances the crustal thickness appears to be largely a function of the near-source structure and does not vary from one station to another. We use a thickness of 24 km for the Santa Lucia Banks events, 28 km for Santa Barbara, and 32 km for Point Mugu.

Assuming we know the depth and crustal thickness, the absolute travel time of the Pn phase depends primarily on the Moho velocity as most of the path is along the Moho. We begin with the velocity model shown in Table 2.2, which has an upper mantle P-wave velocity of 8.2 km/s. The difference between the observed and theoretical travel times is used to determine the moho velocity. The results are shown in Figure 2.19. At stations where we obtained anomalous results, we also used the travel time data from the 1971

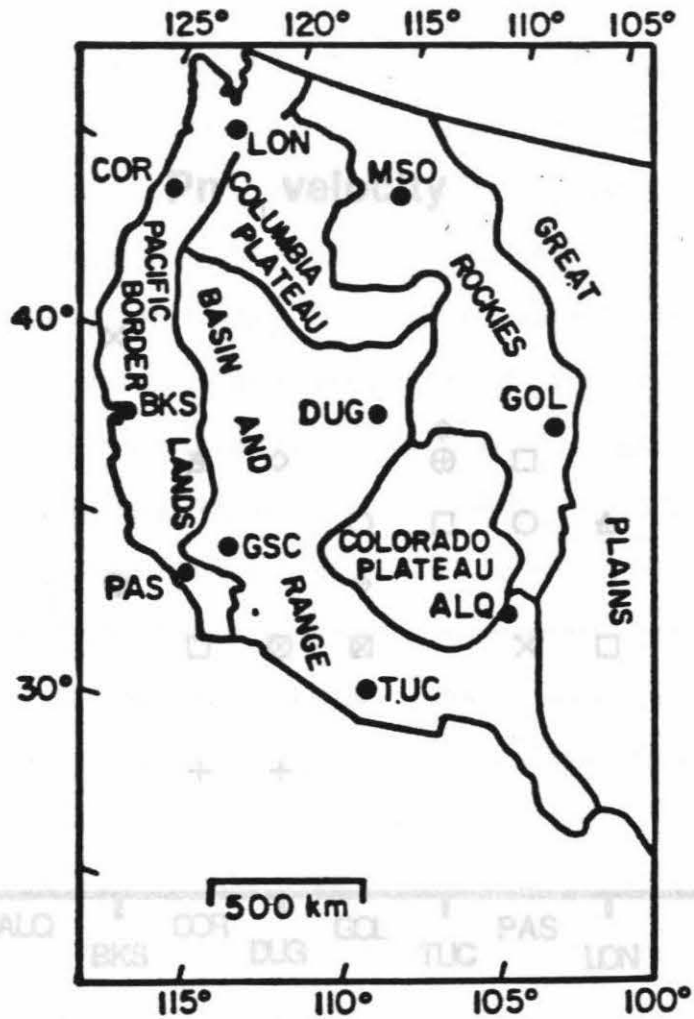


Figure 2.18

Map showing stations used in modeling regional phases and their tectonic settings (after *Helmberger and Engen [1980]*).

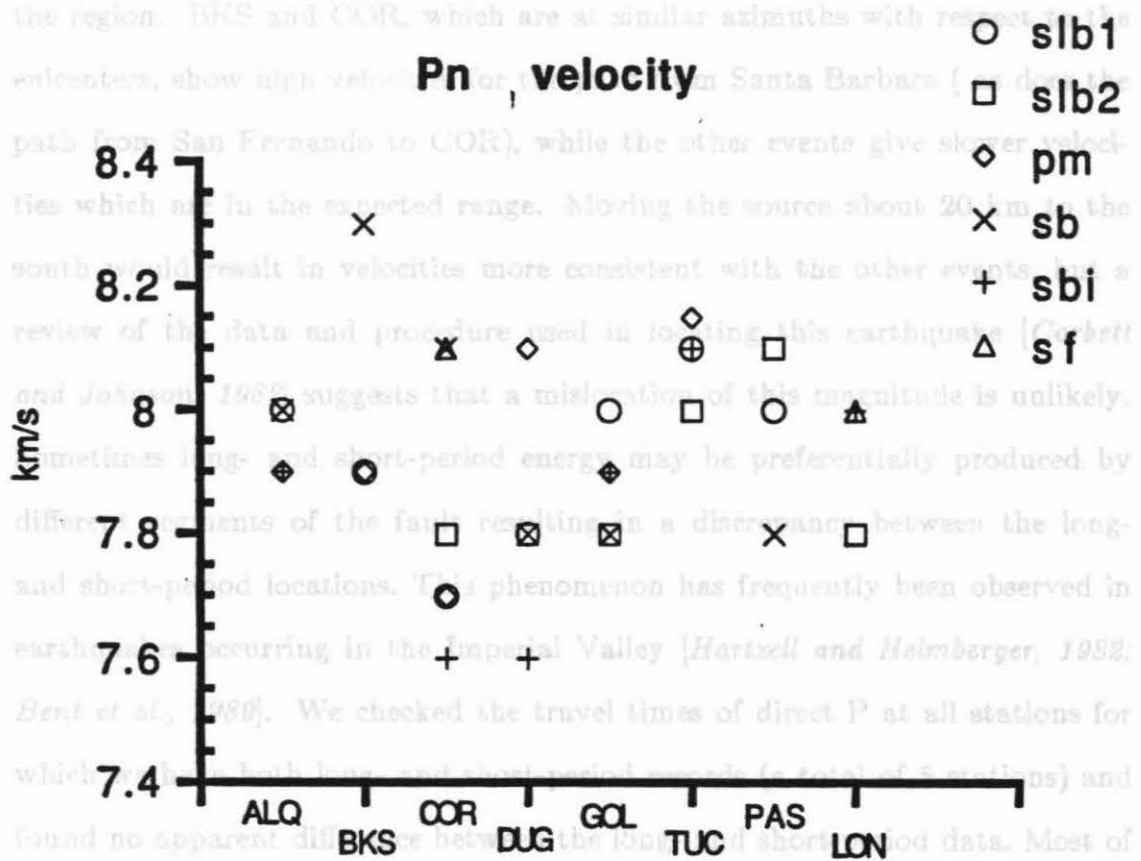


Figure 2.19 Moho velocities which fit the observed Pn travel times. The abbreviations are the same as in Figure 2.11, and sf is San Fernando.

San Fernando earthquake to increase the size of the data set. For the path to ALQ we obtain a moho velocity of 7.9 to 8.0 km/s. There is very little scatter in the data and the results agree with other studies [Wallace, 1983] of the region. BKS and COR, which are at similar azimuths with respect to the epicenters, show high velocities for the path from Santa Barbara (as does the path from San Fernando to COR), while the other events give slower velocities which are in the expected range. Moving the source about 20 km to the south would result in velocities more consistent with the other events, but a review of the data and procedure used in locating this earthquake [Corbett and Johnson, 1982] suggests that a mislocation of this magnitude is unlikely. Sometimes long- and short-period energy may be preferentially produced by different segments of the fault resulting in a discrepancy between the long- and short-period locations. This phenomenon has frequently been observed in earthquakes occurring in the Imperial Valley [Hartzell and Helmberger, 1982; Bent et al., 1989]. We checked the travel times of direct P at all stations for which we have both long- and short-period records (a total of 5 stations) and found no apparent difference between the long- and short-period data. Most of the differences correspond to distances of less than 5 km and with respect to time are within our uncertainty in picking the long-period phases. There is also no azimuthal trend in the travel time differences, suggesting that the long- and short-period locations should be the same.

The Santa Barbara and Santa Lucia Banks events all give a velocity of 7.8 km/s to DUG. The Point Mugu data suggest a much faster velocity. This anomaly may be due to the depth of the Point Mugu earthquake. We have assumed that the travel time residuals are due to variations only in the upper mantle velocity, but Point Mugu is deep enough that the crustal

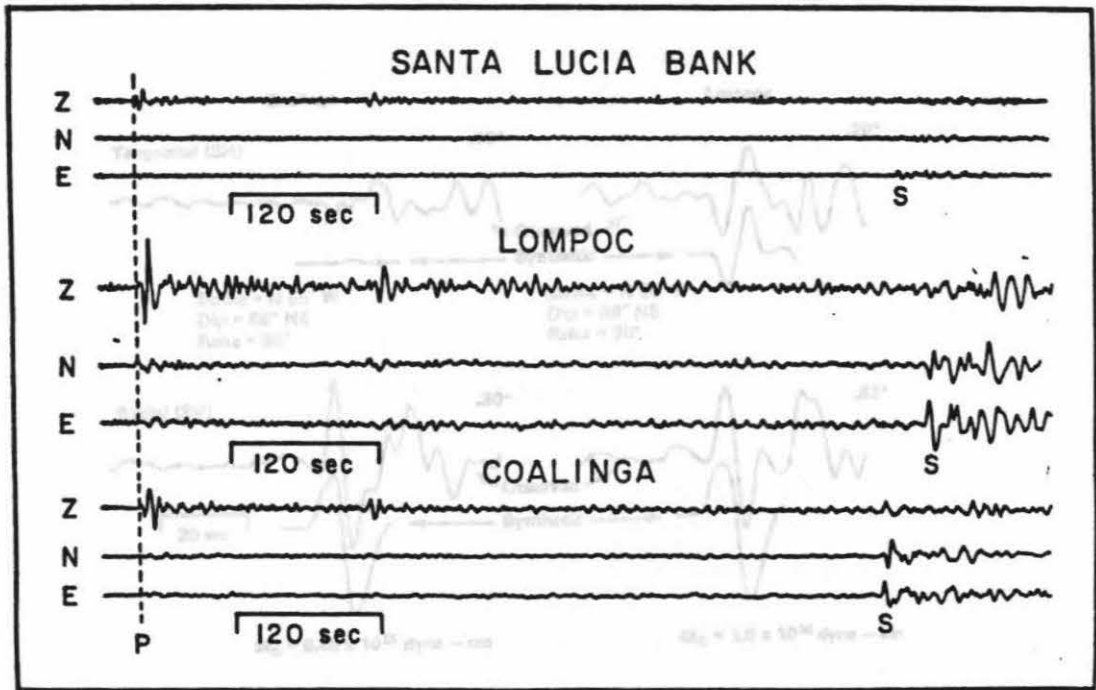
velocity we used may have been too low. The Santa Barbara Island data suggest that the path to DUG is slow. This may be due to a low velocity layer or structure in the source region. Although the scatter at GOL is somewhat larger than we would like, there are no anomalous events and the velocity range of 7.8 to 8.0 km/s is in the expected range. The path to TUC appears to be relatively fast, 8.0 to 8.1 km/s, for all events. There is very little scatter in our data set. This path is faster than what was expected based on the work of Wallace [1983]. The difference may be due to the fact that our velocities were determined for paths covering a small azimuthal range for each station, while his were determined from sources covering a much larger area. PAS shows a slow path with respect to Santa Barbara. If the event were mislocated to the north, the velocity would increase to be more consistent with the other data but, as discussed above with respect to BKS and COR, it is unlikely that the event is mislocated by the distance required to neutralize the velocity anomalies. Only two of the five events have good records from LON, but we include it since its azimuth is similar to that of BKS and COR. Unfortunately this station did not provide insight into the anomalies observed at the other two.

2.7 Lompoc Earthquake

The Lompoc earthquake of 4 November 1927 occurred before the deployment of a dense seismic array in California and has subsequently been the cause of considerable debate with respect to its location, focal mechanism and seismic moment. By using synthetic seismograms and comparing the Lompoc data to recent earthquakes at common stations some of the uncertainty about the Lompoc source parameters can be reduced.

The Lompoc earthquake as well as SLB2, the 2 May 1983 Coalinga earthquake and its largest aftershock were well recorded by the Galitzen instrument at De Bilt, Netherlands (DBN), an instrument which has been in continuous operation since the 1920's. At DBN the body waves for the Lompoc, Coalinga and Santa Lucia Banks events are very similar (Figure 2.20) on all three components suggesting similar focal mechanisms. Synthetic seismograms were made using the source parameters for the Coalinga mainshock [Choy, 1983], its largest aftershock (Chapter 3) and SLB2, and compared to the Lompoc record at DBN. The SH phase is much stronger for Lompoc than for Coalinga, which is near-nodal, suggesting that the strikes of the two events are not identical. A clockwise rotation of the strike by 40° , resulting in a strike of 340° for a pure thrust fault, gives SH synthetics that match the data in waveform and amplitude (Figure 2.21). If a strike-slip component of motion is added, the strike can rotate further toward north-south. The SV synthetics do not match the data as well, but this is a common problem usually due to SV-to-P precursors caused by the crust-mantle transition zone and by shear coupled PL waves arriving just after the direct S phase. The P waves (Figure 2.22) indicate that the depth of the Lompoc earthquake is similar to that of the calibration events or about 10 km. The P synthetics are compatible with the SH derived focal mechanism. By comparing the P wave amplitudes of the Lompoc and Coalinga earthquakes, a moment of 1.0×10^{26} dyne cm is obtained for the Lompoc earthquake. *Helmberger et al. [1990]* modeled regional body waves for the Lompoc earthquake and obtained good results using the teleseismic focal mechanism and moment.

Moment estimates for the Lompoc earthquake differ by as much as an order of magnitude. A moment of 1.0×10^{26} was obtained by modeling the



* Relative to 0H to EV Amplification

Figure 2.20

Body waves of the Nov. Santa Lucia Banks, Lompoc, and Coalinga earthquakes recorded at DBN. They are aligned so that the onset of direct P is in the same place.

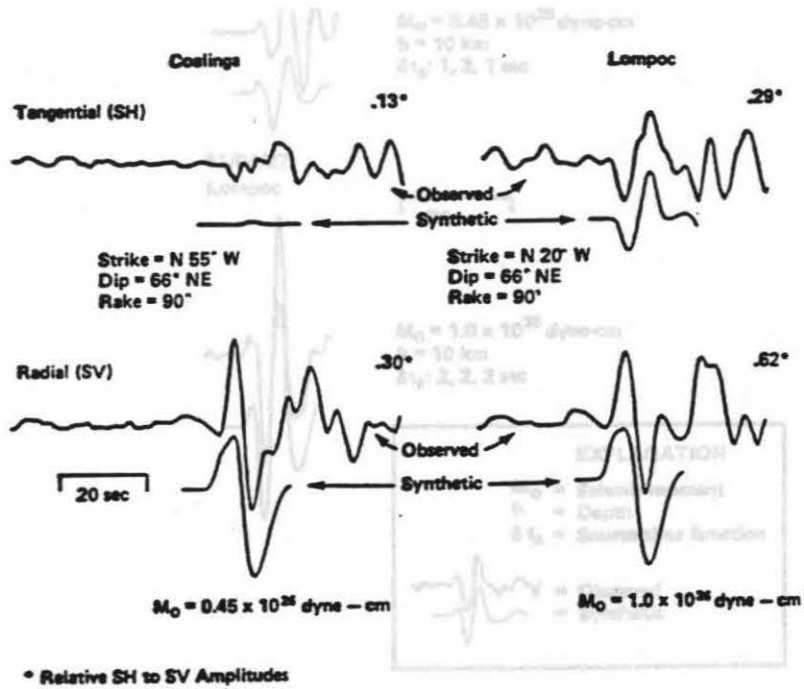


Figure 2.21

SH and SV data (upper) and synthetics (lower) for the Lompoc and Coalinga earthquakes at DBN. and largest aftershock) at DBN.

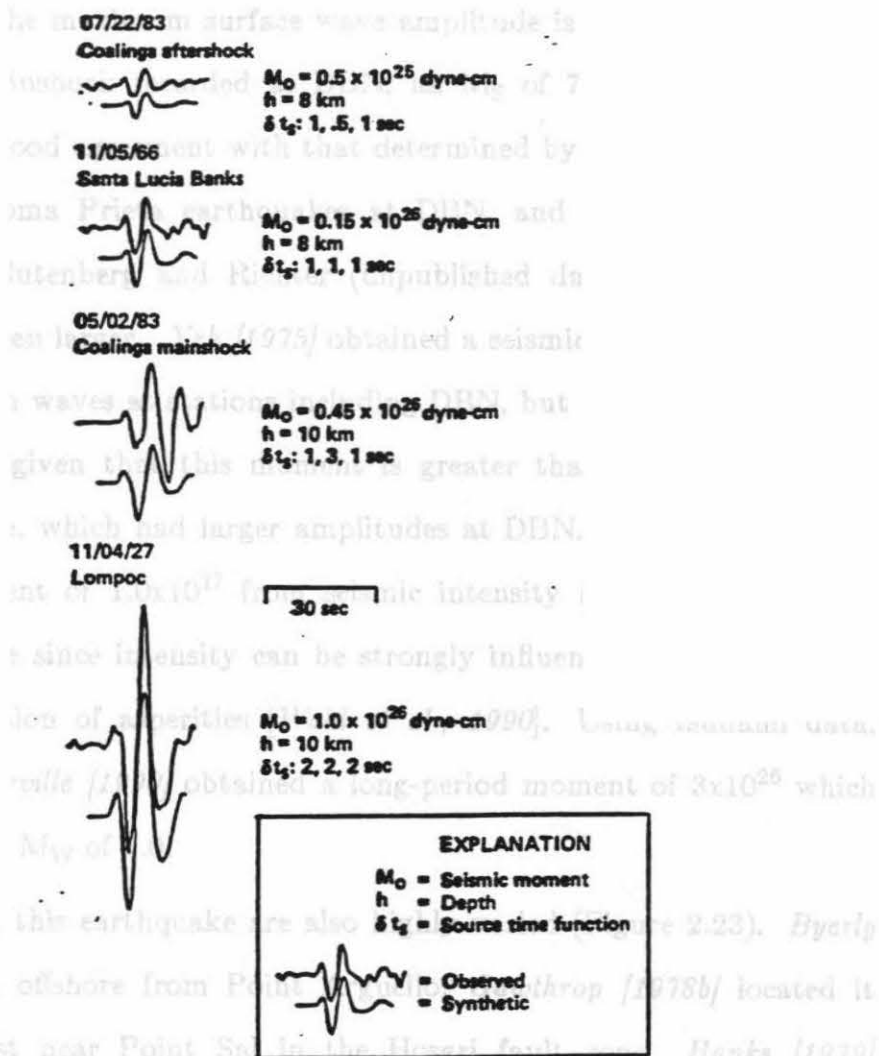


Figure 2.22
Long-period P data and synthetics for the Lompoc, Santa Lucia Banks, and Coalinga (mainshock and largest aftershock) at DBN.

body waves. If the maximum surface wave amplitude is compared to that of the Coalinga mainshock recorded at DBN, an M_S of 7.0 is obtained. This magnitude is in good agreement with that determined by comparing the Lompoc and 1989 Loma Prieta earthquakes at DBN, and with the magnitude determined by Gutenberg and Richter (unpublished data). Other moment estimates have been larger. *Yeh [1975]* obtained a seismic moment of 4.5×10^{26} based on Rayleigh waves at stations including DBN, but this moment appears to be unreliable given that this moment is greater than that of the Loma Prieta earthquake, which had larger amplitudes at DBN. *Hanks et al. [1975]* obtained a moment of 1.0×10^{27} from seismic intensity reports, which again may be unreliable since intensity can be strongly influenced by local geology and the distribution of asperities [*Wald et al., 1990*]. Using tsunami data, *Satake and Somerville [1990]* obtained a long-period moment of 3×10^{26} which corresponds to an M_W of 7.0.

Locations of this earthquake are also highly varied (Figure 2.23). *Byerly [1930]* located it offshore from Point Arguello. *Gawthrop [1978b]* located it just off the coast near Point Sal in the Hosgri fault zone. *Hanks [1979]* located it offshore intermediate to the other locations. A comparison of S-P times for the Lompoc, Coalinga, and Santa Lucia Banks earthquakes (Figure 2.20) combined with the SSS-S times and regional data of *Helmberger et al. [1990]* place the Lompoc earthquake 40 km west of Point Conception at 34.35°N and 120.9°W . This location is in agreement with that of *Satake and Somerville [1990]*.

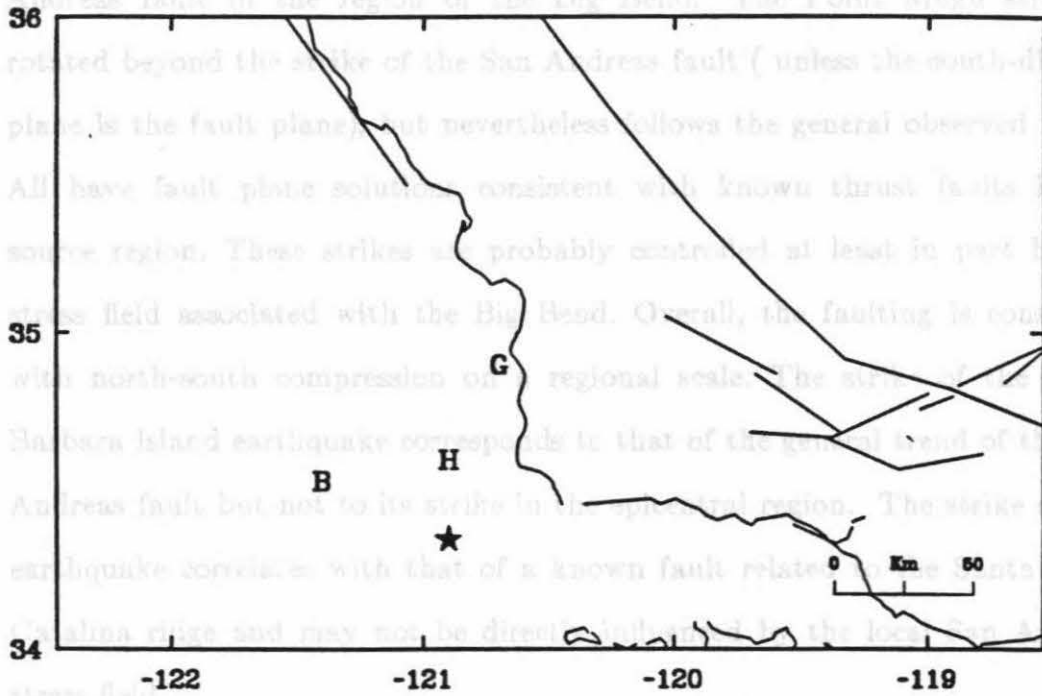


Figure 2.23
Map showing various locations for the Lompoc earthquake. The star is this study, B is *Byerly [1980]*, H is *Hanks [1979]*, and G is *Gawthrop [1978b]*. *Hanks's [1979]* and *southeast of Byerly's [1980]* locations.

2.8 Discussion and Conclusions

The strikes of the thrust events studied rotate southwestward as the epicenters move southward. If we assume the north-dipping plane is the fault plane, then the strikes correspond roughly to the changing strike of the San Andreas fault in the region of the Big Bend. The Point Mugu strike is rotated beyond the strike of the San Andreas fault (unless the south-dipping plane is the fault plane), but nevertheless follows the general observed trend. All have fault plane solutions consistent with known thrust faults in the source region. These strikes are probably controlled at least in part by the stress field associated with the Big Bend. Overall, the faulting is consistent with north-south compression on a regional scale. The strike of the Santa Barbara Island earthquake corresponds to that of the general trend of the San Andreas fault but not to its strike in the epicentral region. The strike of this earthquake correlates with that of a known fault related to the Santa Cruz-Catalina ridge and may not be directly influenced by the local San Andreas stress field.

The 1927 Lompoc earthquake is also a thrust event with a strike of 340° . Synthetic seismograms and comparisons of amplitudes with similar events suggest that the seismic moment is 1.0×10^{26} dyne cm, somewhat smaller than previous estimates. The S-P times indicate an offshore location south of *Hanks's [1979]* and southeast of *Byerly's [1930]* locations.

Based on the reported M_L 's, we would expect the Point Mugu earthquake to have the largest seismic moment and the Santa Barbara earthquake to have the smallest. This is not what was observed. The November Santa Barbara Island data, the pattern at GOL remains but DUG appears to be less reliable. Perhaps it would be better to say that the synthetics at DUG are moments. The Santa Barbara earthquake has an intermediate moment, and

the Point Mugu and October Santa Lucia Banks events have the smallest moments. There is a much better correlation between moment and M_S . The Santa Lucia Banks events have M_S 's of 5.1 and 6.1 (ISC). That of the Point Mugu earthquake is 5.2 (NOAA). M_S for the Santa Barbara and Santa Barbara Island earthquakes are 5.6 and 5.9 respectively (both from NEIS). These results suggest that M_S is a better parameter than M_L for determining the long-period energy release of earthquakes in this magnitude range. (Figure

2.24) In modeling source parameters, large variations, sometimes as large as 50%, from the average moment are often observed at some stations. Changing the source parameters usually does not reduce the scatter. Since we have modeled a number of earthquakes with almost identical paths with respect to teleseismic stations, we have the opportunity to study the amplitude variations as a function of the station. The amplitudes may be affected by the path but the effects should be the same for every event. Four of the earthquakes studied were well recorded teleseismically. We will look at all stations which recorded three or more of these events, a total of 12 stations- 5 teleseismic and 7 regional- and also look for regional or azimuthal trends using the complete data set. At regional distances three stations (ALQ, BKS and COR) showed a high degree of variability in the ratio of observed and theoretical amplitudes. The synthetic amplitudes at GOL were consistently smaller than the data, although the ratio varied considerably. TUC showed the opposite trend with the synthetics being consistently larger than the data. DUG and PAS usually gave synthetic amplitudes that were close to the observed value, but in each case there was one event which did not. When we add the Santa Barbara Island data, the pattern at GOL remains but DUG appears to be less reliable. Perhaps it would be better to say that the synthetics at DUG are

consistently greater than or equal to the data. Three of the teleseismic stations (COP, PTO and TOL) show a high degree of scatter. The synthetic amplitudes at CAR, which have a maximum difference of 20%, are generally close to the observed amplitudes. At GDH the synthetics tend to be greater than or equal to the data but the actual ratios are more varied than at CAR. The station by station amplitude ratios are shown in Figure 2.24a.

When the amplitude ratios are plotted as a function of azimuth (Figure 2.24b) there are some regional trends but they are not strong enough to be conclusive. Stations to the northwest (Japan and Alaska) tend to have synthetic amplitudes less than or equal to the observed amplitudes, but there is a wide range of values. The scatter for South American stations is less than for other regions but the synthetic amplitudes are equally likely to be larger or smaller than the data. At stations in the eastern United States and Canada, the synthetics are more likely to be larger than the data, but again there are exceptions to this trend. European and northern Canadian stations show a fair amount of scatter in the amplitude ratios.

In summary, we have found that the nearshore region of south-central California is dominated by thrust faulting. The average strike is roughly east-west, implying north-south compression, but the strike seems to be controlled at least in part by the stress field associated with the San Andreas fault. Complex sources appear to be fairly common for moderate earthquakes in this region. The fit of the synthetic seismograms to the data was improved by allowing the Green's functions to vary with station and epicentral locations as well as distance. By studying the events as a group, we were able to determine some characteristics of the regional velocity structure and whether amplitude mismatches are consistent at a number of stations and azimuths.

In general, there were only weak regional trends.

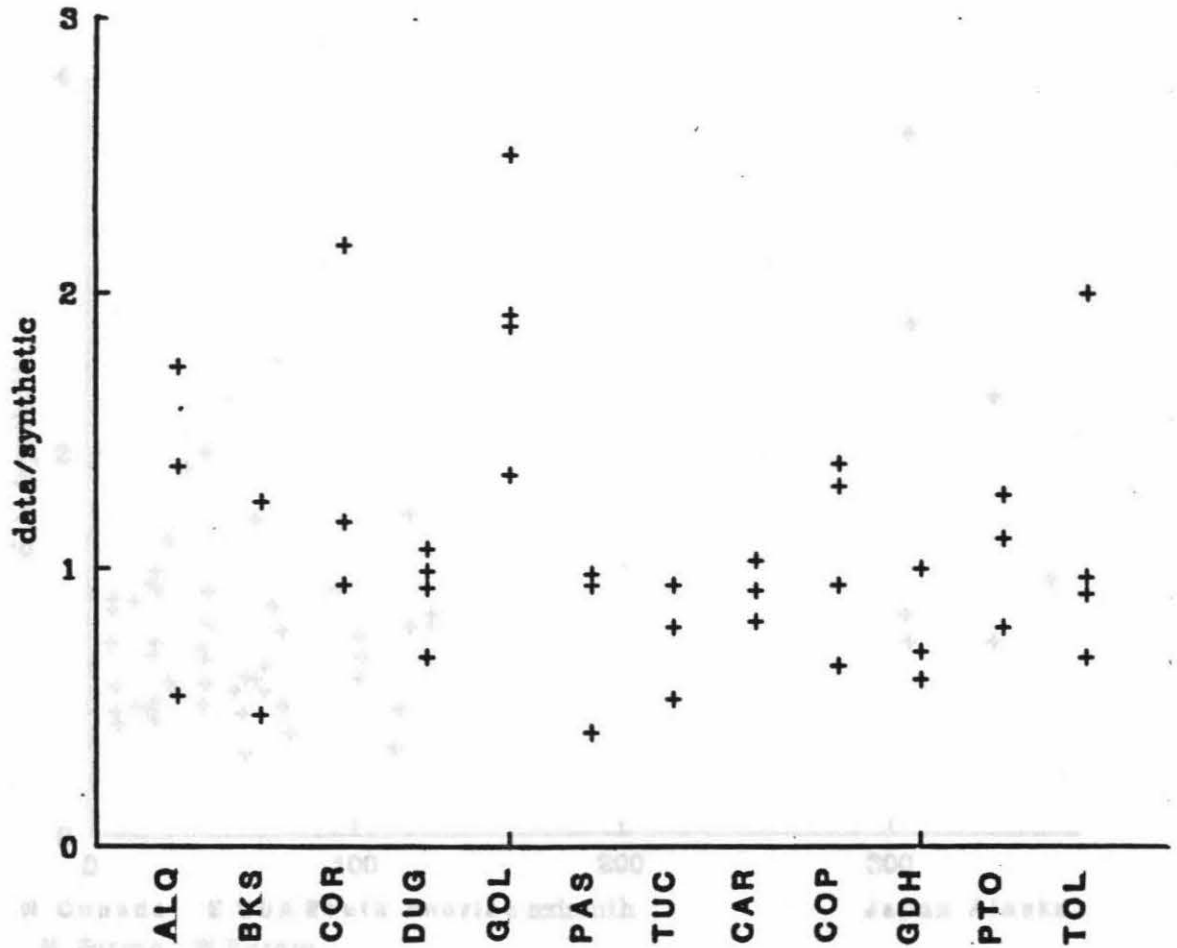


Figure 2.24a

Ratio of observed amplitudes to synthetic seismograms (vertical component) as a function of station. The radial component is used at PAS because the vertical is unavailable.

3.1.4 Introduction

On 2 May 1983 a large (M_L 6.7) earthquake occurred near Coalinga in an area where there were no mapped faults thought to be capable of producing such a large event. This earthquake and many of its larger aftershocks were predominantly thrust events. These earthquakes were located further north than those discussed in previous chapters and occurred in the central coast near the San Andreas Fault (Figure 3.1). The mainshock occurred on the east limb of the Coalinga anticline, and it is believed that the earthquakes were caused by active sliding on a blind thrust much as the Whittier Narrows sequence occurred. The mainshock has been well studied by others (Choy, 1983) within a minute. There were several aftershocks of magnitude 5 or greater of which I will discuss some of the better recorded ones. All were well recorded regularly spaced stations. Records are available only for the N Canada E USA South America azimuth For the 22 July Japan Alaska N Europe W Europe

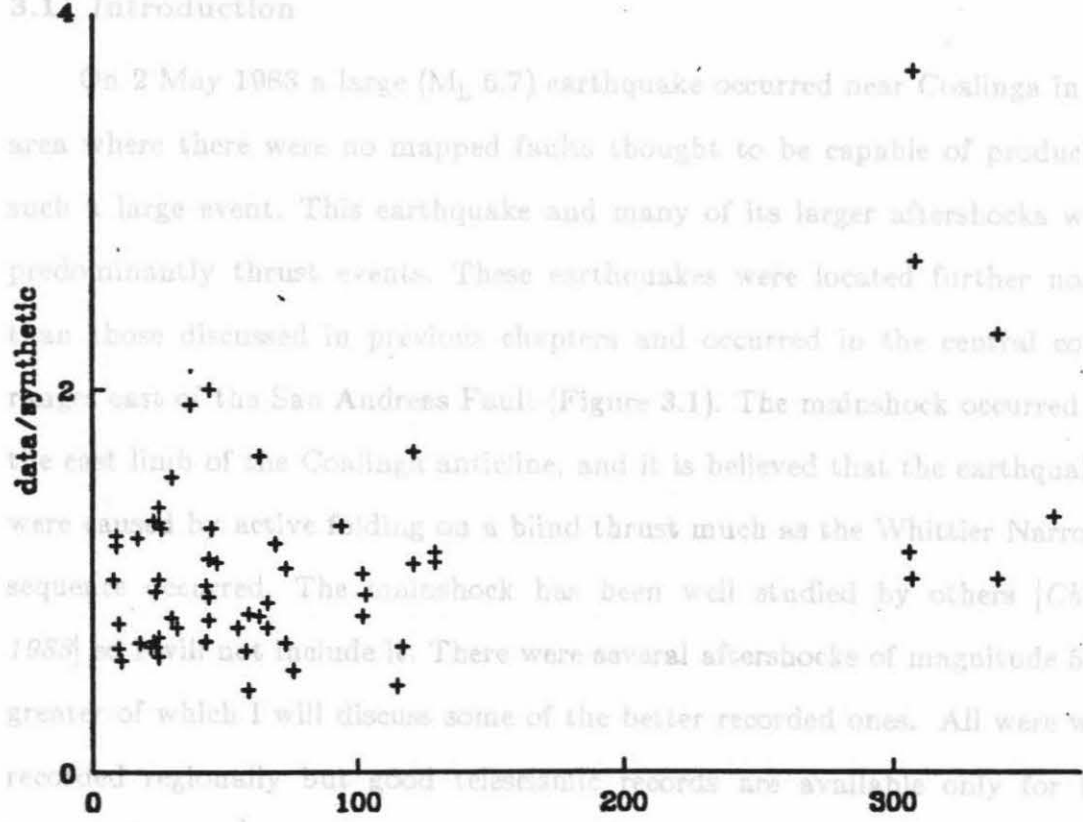


Figure 2.24b

Ratio of observed amplitudes to synthetic seismograms as a functions of azimuth for distances greater than 30°.

3.2 22 July

Chapter 3

Aftershocks of the 1983 Coalinga Earthquake

3.1 Introduction

On 2 May 1983 a large (M_L 6.7) earthquake occurred near Coalinga in an area where there were no mapped faults thought to be capable of producing such a large event. This earthquake and many of its larger aftershocks were predominantly thrust events. These earthquakes were located further north than those discussed in previous chapters and occurred in the central coast ranges east of the San Andreas Fault (Figure 3.1). The mainshock occurred on the east limb of the Coalinga anticline, and it is believed that the earthquakes were caused by active folding on a blind thrust much as the Whittier Narrows sequence occurred. The mainshock has been well studied by others [Choy, 1983] so I will not include it. There were several aftershocks of magnitude 5 or greater of which I will discuss some of the better recorded ones. All were well recorded regionally but good teleseismic records are available only for the largest aftershock which occurred on 22 July. For the 22 July aftershock I can independently determine the depth, but for all others I use Eaton's [1983b] depths obtained from local data.

3.2 22 July

The best recorded aftershock was an M_L 6.0 event which occurred on 22 July. It occurred at a depth of 7.5 km, and, like the mainshock, was a thrust event. By modeling the regional data, we obtain a focal mechanism with strike 355° , dip 38° , and rake 100° . This solution is compatible with Eaton's

sec. The results of the regional modeling are shown in Figure 3.2.

Both the long- and short-period teleseismic records can be well modeled using the M_0 fault parameters and *Estes's* [1989b] depth, but there are a number of complexities regarding the source time function. The periods of the long-period records show a definite azimuthal trend with the period increasing from northwest to southeast (Figure 3.3). Records in Alaska (COL) and Europe (KBS, KEV, ...) agree with the regional time function. Eastern United States stations (WES, SCP, BLA, FVM) require a longer time function with $\delta_1 = 1$ and $\delta_2 = \delta_3 = 3$. A straight doubling of the original time function does not work well, as it results in a direct P arrival that is smaller than is observed. The only South American station (BOG) requires an even longer time function, with δ_2 increased to 5 seconds. The only station which does not follow this trend is SJG, which can be modeled with the shortest time function. The observed pattern of azimuthal dependence suggests that the fault rupture propagated toward the northwest. The teleseismic long-

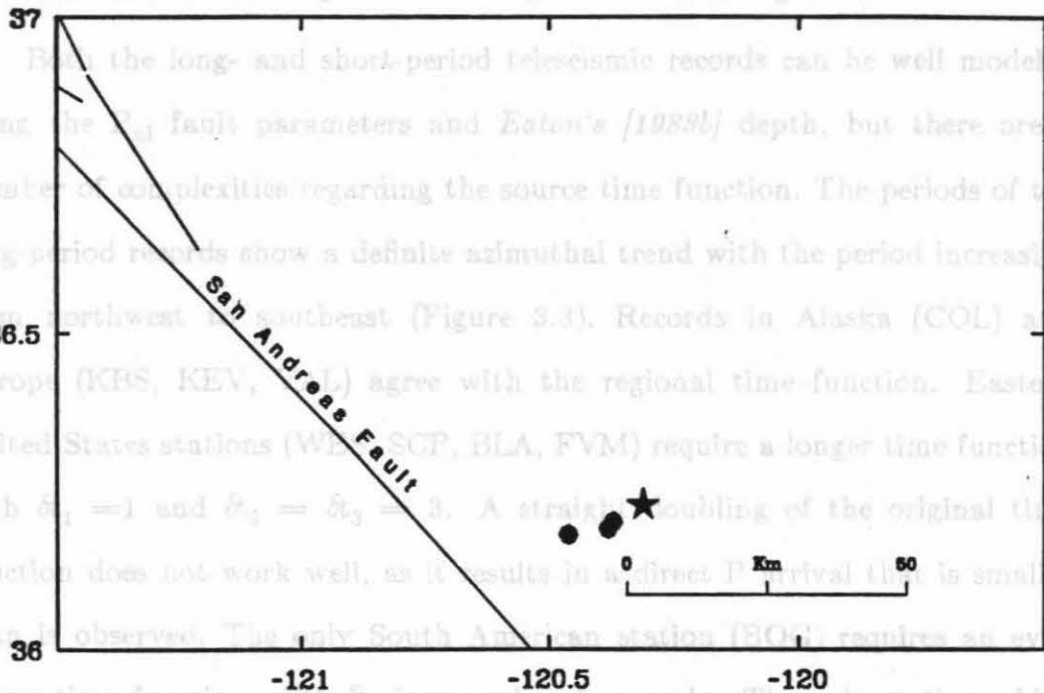


Figure 3.1

Locations of the Coalinga mainshock (star) and the aftershocks used in this study. The azimuthal variation of frequency is not seen in the short-period

[1983b] first motion fault plane solution determined from local data. The long-period seismic moment is 7.9×10^{24} dyne cm. We obtained the best results using a trapezoidal time function with $\delta t_1 = \delta t_3 = 1$ sec, and $\delta t_2 = 0.5$ sec. The results of the regional modeling are shown in Figure 3.2.

Both the long- and short-period teleseismic records can be well modeled using the P_{nl} fault parameters and *Eaton's [1983b]* depth, but there are a number of complexities regarding the source time function. The periods of the long-period records show a definite azimuthal trend with the period increasing from northwest to southeast (Figure 3.3). Records in Alaska (COL) and Europe (KBS, KEV, VAL) agree with the regional time function. Eastern United States stations (WES, SCP, BLA, FVM) require a longer time function with $\delta t_1 = 1$ and $\delta t_2 = \delta t_3 = 3$. A straight doubling of the original time function does not work well, as it results in a direct P arrival that is smaller than is observed. The only South American station (BOG) requires an even longer time function, with δt_2 increased to 5 seconds. The only station which does not follow this trend is SJG, which can be modeled with the shortest time function. The observed pattern of azimuthal dependence suggests that the fault rupture propagated toward the northwest. The teleseismic long-period moment of 7.0×10^{24} is in good agreement with the regional moment.

The azimuthal variation of frequency is not seen in the short-period records (Figure 3.4) where one would expect it to be stronger, suggesting that most of the short-period energy release came from one or more asperities. The short-period synthetics fit best with a two source solution of total duration about 0.75 sec less than the shortest long-period solution and with a depth of 6 km. Within the resolving capabilities of the data, both subevents have identical mechanisms equal to that determined by modeling long-period

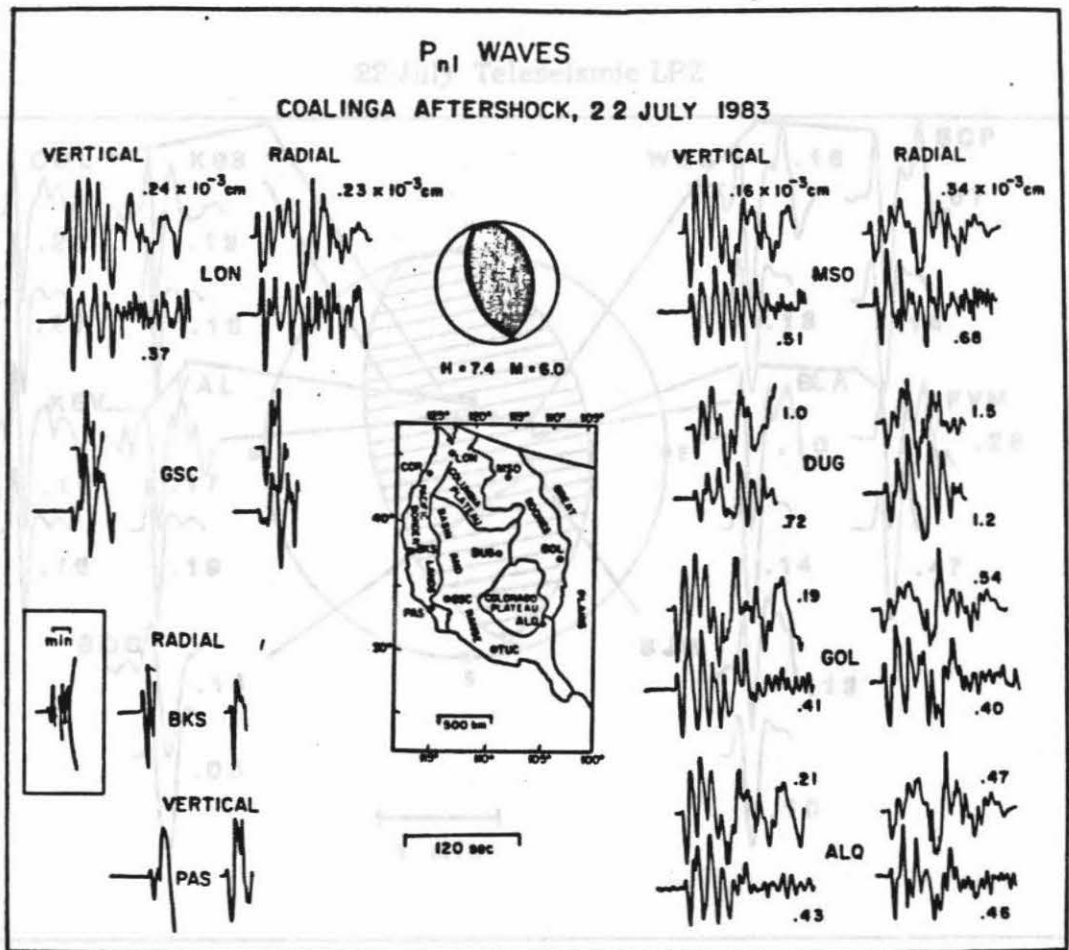


Figure 3.2

Regional data (lower) and synthetics (upper) for the 22 July aftershock. The amplitudes are given in units of 10^{-3} cm and have the instrument magnification removed.

22 July Teleseismic SPZ

22 July Teleseismic LPZ

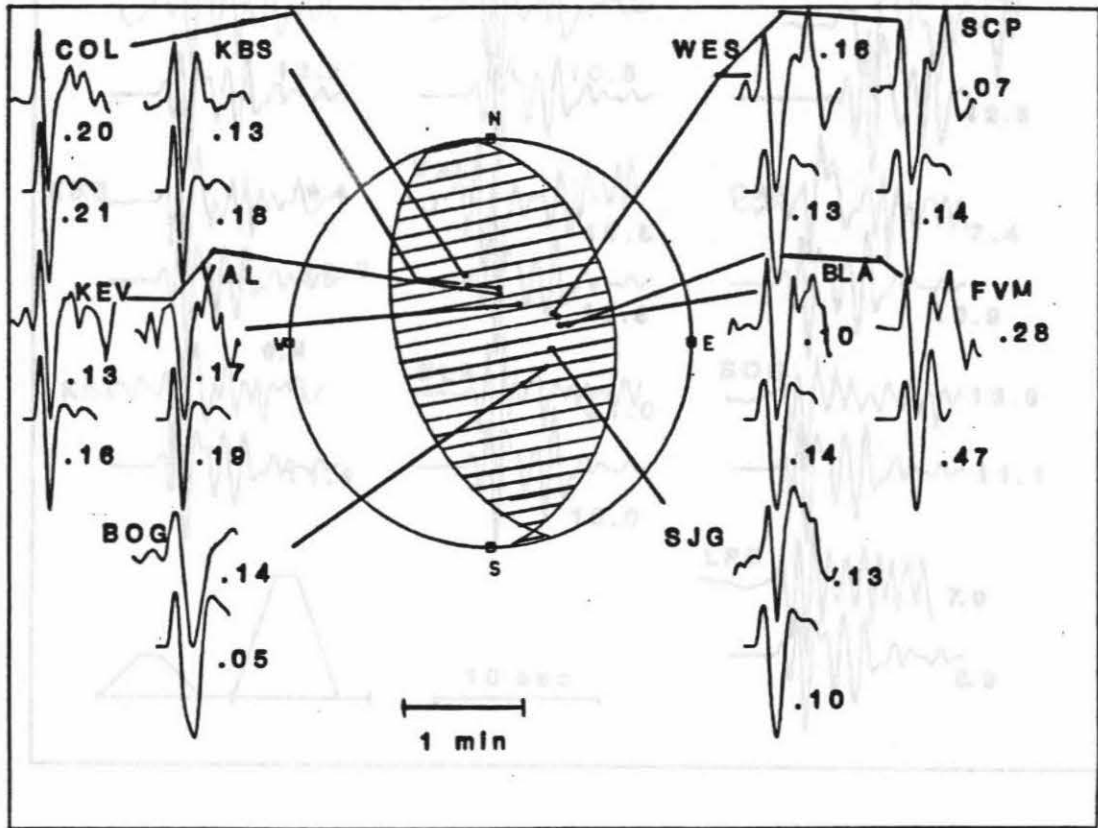
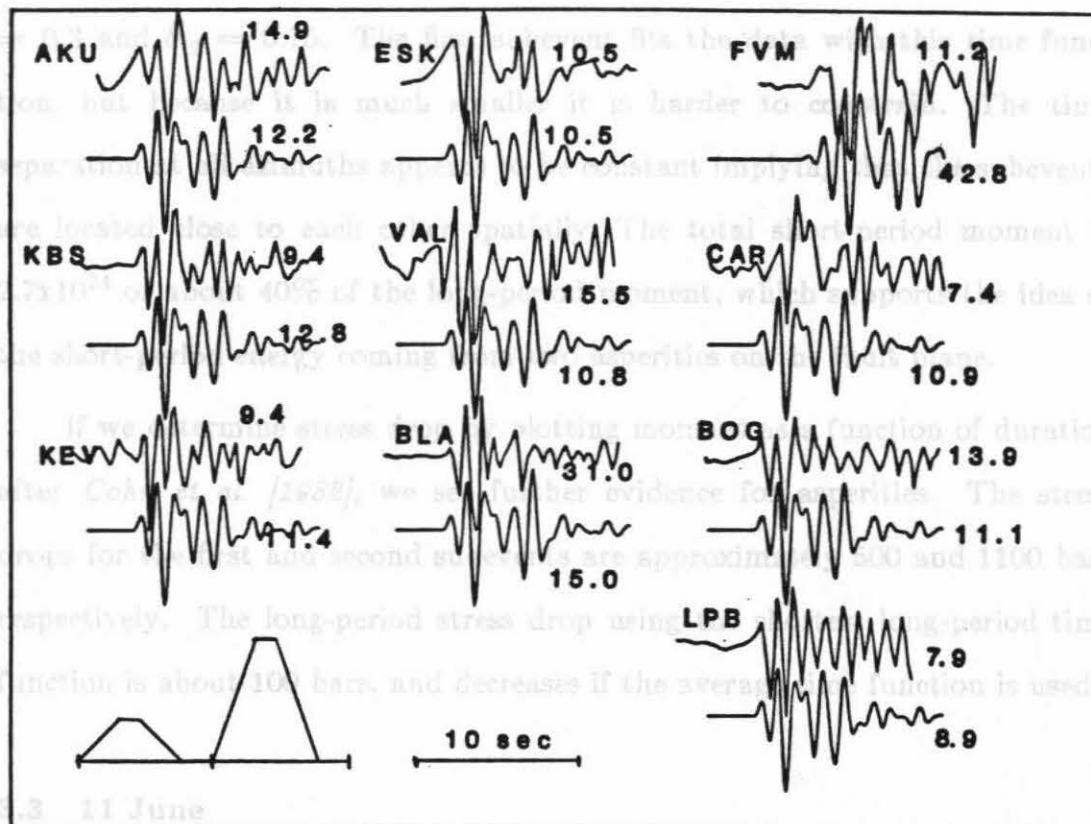


Figure 3.3

Long-period teleseismic data (upper) and synthetics (lower) for the 22 July aftershock. The amplitudes are as in Figure 3.2. Amplitudes are in units of 10^{-8} cm and have the instrument magnification removed.

records. The second subevent occurred 1.0 seconds after the first and was 3 times larger. For the second subevent the time function of $\Delta_1 = \Delta_2$

22 July Teleseismic SPZ



11 June

The aftershock which occurred on 11 June was very shallow, with a depth of 2.4 km, and had a magnitude of 5.2. I used Eaton's [1983b] local first motion solution as the starting point in the modeling procedure, but this

Figure 3.4

Short-period data (upper) and (synthetics) for the 22 July aftershock. The tic marks on the time function are at 1 sec intervals. Amplitudes are in units of 10^{-6} cm and have the instrument magnification removed.

results are shown in Figure 3.5. The amplitude at BKS suggests that it is near nodal, but the waveform does not appear to be nodal and the amplitude fit cannot be improved without drastically reducing the waveform fit of the synthetic seismogram to the data.

records. The second subevent occurred 1.0 seconds after the first and was 3 times larger. For the second subevent we obtain a time function of $\delta t_1 = \delta t_3 = 0.3$ and $\delta t_2 = 0.15$. The first subevent fits the data with this time function, but because it is much smaller it is harder to constrain. The time separation at all azimuths appears to be constant implying that the subevents are located close to each other spatially. The total short-period moment is 2.7×10^{24} or about 40% of the long-period moment, which supports the idea of the short-period energy coming from two asperities on the fault plane.

If we determine stress drop by plotting moment as a function of duration after *Cohn et al. [1982]*, we see further evidence for asperities. The stress drops for the first and second subevents are approximately 500 and 1100 bars respectively. The long-period stress drop using the shortest long-period time function is about 100 bars, and decreases if the average time function is used.

3.3 11 June

The aftershock which occurred on 11 June was very shallow, with a depth of 2.4 km, and had a magnitude of 5.2. I used *Eaton's [1983b]* local first motion solution as the starting point in the modeling procedure, but this model resulted in the wrong first motion at GOL and too small a Pn at BKS. Better fitting synthetics were obtained using a strike of 197° , dip 38° , and rake 70° . The long-period seismic moment is 1.5×10^{24} dyne cm. The modeling results are shown in Figure 3.5. The amplitude at BKS suggests that it is near nodal, but the waveform does not appear to be nodal and the amplitude fit cannot be improved without drastically reducing the waveform fit of the synthetic seismogram to the data.

3.4 2 July

The M_L 5.4 aftershock of 9 July occurred at a depth of 9 km and was

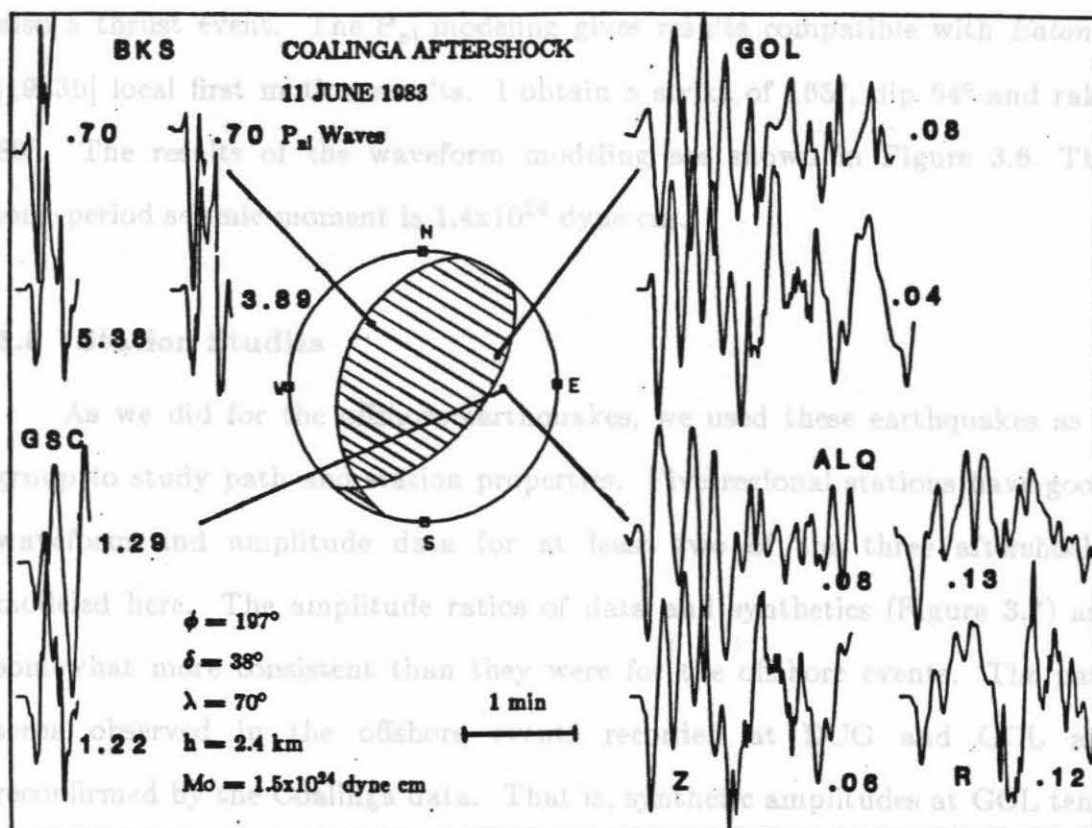


Figure 3.5

Regional data (upper) and synthetics (lower) for the 11 June aftershock. The amplitudes are as in Figure 3.2.

By comparing the observed and theoretical travel times of P_n , we are able to determine the average μ ratio along the path from source to receiver. Because the epicenters are closer together than the offshore epicenters were, we expect to see less scatter in the results, and in general, we do (Figure 3.8). The two July aftershocks were located very close together and give

3.4 9 July

The M_L 5.4 aftershock of 9 July occurred at a depth of 9 km and was also a thrust event. The P_{nl} modeling gives results compatible with *Eaton's* [1983b] local first motion results. I obtain a strike of 165° , dip 54° and rake 80° . The results of the waveform modeling are shown in Figure 3.6. The long-period seismic moment is 1.4×10^{24} dyne cm.

3.5 Station Studies

As we did for the offshore earthquakes, we used these earthquakes as a group to study path and station properties. Five regional stations have good waveform and amplitude data for at least two of the three aftershocks modeled here. The amplitude ratios of data and synthetics (Figure 3.7) are somewhat more consistent than they were for the offshore events. The patterns observed in the offshore events recorded at DUG and GOL are reconfirmed by the Coalinga data. That is, synthetic amplitudes at GOL tend to be too small while those at DUG are too large. DUG shows very little scatter from event to event and also between the vertical and radial components. At ALQ the synthetics are too small and there is much less scatter in the ratios than at most other stations. At BKS (radial component) the synthetics are also too small, but with highly variable ratios. The amplitude ratios at LON showed no obvious pattern.

By comparing the observed and theoretical travel times of P_n , we are able to determine the average moho velocity along the path from source to receiver. Because the epicenters are closer together than the offshore epicenters were, we expect to see less scatter in the results, and in general, we do (Figure 3.8). The two July aftershocks were located very close together and give

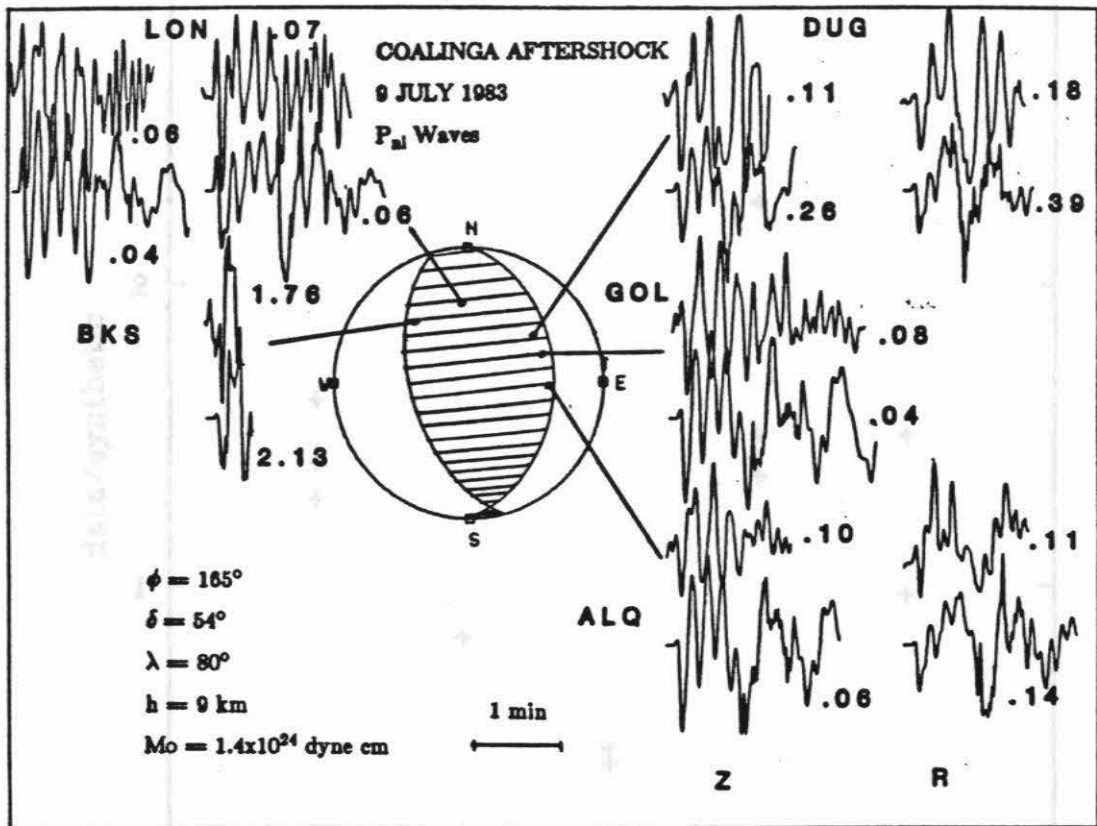


Figure 3.6

Regional data and synthetics for the 9 July aftershock. The format is the same as Figure 3.5.

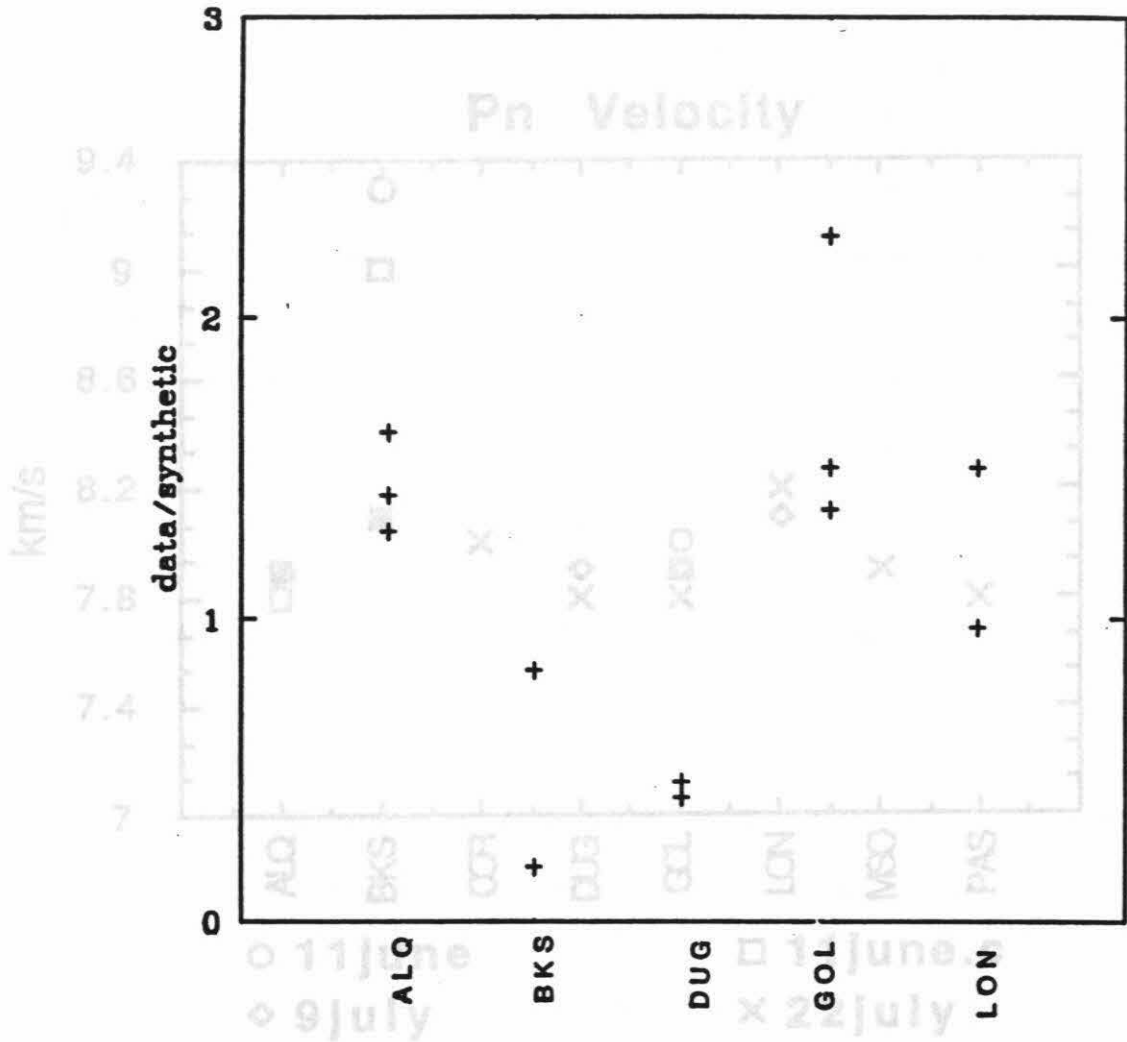


Figure 3.7

Ratio of observed to synthetic amplitudes (vertical component) as a function of station.

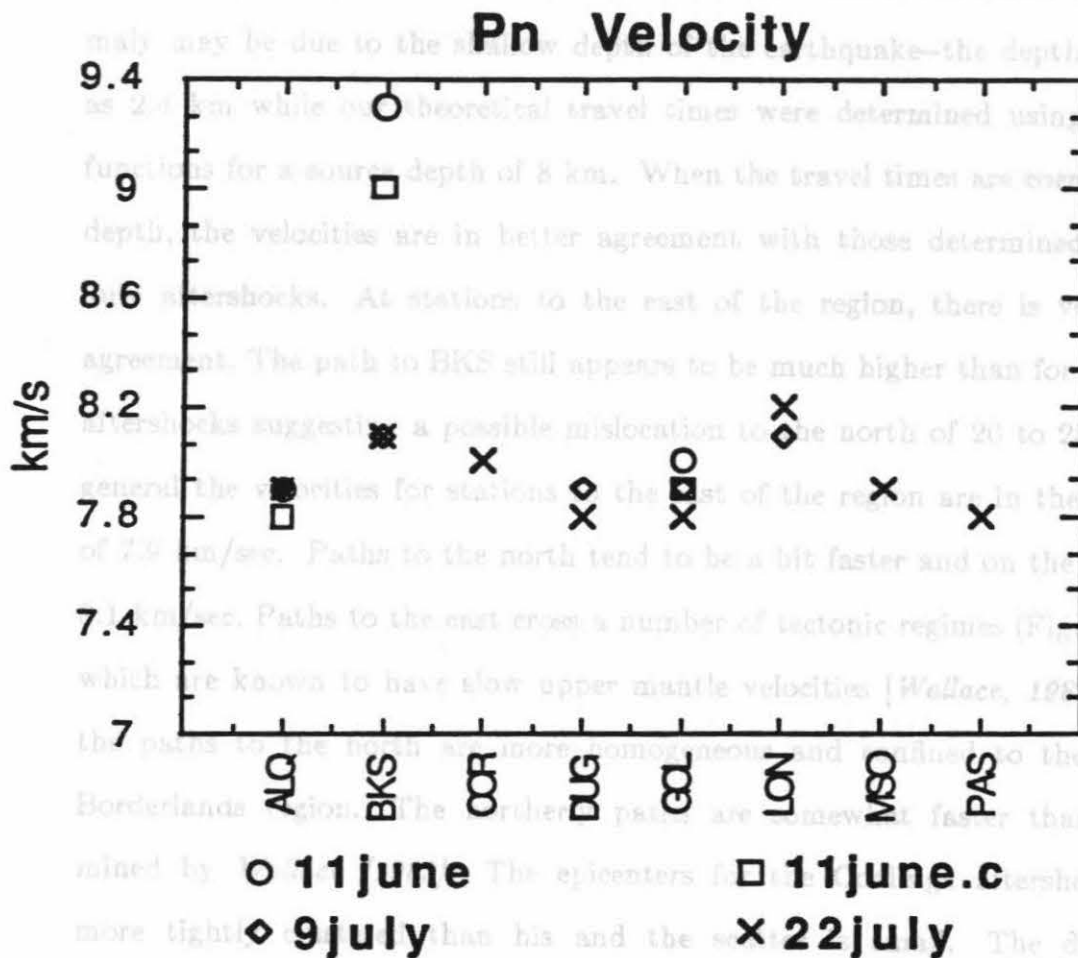


Figure 3.8

Moho velocities which best fit the observed Pn travel times. 11june.c is corrected for depth.

3.6 Discussion and Conclusions

almost identical velocities at all stations which recorded both. Higher velocities were generally determined for the June event. Part of the travel time anomaly may be due to the shallow depth of the earthquake—the depth is given as 2.4 km while our theoretical travel times were determined using Green's functions for a source depth of 8 km. When the travel times are corrected for depth, the velocities are in better agreement with those determined for the July aftershocks. At stations to the east of the region, there is very good agreement. The path to BKS still appears to be much higher than for the July aftershocks suggesting a possible mislocation to the north of 20 to 25 km. In general the velocities for stations to the east of the region are in the vicinity of 7.9 km/sec. Paths to the north tend to be a bit faster and on the order of 8.1 km/sec. Paths to the east cross a number of tectonic regimes (Figure 2.18) which are known to have slow upper mantle velocities [Wallace, 1983], while the paths to the north are more homogeneous and confined to the Pacific Borderlands region. The northerly paths are somewhat faster than determined by Wallace [1983]. The epicenters for the Coalinga aftershocks are more tightly clustered than his and the scatter is small. The difference between the models may be due to the way he divided the region or to a difference in the paths studied.

3.6 Discussion and Conclusions

The aftershocks of the 1983 Coalinga earthquake studied here were all thrust events on moderately dipping faults. Details of the rupture process could be determined only for the largest aftershock, which occurred on 22 July. It appears to be a northwestward propagating fault with most of the short period energy coming from two asperities on the fault plane.

The amplitude ratios of data to synthetics reconfirmed patterns seen in the offshore events discussed in Chapter 2. In general synthetics at GOL, BKS and ALQ tend to be too small while those at DUG tend to be too large. Other stations showed no obvious trend.

4.1 The difference between theoretical and observed Pn travel times were used to calculate upper mantle velocities for paths to stations in the western United States. Paths to the east were on average 0.2 km/sec slower than those to the north. *body that has produced many nodders to large earth- quakes in the west (1968 Borrego Mountain, 1969 Colorado Mountain, 1970*

Chapter 4

The 1987 Superstition Hills Earthquakes

4.1 Introduction

The Superstition Hills earthquakes of 24 November 1987, hereafter referred to as EQ1 (at 0153 UT) and EQ2 (at 1316 UT), occurred near the edge of a complex basin that has produced many moderate to large earthquakes in the past (1968 Borrego Mountain, 1969 Coyote Mountain, 1979 Imperial Valley, 1981 Westmorland). Field investigations and aftershock patterns (Figure 4.1) indicate that EQ1, which occurred a few kilometers SW of the southern end of the Salton Sea, occurred on a previously unknown NE-striking left-lateral fault. EQ2 occurred 10 km SW of EQ1 and ruptured the right-lateral Superstition Hills fault, which is roughly perpendicular to the fault that produced EQ1. The epicenter of EQ2 is located at or near the junction of the two faults. The aftershocks of EQ2 line up roughly parallel to the Superstition Hills fault but are located between the Superstition Hills and Superstition Mountain faults (Figure 4.1).

4.2 Data Set

Both November events as well as a smaller (M_L 4.9) aftershock that occurred on 28 January 1988 (EQ3) were well recorded at Pasadena (PAS), about 250 km NW of the epicenters (Figures 4.2 and 4.3). Because EQ3 was a small event, it was recorded on scale by more Caltech stations at local distances (< 200 km) than were EQ1 and EQ2, so its depth and focal mechanism are well determined from local data. EQ3 can be well modeled at PAS

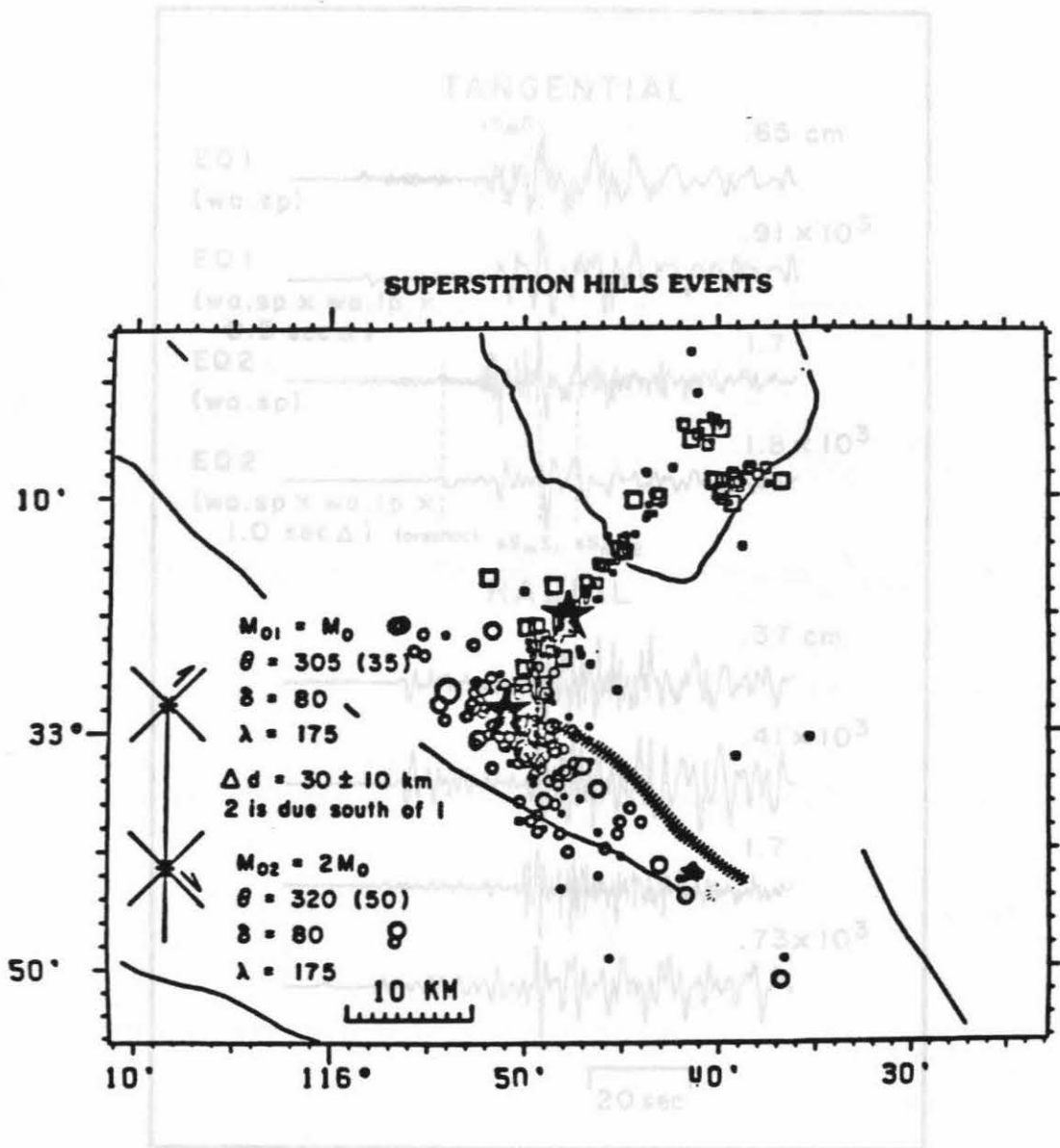


Figure 4.1

Locations of the Superstition Hills events (modified from *Magistrale et al., 1989*). The squares represent events occurring before EQ2 and circles are events occurring after EQ2. The large stars are EQ1 and EQ2 (EQ2 is SW of EQ1). The hatched line shows the extent of rupture on the Superstition Hills fault. In the lower left-hand corner, the approximate locations of the 2 subevents of EQ2 are shown. The arrows represent the probable direction of rupture based on strong motion data [*Wald and Sommerville, 1988*].

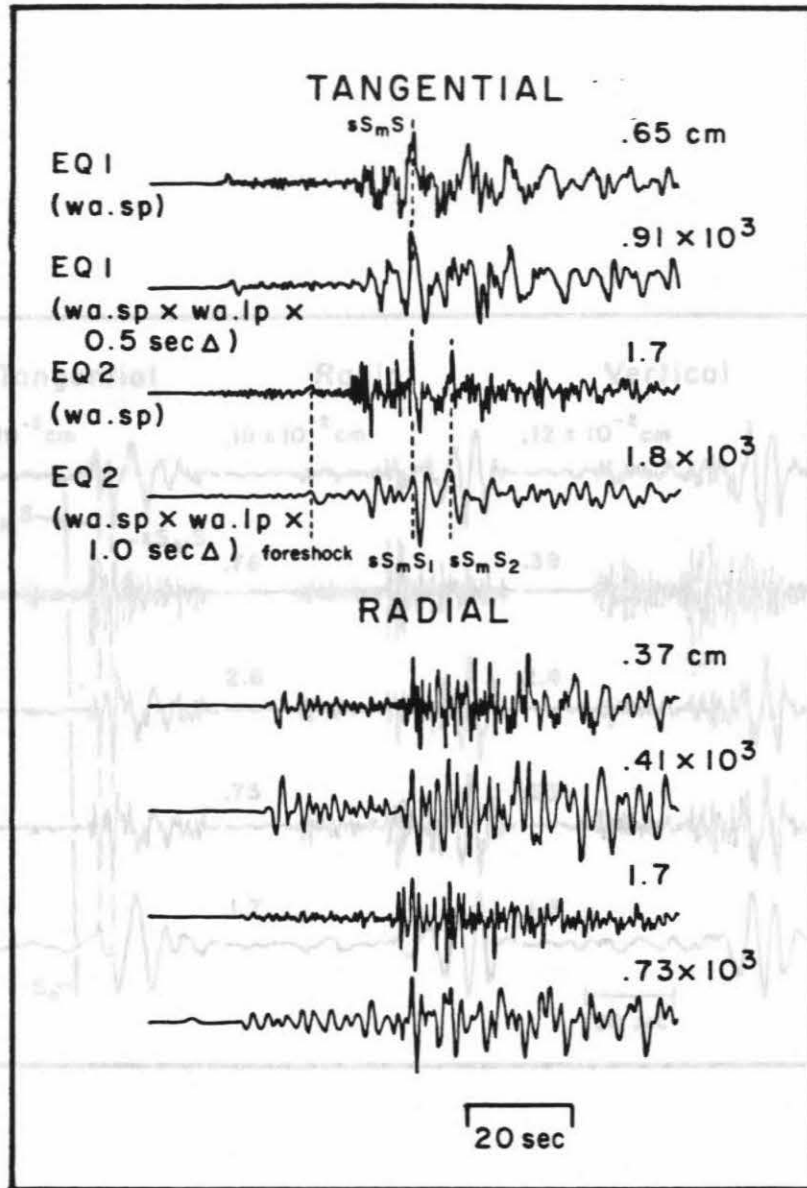


Figure 4.2

Tangential and radial data for EQ1 and EQ2 recorded at PAS. The upper trace is EQ1 raw data (recorded on a short-period Wood-Anderson instrument); the second trace is EQ1 data convolved with a long-period Wood-Anderson instrument and a 0.5 sec triangular filter; the third is EQ2 data; the fourth is EQ2 convolved with a long-period Wood-Anderson instrument and a 1 sec triangle.

using regional Green's functions for the path from Imperial Valley to Pasadena obtained by modeling regional Love waves for a large number of past events in the Imperial Valley regions [Ho-Liu and Heimberger, 1989]. In this way we can use EQ3 to help constrain the faulting parameters of EQ1

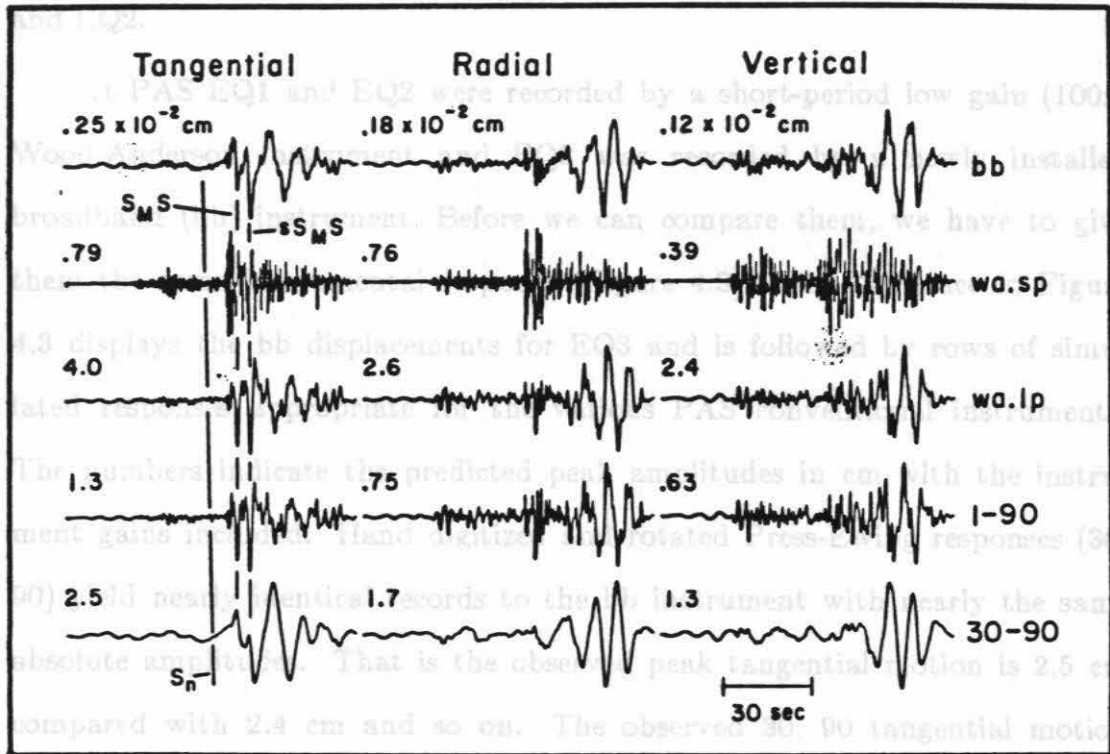


Figure 4.3

Tangential (left), radial (middle), and vertical (right) components of EQ3 convolved with various instrument responses. Wa-sp is short-period Wood-Anderson; wa-lp is long-period Wood-Anderson; lp3090 is Press-Ewing.

recorded on a short-period Wood-Anderson instrument (gain=100). Presumably, the shift in corner frequency is off-set by the instrumental response and the difference in strength is handled by the gain differential [Ho-Liu and Heimberger, 1989]. Such a comparison is given in Figure 4.4 along with a theoretical response. The depth phase s_s appears clear for both events and indicates a

using regional Green's functions for the path from Imperial Valley to Pasadena obtained by modeling regional Love waves for a large number of past events in the Imperial Valley regions [Ho-Liu and Helmberger, 1989]. In this way we can use EQ3 to help constrain the faulting parameters of EQ1 and EQ2.

At PAS EQ1 and EQ2 were recorded by a short-period low gain (100x) Wood-Anderson instrument and EQ3 was recorded by a newly installed broadband (bb) instrument. Before we can compare them, we have to give them the same instrumental response (Figure 4.3). The top trace in Figure 4.3 displays the bb displacements for EQ3 and is followed by rows of simulated responses appropriate for the various PAS conventional instruments. The numbers indicate the predicted peak amplitudes in cm with the instrument gains included. Hand digitized and rotated Press-Ewing responses (30, 90) yield nearly identical records to the bb instrument with nearly the same absolute amplitudes. That is the observed peak tangential motion is 2.5 cm compared with 2.4 cm and so on. The observed 30, 90 tangential motion agrees well with that of similar magnitude Brawley events and can be modeled [Ho-Liu and Helmberger, 1989]. Unfortunately, the long-period recordings of EQ1 and EQ2 are off-scale.

In many situations, an aftershock recorded on a long-period Wood-Anderson instrument (gain=1700) looks very similar to the main event recorded on a short-period Wood-Anderson instrument (gain=100). Presumably, the shift in corner frequency is off-set by the instrumental response and the difference in strength is handled by the gain differential [Ho-Liu and Helmberger, 1989]. Such a comparison is given in Figure 4.4 along with a theoretical response. The depth phase sS appears clear for both events and indicates a

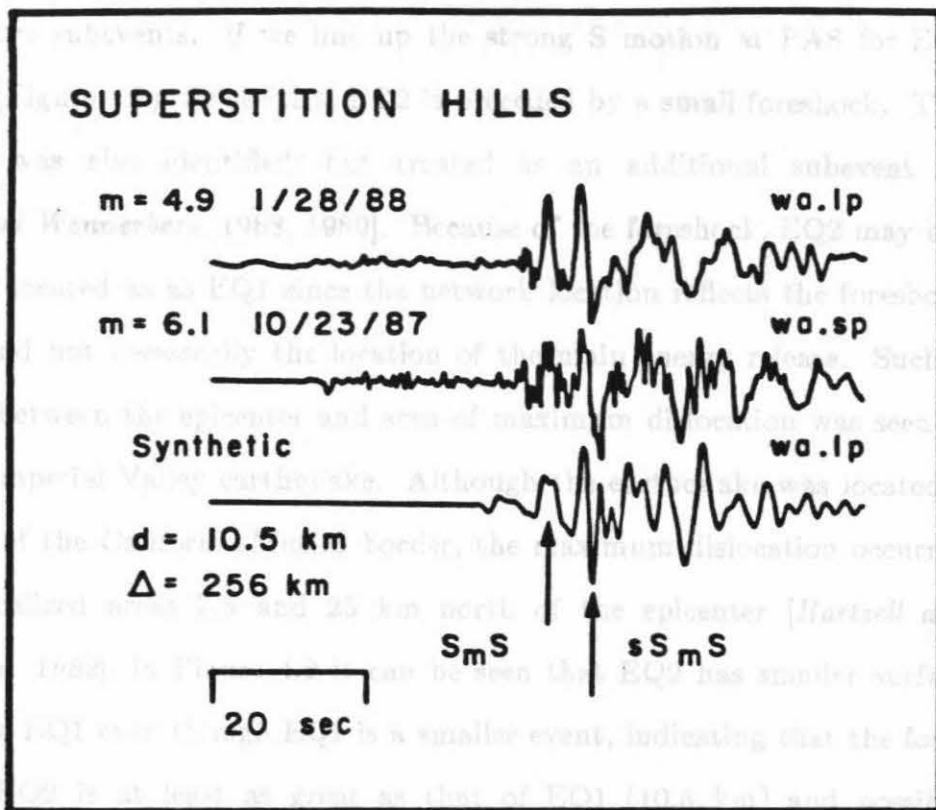


Figure 4.4 EQ1 and EQ3 at PAS (tangential component). The lower trace is the synthetic seismogram for EQ3, but also fits the EQ1 data.

Both EQ1 and EQ2 were well recorded teleseismically by the GDSN and Canadian networks. The long-period teleseismic data show that EQ2 is more complex than EQ1 as did the local and regional strong motion data. The teleseismic records indicate that EQ2 may consist of two subevents similar to EQ1, but with the second subevent larger than the first. Figure 4.5 shows the raw data for EQ1 and EQ2 as well as the 1962 Barringer Mountain event.

depth of 10 km for both.

EQ2 is a more complex event than either EQ1 or EQ3 and consists of two or more subevents. If we line up the strong S motion at PAS for EQ1 and EQ2 (Figure 4.2), we see that EQ2 is preceded by a small foreshock. This foreshock was also identified, but treated as an additional subevent by *Frankel and Wennerberg* [1988, 1989]. Because of the foreshock, EQ2 may not be as well located as EQ1 since the network location reflects the foreshock location and not necessarily the location of the main energy release. Such a difference between the epicenter and area of maximum dislocation was seen in the 1979 Imperial Valley earthquake. Although the earthquake was located 5 km south of the California-Mexico border, the maximum dislocation occurred in two localized areas 7.5 and 25 km north of the epicenter [*Hartzell and Helmberger, 1982*]. In Figure 4.2 it can be seen that EQ2 has smaller surface waves than EQ1 even though EQ1 is a smaller event, indicating that the focal depth of EQ2 is at least as great as that of EQ1 (10.5 km) and possibly greater. Since EQ2 was originally located at a depth of about 2 km [*Magistrale et al., 1989*], this suggests that indeed there is some discrepancy between the network depth and the actual depth of EQ2. In modeling the teleseismic waves of EQ2 (which will be discussed in a later section), we obtain the best results when we use a depth of 10 km or greater.

Both EQ1 and EQ2 were well recorded teleseismically by the GDSN and Canadian networks. The long-period teleseismic data show that EQ2 is more complex than EQ1 as did the local and regional strong motion data. The teleseismic records indicate that EQ2 may consist of two subevents similar to EQ1, but with the second subevent larger than the first. Figure 4.5 shows the raw data for EQ1 and EQ2 as well as the 1968 Borrego Mountain event

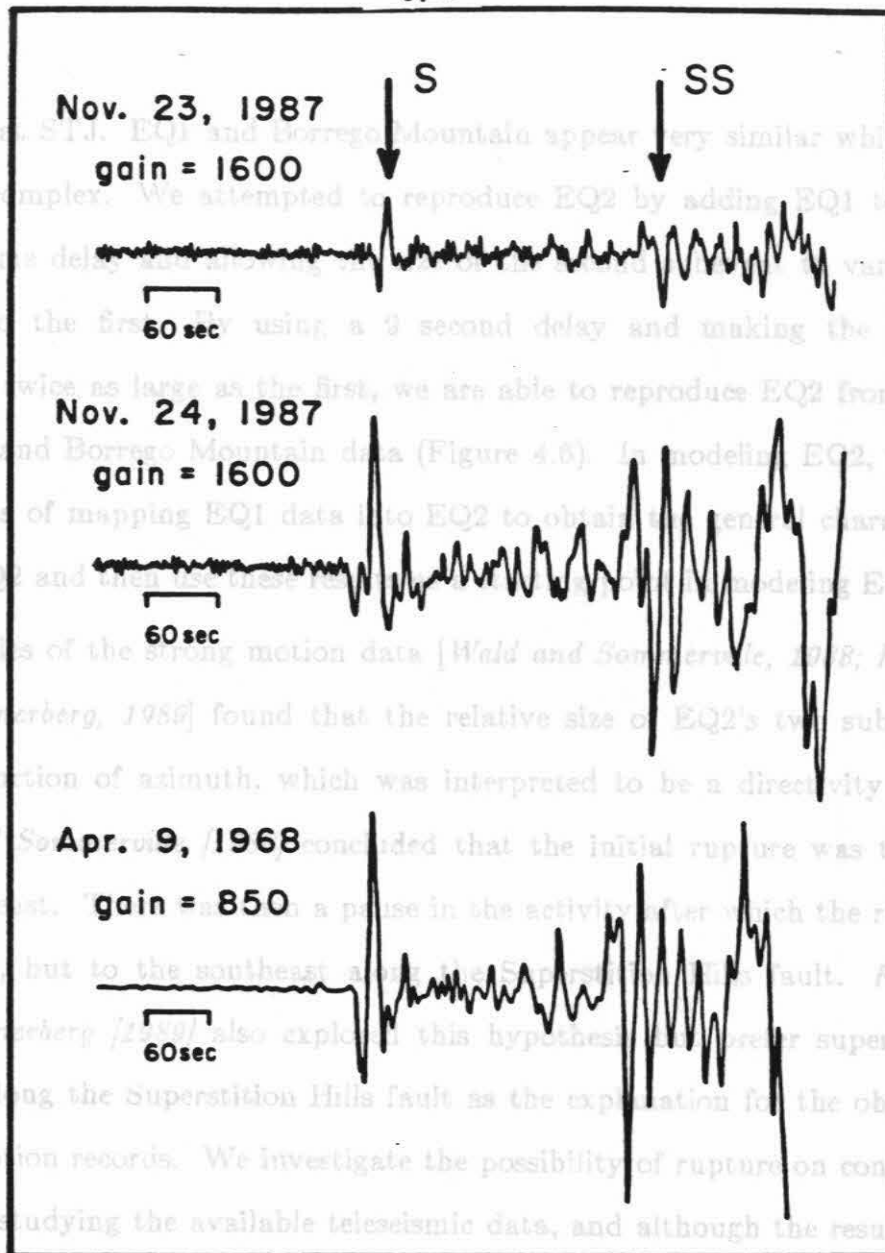


Figure 4.5 the relative timing of the two SH data recorded at STJ for EQ1, EQ2, and the 1968 Borrego Mountain event. The data are plotted at the correct relative amplitudes of the original records. Note that the magnification has changed since 1968.

distribution and known fault geometry, the most reasonable locations for the two subevents separated in this manner would be to place the first subevent on the Elmore Ranch fault (the same fault as EQ1) and the second subevent on the Superstition Hills fault.

recorded at STJ. EQ1 and Borrego Mountain appear very similar while EQ2 is more complex. We attempted to reproduce EQ2 by adding EQ1 to itself with a time delay and allowing the size of the second subevent to vary with respect to the first. By using a 9 second delay and making the second subevent twice as large as the first, we are able to reproduce EQ2 from both the EQ1 and Borrego Mountain data (Figure 4.6). In modeling EQ2, we use the results of mapping EQ1 data into EQ2 to obtain the general characteristics of EQ2 and then use these results as a starting point in modeling EQ2.

Studies of the strong motion data [*Wald and Sommerville, 1988; Frankel and Wennerberg, 1989*] found that the relative size of EQ2's two subevents was a function of azimuth, which was interpreted to be a directivity effect. *Wald and Sommerville [1988]* concluded that the initial rupture was toward the northeast. There was then a pause in the activity after which the rupture continued, but to the southeast along the Superstition Hills fault. *Frankel and Wennerberg [1989]* also explored this hypothesis but prefer super-shear rupture along the Superstition Hills fault as the explanation for the observed strong motion records. We investigate the possibility of rupture on conjugate faults by studying the available teleseismic data, and although the results are inconclusive due to the uncertainties in the relative timing of the two subevents at some stations, our best results indicate that the second subevent occurred due south of the first. In light of the aftershock distribution and known fault geometry, the most reasonable locations for the two subevents separated in this manner would be to place the first subevent on the Elmore Ranch fault (the same fault as EQ1) and the second subevent on the Superstition Hills fault.

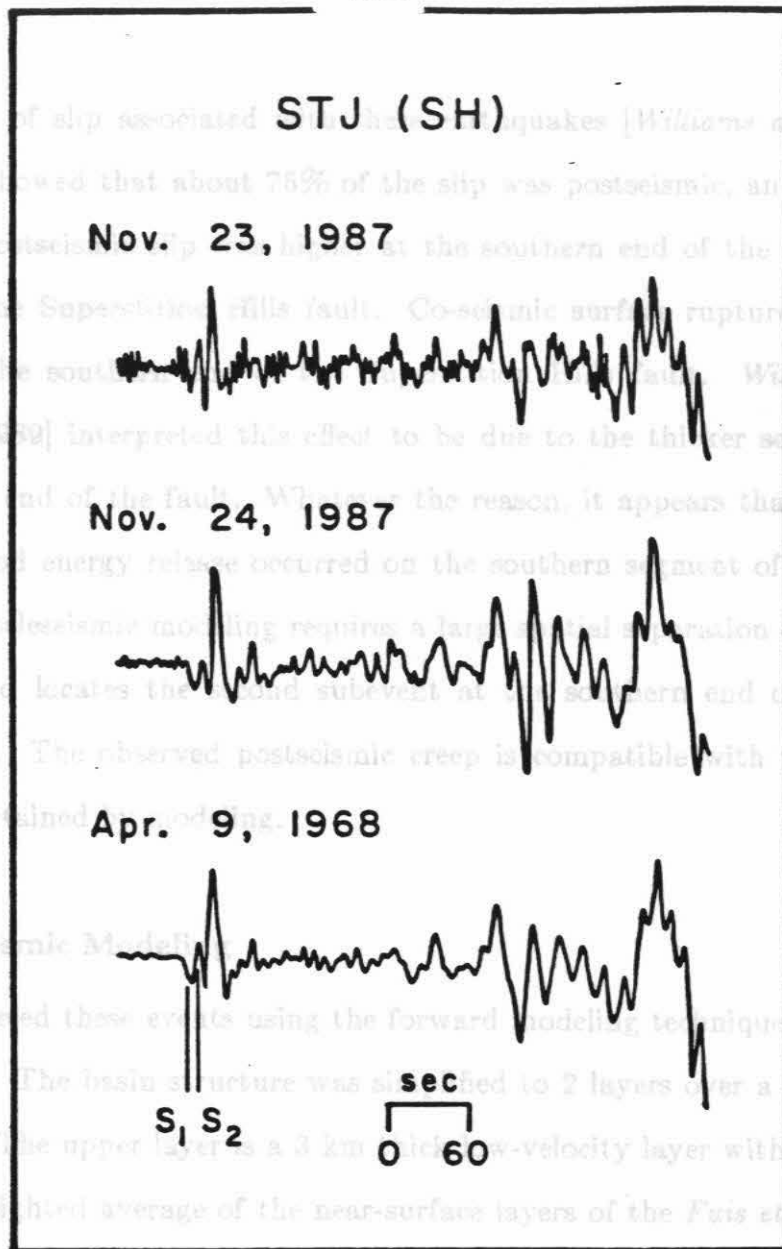


Figure 4.6

The middle trace is the SH data at STJ for EQ2. The upper trace is the data for EQ1 added to itself with a 9 sec delay and with the delayed event being twice as large as the first. The lower trace is the data for the Borrego Mountain event added to itself with a 9 sec delay. Amplitudes are normalized so that the maximum S amplitude is the same on all traces.

For the present the basin edge effects will be ignored, but may be addressed in a subsequent study.

A study of slip associated with these earthquakes [Williams and Magistrale, 1989] showed that about 75% of the slip was postseismic, and that the amount of postseismic slip was higher at the southern end of the aftershock zone along the Superstition Hills fault. Co-seismic surface rupture was also inferred at the southern end of the Superstition Hills fault. Williams and Magistrale [1989] interpreted this effect to be due to the thicker sediment at the southern end of the fault. Whatever the reason, it appears that much of the long-period energy release occurred on the southern segment of the fault. Long-period teleseismic modeling requires a large spatial separation of the two subevents and locates the second subevent at the southern end of the aftershock zone. The observed postseismic creep is compatible with the source separation obtained by modeling.

4.3 Teleseismic Modeling

We modeled these events using the forward modeling technique discussed in chapter 1. The basin structure was simplified to 2 layers over a half-space (Table 4.1). The upper layer is a 3 km thick low-velocity layer with velocities that are a weighted average of the near-surface layers of the Fuis *et al.* [1982] model for the Imperial Valley. The lower layer is a "normal" crustal layer 12 km thick. The half-space has upper mantle velocities. Since these events occurred at the edge of the basin, there is some concern about the adequacy of assuming a laterally homogeneous velocity model [Magistrale *et al.*, 1989]. For the present the basin edge effects will be ignored, but may be addressed in a subsequent study.

The results for EQ1 are shown in Table 4.1. Figures 4.7 and 4.8. We have included one P_{21} (regional) wave. The data coverage is sparse, the number of the data well. At some station Canadian stations improve the fit of this phase. The problem is probably the result of trade-offs in the source time separation, frequency and crustal velocity structure. The digital stations have longer period instruments and are therefore less sensitive to small changes in the duration. When we used a half-space model, the

Table 4.1

Velocity Model

P Wave Velocity (km/sec)	S Wave Velocity (km/sec)	Density (g/cm ³)	Thickness (km)
3.7	1.4	1.6	3
6.2	3.5	2.7	13
7.9	4.6	3.4	

The results for EQ1 are displayed in Figures 4.7 and 4.8. We have included one P_{nl} (regional) waveform to expand the data coverage. In general the synthetics fit the data well. At some eastern Canadian stations however, the initial SH arrival is noticeably larger than the observed first arrival. This occurs only at analog stations. Changing the focal mechanism does not improve the fit of this phase. The problem is probably the result of trade-offs in the source time separation, frequency and crustal velocity structure. The digital stations have longer period instruments and are therefore less sensitive to small changes in the duration. When we used a half-space model, the initial S arrivals were not abnormally large, but the P synthetics did not fit the data so we used a more realistic velocity model. With the basin velocity structure and a longer time function (5 to 6 sec duration instead of 1 to 2 sec), the problem of the first arrival can be partially alleviated, but the overall frequency content of the synthetics does not fit the data. We use a short time function because it produces the observed frequencies at all stations and the observed relative amplitudes at most stations. An exact time function has not been determined because the long-period waves are not sensitive to small changes in the time function, but a triangle of 1 to 2 sec duration produces generally good results.

Figure 4.7

In short, the long-period modeling of EQ1 confirms that it is a simple deep event, at roughly 10 km. The best fitting focal mechanism is a vertical pure strike-slip fault striking at 315° or 45° . Based on the observed surface rupture pattern [Magistrale et al., 1989] the left-lateral or NE-striking plane is probably the fault plane. The moment determined from SH modeling is 2.7×10^{25} dyne cm, which is in good agreement with the P_{nl} moment of 2.9×10^{25} . The teleseismic P waves, however, fit best with a slightly higher

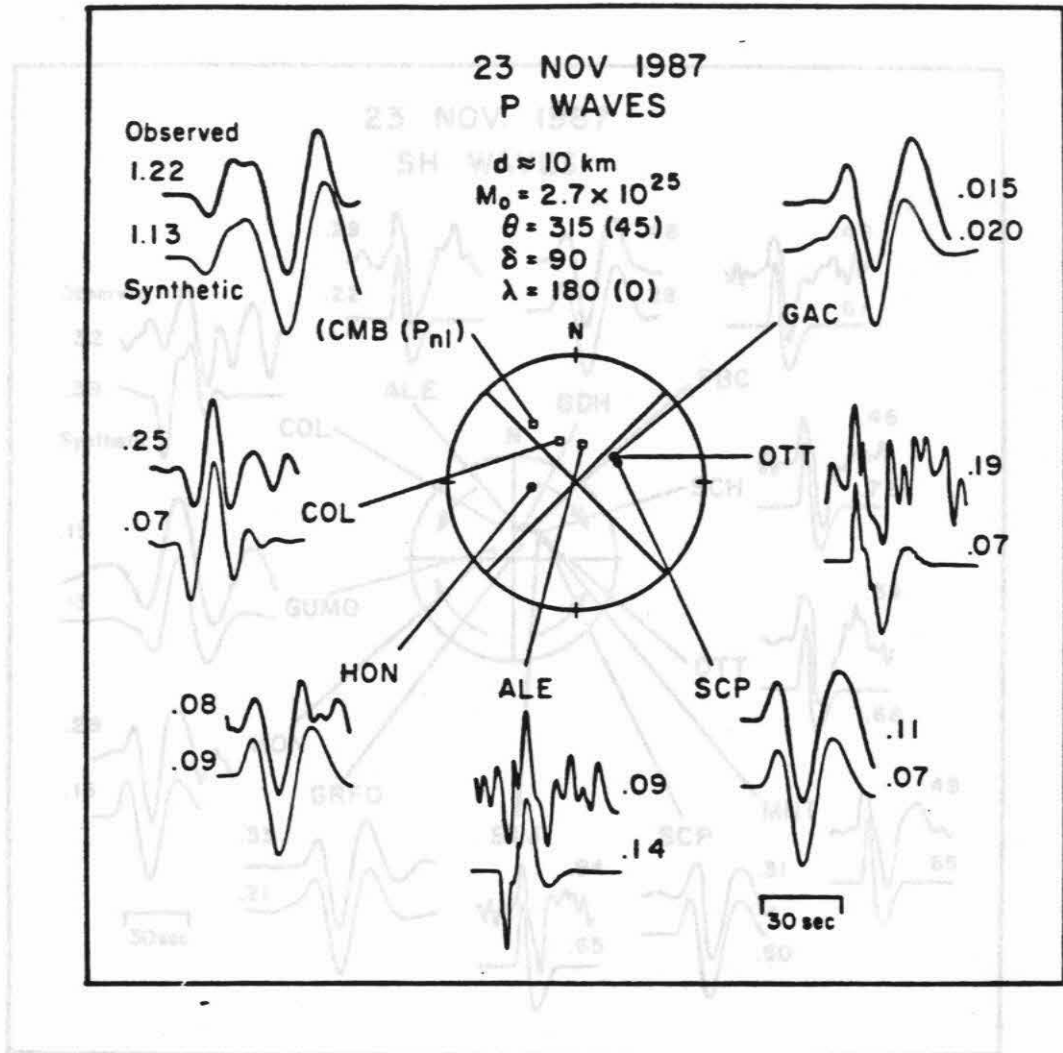


Figure 4.7

P wave data and synthetics for the best-fitting EQ1 solution. The upper trace is the observed waveform; the lower is the synthetic. Amplitudes are given in units of 10^{-3} cm and the instrument gain has been removed from the observed waves.

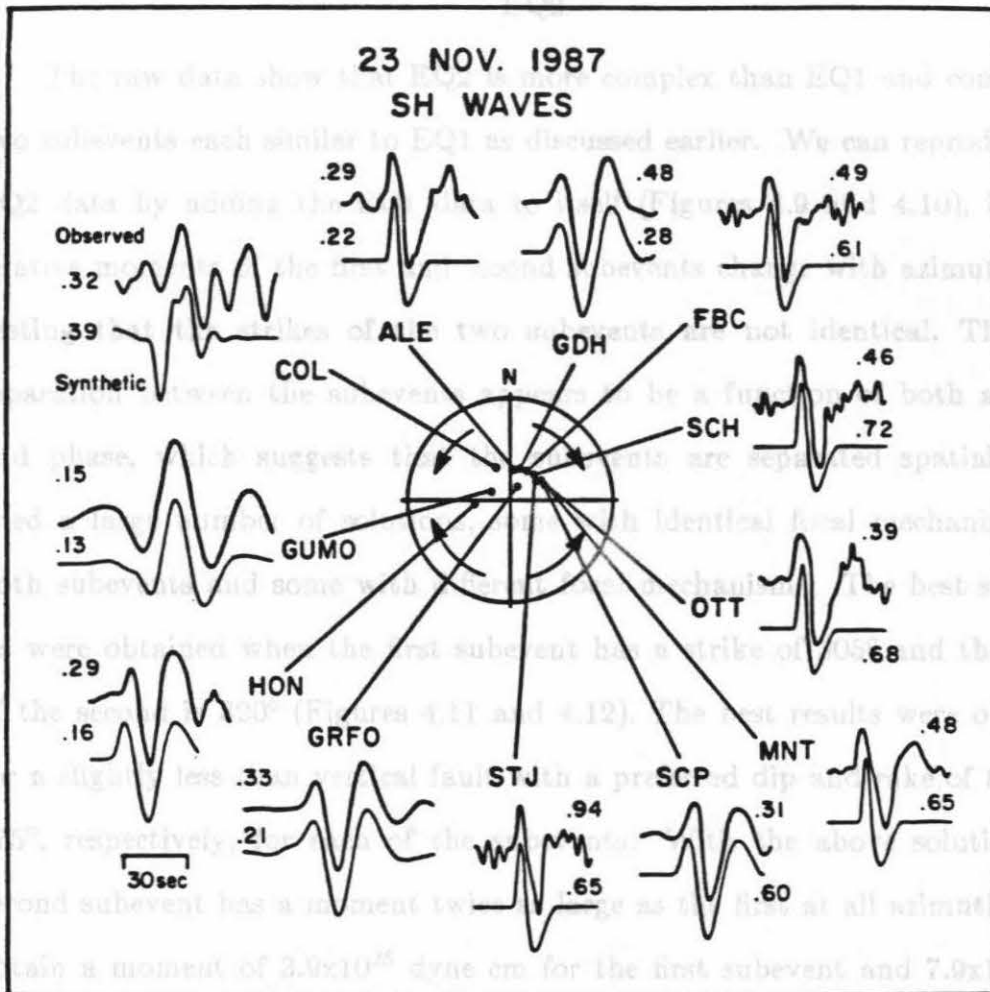


Figure 4.8
SH data and synthetics for EQ2. The format is the same as for Fig. 4.7.

moment (3.3×10^{25}).

EQ2

The raw data show that EQ2 is more complex than EQ1 and consists of two subevents each similar to EQ1 as discussed earlier. We can reproduce the EQ2 data by adding the EQ1 data to itself (Figures 4.9 and 4.10), but the relative moments of the first and second subevents change with azimuth, suggesting that the strikes of the two subevents are not identical. The time separation between the subevents appears to be a function of both azimuth and phase, which suggests that the subevents are separated spatially. We tried a large number of solutions, some with identical focal mechanisms for both subevents and some with different focal mechanisms. The best synthetics were obtained when the first subevent has a strike of 305° and the strike of the second is 320° (Figures 4.11 and 4.12). The best results were obtained for a slightly less than vertical fault with a preferred dip and rake of 80° and 175° , respectively, for each of the subevents. With the above solution, the second subevent has a moment twice as large as the first at all azimuths. We obtain a moment of 3.9×10^{25} dyne cm for the first subevent and 7.9×10^{25} for the second. As was noted in the EQ1 synthetics, the initial SH arrival at some eastern Canadian stations is larger than the observed arrival. Again the amplitude cannot be corrected by changing the focal mechanism or depth. When we calculate the moment of EQ2 by using the synthetically determined moment for EQ1 and comparing the maximum observed amplitudes at all stations which recorded both events, we obtain moments of 3.6×10^{25} and 7.2×10^{25} dyne cm for the two subevents.

By using the differences in P and SH delays for the second subevent at stations of different azimuths, we can obtain the spatial and temporal

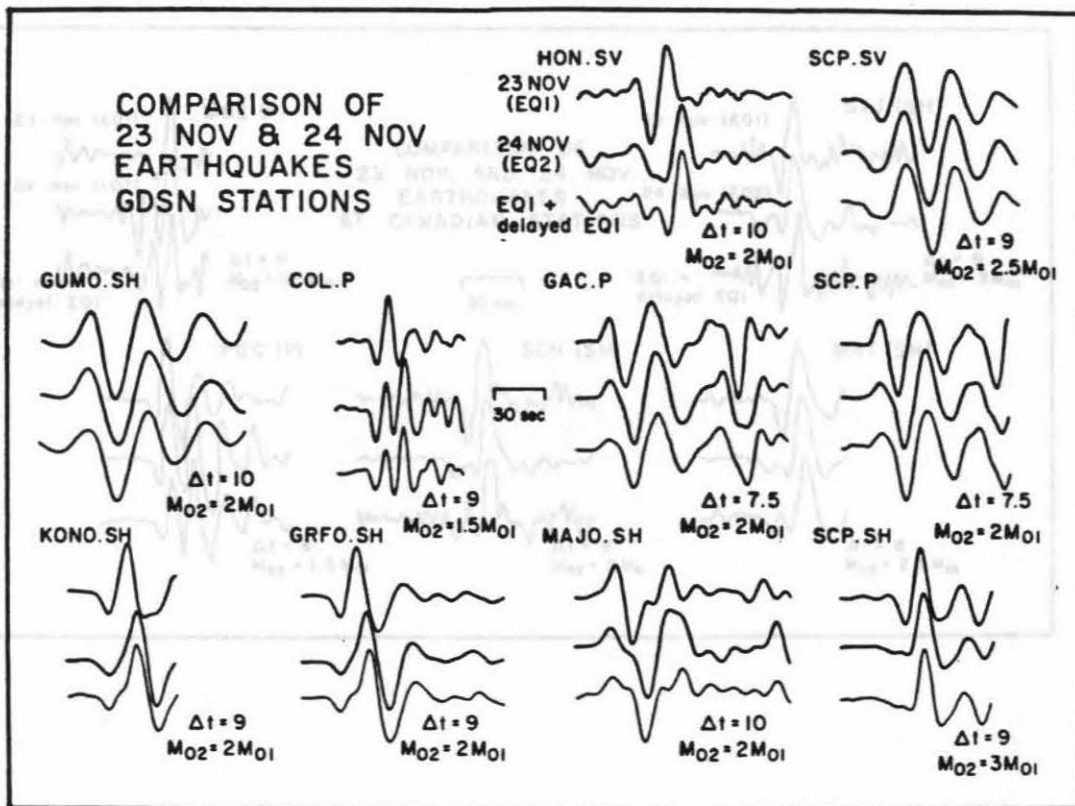


Figure 4.9

The upper trace is EQ1, the middle is EQ2, and the lower is EQ1 added to itself with the delays and relative moments as indicated. Amplitudes are normalized to the maximum peak to peak amplitude. The P data at HON are clipped and therefore not shown.

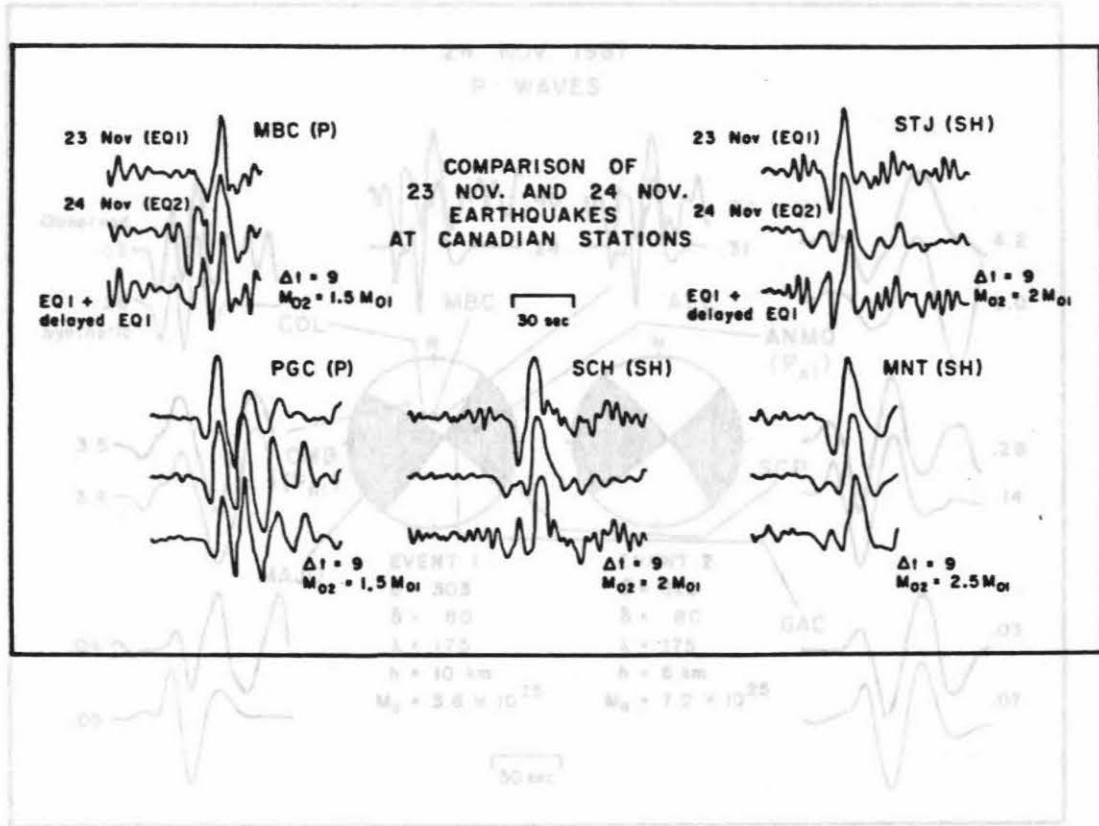


Figure 4.10

Canadian data for EQ1 and EQ2. The format is the same as Fig. 4.9. Stations ANMO and CMB are at regional distances; all other stations are at teleseismic distances. The format is the same as Fig. 4.7.

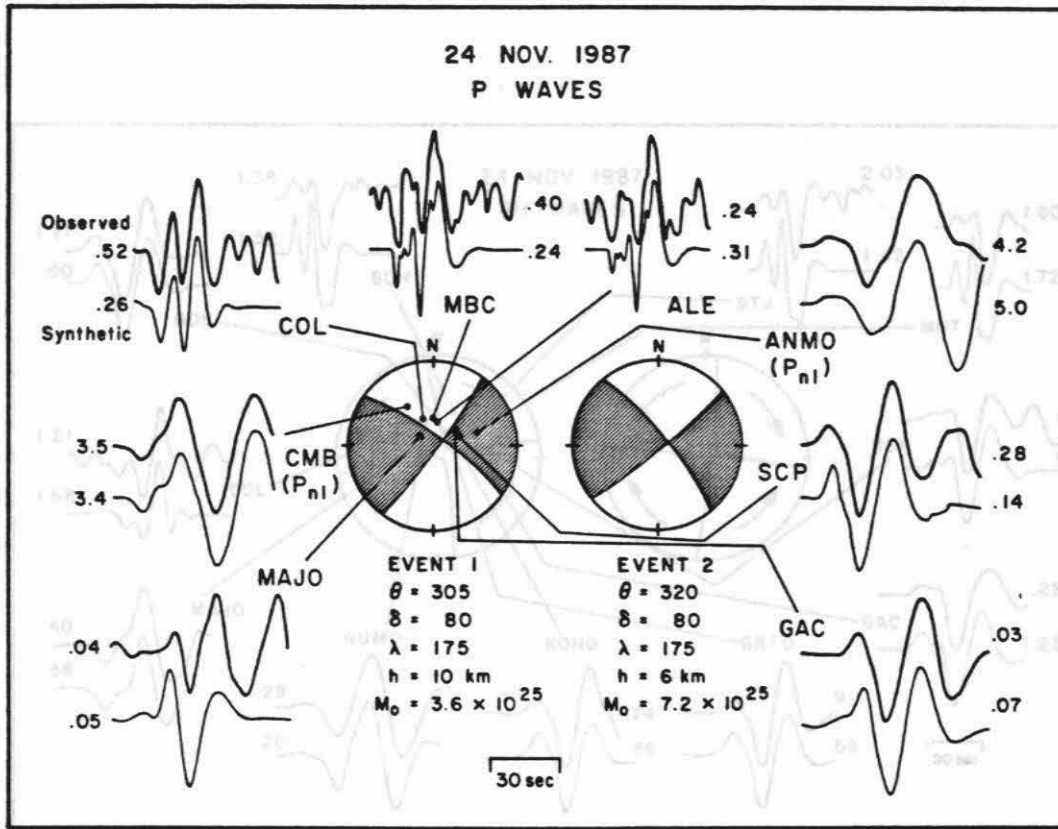


Figure 4.11

P wave data and synthetics for the best fitting EQ2 solution. Stations ANMO and CMB are at regional distances; all other stations are at teleseismic distances. The format is the same as Fig. 4.7.

differences between the two subevents. Since we have good P and SH data at SCP, COL, and MAJO, but only one good record at most other stations, we concentrate on these three stations. At SCP we have a 7.5 sec delay between the P waves of the two subevents and 9 sec between the SH waves. At COL the delays are 9 and 11 sec for P and SH waves, respectively, and at MAJO

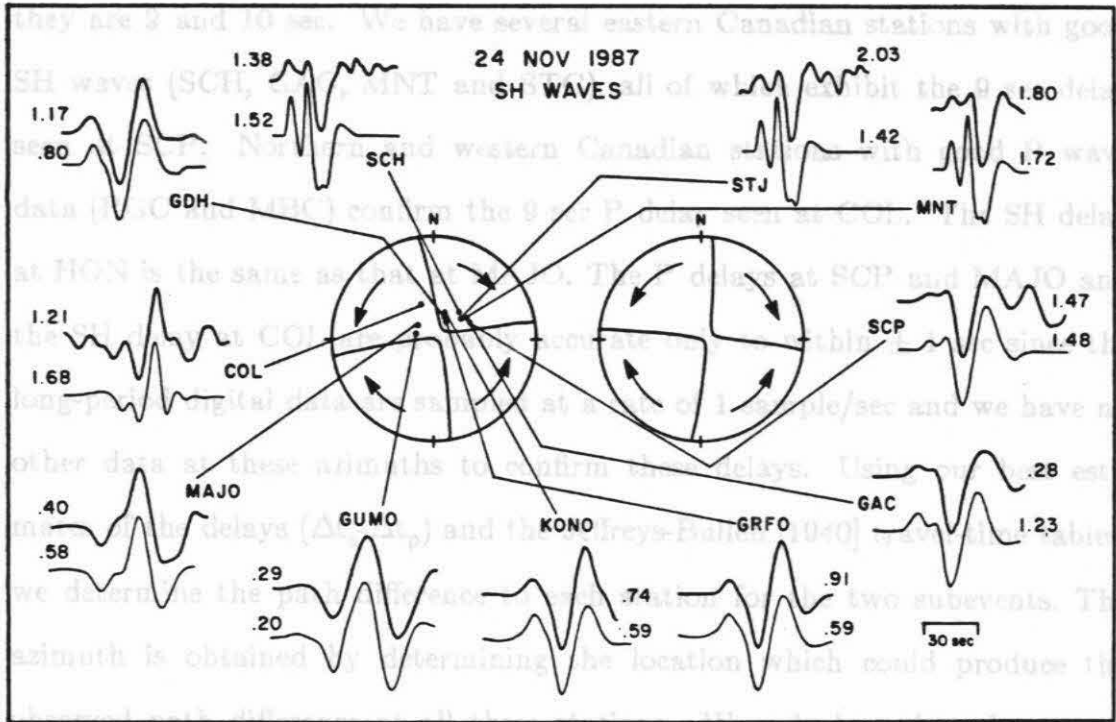


Figure 4.12
SH wave data and synthetics for EQ2. All stations are at teleseismic distances. The format is the same as Fig. 4.7.

varies from 120° to 250° . For the average S-P times we obtain a time separation of 6.5 sec.

We can also consider P and S waves separately, using Δt_p and Δt_s instead of $\Delta t_p - \Delta t_s$, and the equation [Ben-Menahem et al., 1965]

$$\Delta t = T_s - D \cos(\delta_0 - \phi) P,$$

differences between the two subevents. Since we have good P and SH data at SCP, COL, and MAJO, but only one good record at most other stations, we concentrate on these three stations. At SCP we have a 7.5 sec delay between the P waves of the two subevents and 9 sec between the SH waves. At COL the delays are 9 and 11 sec for P and SH waves, respectively, and at MAJO they are 9 and 10 sec. We have several eastern Canadian stations with good SH waves (SCH, GAC, MNT and STG), all of which exhibit the 9 sec delay seen at SCP. Northern and western Canadian stations with good P wave data (PGC and MBC) confirm the 9 sec P delay seen at COL. The SH delay at HON is the same as that at MAJO. The P delays at SCP and MAJO and the SH delay at COL are probably accurate only to within ± 1 sec since the long-period digital data are sampled at a rate of 1 sample/sec and we have no other data at these azimuths to confirm these delays. Using our best estimates of the delays ($\Delta t_s - \Delta t_p$) and the Jeffreys-Bullen [1940] travel-time tables, we determine the path difference to each station for the two subevents. The azimuth is obtained by determining the location which could produce the observed path difference at all three stations. We calculate that the second subevent occurred 30 km almost due south of the first. Using the minimum S-P times at all stations, we obtain a source separation of 8 km with the second subevent SW of the first. A source separation of 50 km is also within the uncertainty of the data, and with a large separation the relative azimuth varies from 125° to 250° . For the average S-P times we obtain a time separation of 6.5 sec.

We can also consider P and S waves separately, using Δt_p and Δt_s instead of $\Delta t_s - \Delta t_p$, and the equation [Ben-Menahem et al., 1965]

$$\Delta t = T_0 - D \cos(\phi_0 - \phi) P,$$

where Δt is the observed time difference between the subevents at a station, T_0 is the actual time difference between the subevents, D is the spatial separation of the subevents, ϕ_0 is the azimuthal separation of the subevents, ϕ is the station azimuth, and P is the ray parameter. The station parameters are summarized in Table 4.2. For SH waves we calculate $D=30.5$ km, $\phi_0=177^\circ$, and $T_0=7.6$ sec. For P waves we obtain $D=16.2$ km, $\phi_0=143.5^\circ$, and $T_0=7.7$ sec. If we include the uncertainty in Δt at some station, we obtain a source separation uncertainty similar to that described for the first method.

The local strong motion data [Wald and Somerville, 1988; Frankel and Wennerberg, 1988, 1989] and the size of the aftershock zone (Figure 4.1) are more compatible with a small source separation, but since some of the coseismic slip and most of the postseismic slip has occurred at the southern end of the aftershock zone, a 30 km source separation may not be unreasonable. The apparent discrepancy in source separation may be due to different frequencies of seismic energy being preferentially produced on different segments of the fault. The high-frequency strong motion energy may be produced by a small high stress drop segment at the northern end of the fault, while the longer period energy can be produced by both high and low stress drop segments.

Differences in the relative amplitudes of the two subevents at local strong motion stations have been used to infer that the first subevent occurred on the NE-striking plane [Wald and Somerville, *personal communication*]. We tested this hypothesis at teleseismic distances. The 30 km north-south source separation determined from $\Delta t_s - \Delta t_p$ and Δt_s is compatible with the two subevents occurring on conjugate fault planes, but given the large uncertainty in the source separation, conjugate faults are not required. The source

separation determined from Δt_p (Table 4.2) or hand, is compatible with both subevents occurring on the same fault and with the Frankel and

Station	Δt_p (sec)	Δt_s (sec)	ϕ (deg)
SCP	7.5 ± 1	9.0	64.5
COL	9.0	11.0 ± 1	338.2
MAJO	9.0 ± 1	10.0	308.7

from subevent 1 had a source time separation equal to what was observed at each station. By interpolation and extrapolation, the delays were determined for subevents at 5 km intervals to a maximum distance of 50 km. The results at most stations were not significantly different from the point source solution, suggesting that whether subevent 2 is point source or a continuous rupture cannot be resolved teleseismically, at least at long periods.

4.4 Discussion and Conclusions

As was noted earlier, EQ1 and EQ3 are very similar at PAS, while EQ2 is a more complex event. We attempted to reproduce EQ2 by adding EQ1 and EQ3 to themselves (Figure 4.13) with a time delay, in the same manner we reproduced EQ1 from the EQ1 and Borrego Mountain data teleseismically. Since the frequency content of EQ2 is higher than EQ1, we attempted to equalize the frequencies by convolving all seismograms with a long-period Wood-Anderson instrument as displayed in Figure 4.2. Delays from 5 to 10 sec in intervals of 0.5 sec were tested. The best time separation is 8 sec, although 7.5 and 8.5 sec produce many features that match EQ2. EQ2 is

separation determined from Δt_p on the other hand, is compatible with both subevents occurring on the Superstition Hills fault and with the *Frankel and Wennerberg* [1989] interpretation of the strong motion data. To determine whether the second subevent was a point source or a continuous southward rupture, we distributed the second subevent into a number of smaller but identical subevents with a total moment the same as the point source moment for the second subevent. The relative timing of these smaller events was such that an event located at the same place as the first subevent had a delay equal to the absolute source time separation (7 ± 0.5 sec) and an event 30 km from subevent 1 had a source time separation equal to what was observed at each station. By interpolation and extrapolation, the delays were determined for subevents at 5 km intervals to a maximum distance of 50 km. The results at most stations were not significantly different from the point source solution, suggesting that whether subevent 2 is point source or a continuous rupture cannot be resolved teleseismically, at least at long periods.

4.4 Discussion and Conclusions

As was noted earlier, EQ1 and EQ3 are very similar at PAS, while EQ2 is a more complex event. We attempted to reproduce EQ2 by adding EQ1 and EQ3 to themselves (Figure 4.13) with a time delay, in the same manner we reproduced EQ1 from the EQ1 and Borrego Mountain data teleseismically. Since the frequency content of EQ2 is higher than EQ1, we attempted to equalize the frequencies by convolving all seismograms with a long-period Wood-Anderson instrument as displayed in Figure 4.2. Delays from 6 to 10 sec in intervals of 0.5 sec were tested. The best time separation is 8 sec, although 7.5 and 8.5 sec produce many features that match EQ2. EQ2 is

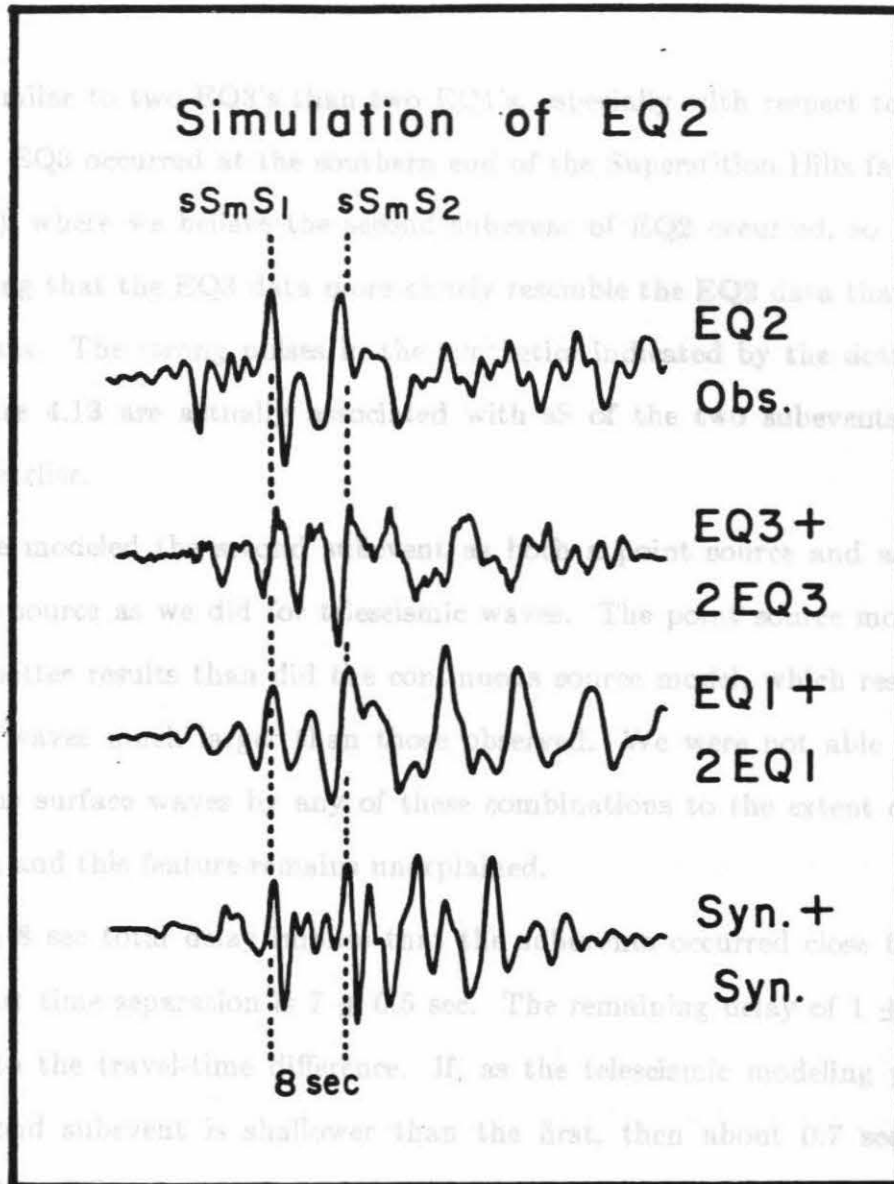


Figure 4.13 Attempts to reproduce EQ2 by adding the tangential components of various events together. In all cases an 8 sec delay is used and the second subevent is scaled to be twice as large as the first. The uppermost waveform is EQ2 at PAS; the second is the aftershock EQ3 added to itself; the third is EQ1 added to itself; the fourth is the synthetic for EQ3 added to itself.

In summary, we have modeled the Superstition Hills earthquakes both synthetically and by mapping the data of one event into that of the other. EQ1 was a simple pure strike-slip earthquake on a vertical plane striking 45°

more similar to two EQ3's than two EQ1's, especially with respect to surface waves. EQ3 occurred at the southern end of the Superstition Hills fault (Figure 4.1), where we believe the second subevent of EQ2 occurred, so it is not surprising that the EQ3 data more closely resemble the EQ2 data than do the EQ1 data. The strong pulses in the synthetics indicated by the dotted lines in Figure 4.13 are actually associated with sS of the two subevents as discussed earlier.

We modeled the second subevent as both a point source and as a continuous source as we did for teleseismic waves. The point source model produced better results than did the continuous source model, which resulted in surface waves much larger than those observed. We were not able to eliminate the surface waves by any of these combinations to the extent observed in EQ2, and this feature remains unexplained.

An 8 sec total delay implies that the subevents occurred close together. The start time separation is 7 ± 0.5 sec. The remaining delay of 1 ± 0.5 sec is due to the travel-time difference. If, as the teleseismic modeling predicts, the second subevent is shallower than the first, then about 0.7 sec of the travel-time difference is taken up by the depth difference and the remainder is due to the horizontal separation of the two subevents. Because PAS is relatively close to the epicenter, the observed record contains only crustal phases. The observed travel-time difference indicates that the source separation is of the order of a few kilometers. Even if we put both subevents at the same depth, we obtain a small source separation.

In summary, we have modeled the Superstition Hills earthquakes both synthetically and by mapping the data of one event into that of the other. EQ1 was a simple pure strike-slip earthquake on a vertical plane striking 45°

and exhibiting left-lateral surface rupture. It was a relatively deep event occurring at a depth of 10 km with a teleseismic long-period moment of 2.7×10^{25} dyne cm. EQ2 was a more complex event consisting of (to a first approximation) two subevents similar to EQ1, neglecting the small foreshock. The first subevent occurred at a depth of 10 km and had the following mechanism: $\theta=35^\circ$, $\delta=80^\circ$, and $\lambda=175^\circ$. Its teleseismic moment is 3.6×10^{25} . The second subevent occurred 7 ± 0.5 sec later at a depth of at least 6 km and probably deeper. It had a strike of 320° and the same dip and rake as subevent 1, and a moment of 7.2×10^{25} . The teleseismic data indicate that subevent 2 occurred 30 km south of subevent 1. The strong motion data, however, are more compatible with a source separation of only a few kilometers. The uncertainty in the source time separation (± 1 sec) at teleseismic distances results in a large uncertainty in the spatial separation (± 20 km), so there may not be a conflict between the teleseismic and strong motion results. Alternatively, the high-frequency strong motion energy and the long-period energy may have been preferentially produced by different fault segments; that is, the high-frequency component is determined by asperities and lower stress drop regions produce the long-period teleseismic results.

the local records are often off scale. The use of teleseismic data can improve the azimuthal coverage and eliminate the problem of off-scale records. By comparing waveforms and travel times of historic earthquakes with those of recent well-studied (and presumably well-located) events, we are able to obtain information about the size and location of the historic events. We consider historic events to be those which occurred before the installation of the WWSSN network in the early 1960's and recent events to be post-WWSSN events. We use regional and teleseismic records from continuously operating

Chapter 5

Historic Earthquakes in the San Jacinto Fault Zone

5.1 Introduction

The San Jacinto fault zone of the western Imperial Valley is one of the most seismically active regions of southern California. The region is cut by a number of active faults including the San Jacinto, Coyote Creek, Superstition Hills, and Superstition Mountain faults (Figure 5.1). The dominant trend is right-lateral strike-slip faulting on near vertical northwest-striking faults, although left-lateral faulting on conjugate faults has also been noted. Since many of these faults are closely spaced, it may be difficult to determine on which fault an earthquake occurred if the epicentral location is not well constrained. Because assumptions of future seismic activity are based primarily on our knowledge of past behavior, it is important to have accurate locations and moment estimates for past events. For historic events in the Imperial Valley, the azimuthal coverage of local stations is not good. Phases from this region, particularly S, are difficult to pick precisely, and for larger earthquakes the local records are often off scale. The use of teleseismic data can improve the azimuthal coverage and eliminate the problem of off-scale records. By comparing waveforms and travel times of historic earthquakes with those of recent well-studied (and presumably well-located) events, we are able to obtain information about the size and location of the historic events. We consider historic events to be those which occurred before the installation of the WWSSN network in the early 1960's and recent events to be post-WWSSN events. We use regional and teleseismic records from continuously operating

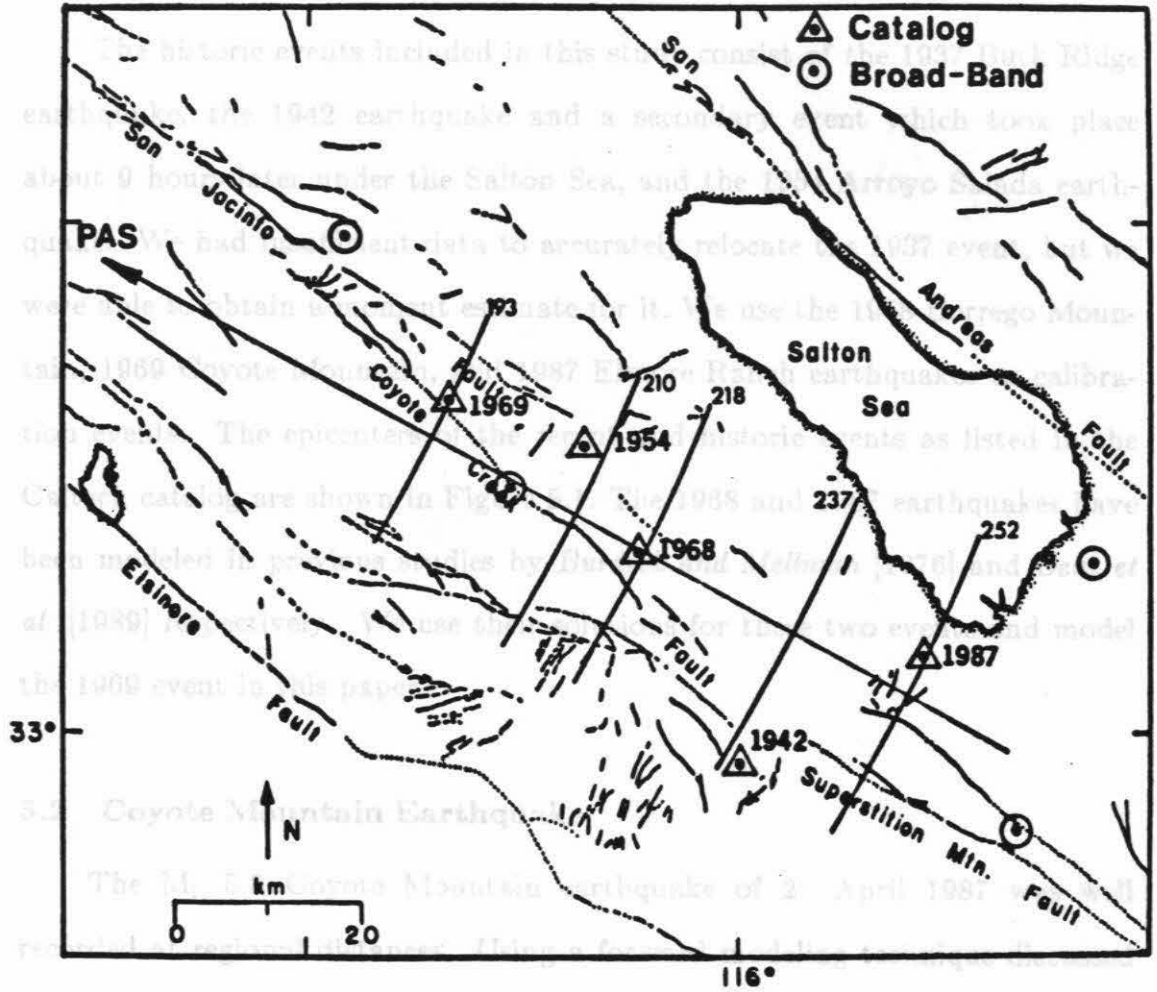


Figure 5.1 Map of the western Imperial Valley showing the major faults and earthquake epicenters. The parallel lines show distance to Pasadena in km. The triangles represent the Caltech catalog locations of the large earthquakes used in this study. The circles represent small earthquakes recorded by the PAS streikeisen used to calibrate travel times to PAS.

Thatcher and Hamilton [1973] obtained using teleseismic first motion data. Our moment estimate is similar to but slightly smaller than their estimate of 5.3×10^{24} . At teleseismic distances this event was recorded, but the direct P arrival is almost always within the noise level, making it difficult to model.

stations, with Pasadena, De Bilt, Ottawa, and St. Louis recording most of the events studied.

The historic events included in this study consist of the 1937 Buck Ridge earthquake, the 1942 earthquake and a secondary event which took place about 9 hours later under the Salton Sea, and the 1954 Arroyo Salada earthquake. We had insufficient data to accurately relocate the 1937 event, but we were able to obtain a moment estimate for it. We use the 1968 Borrego Mountain, 1969 Coyote Mountain, and 1987 Elmore Ranch earthquakes as calibration events. The epicenters of the recent and historic events as listed in the Caltech catalog are shown in Figure 5.1. The 1968 and 1987 earthquakes have been modeled in previous studies by *Burdick and Mellman* [1976] and *Bent et al.* [1989] respectively. We use their solutions for these two events and model the 1969 event in this paper.

5.2 Coyote Mountain Earthquake

The M_L 5.8 Coyote Mountain earthquake of 28 April 1987 was well recorded at regional distances. Using a forward modeling technique discussed in detail by *Helmberger and Engen* [1980] we obtain the fault parameters, depth and seismic moment for this event. By modeling the P_{nl} waveforms (Figure 5.2) we obtain a strike of 305° , a dip of 80° , a rake of 180° , and a seismic moment of 4.8×10^{24} dyne cm. The focal mechanism is consistent with that of other events the region, and is rotated 15° westward from the strike *Thatcher and Hamilton* [1973] obtained using teleseismic first motion data. Our moment estimate is similar to but slightly smaller than their estimate of 5.3×10^{24} . At teleseismic distances this event was recorded, but the direct P arrival is almost always within the noise level, making it difficult to model,

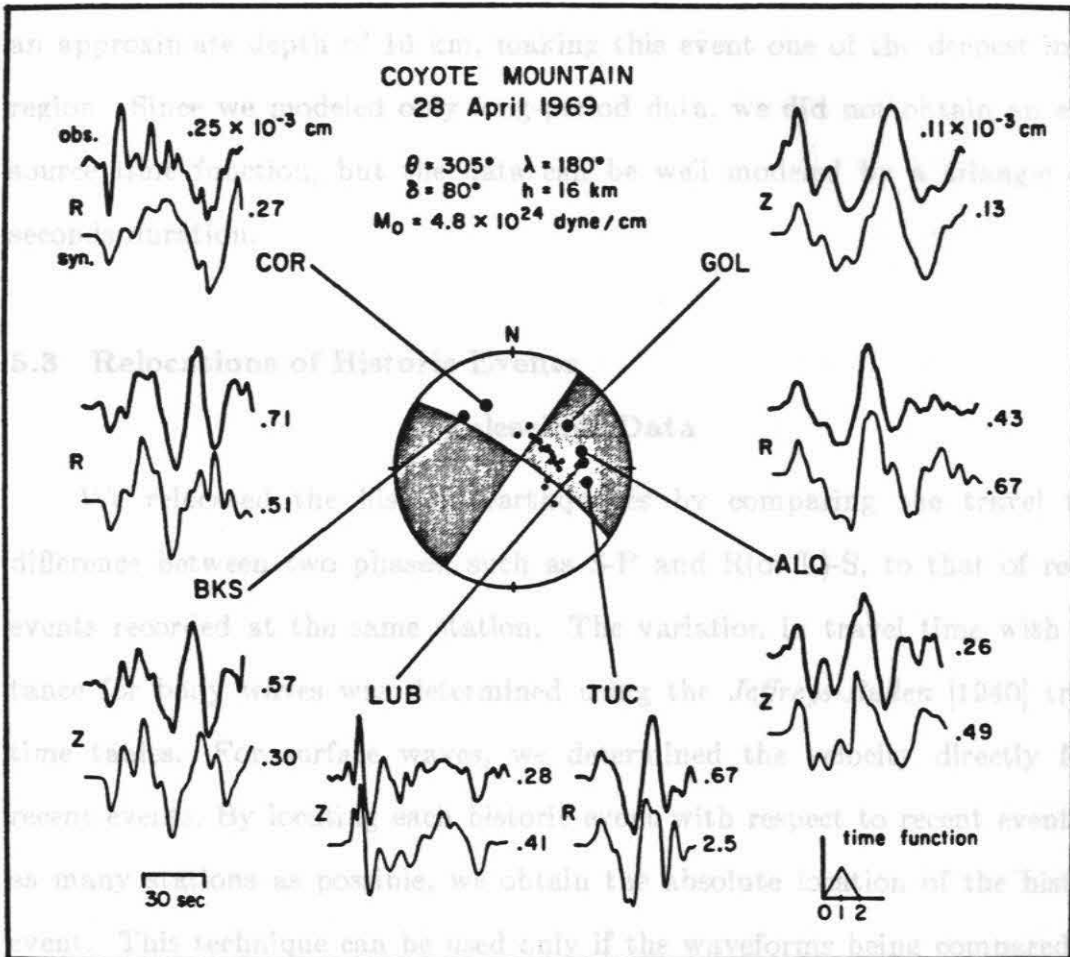


Figure 5.2

Observed (upper) and synthetic (lower) waveforms of the Coyote Mountain earthquake at regional distances. The large dots on the focal mechanism represent the regional stations modeled and the small dots are teleseismic stations. The amplitudes are given in units of 10^{-3} cm and have been corrected for the instrument magnification.

but the reflected phases (pP and sP) can be well modeled, both in waveform and amplitude, by our regional solution. Using the teleseismic data we obtain an approximate depth of 16 km, making this event one of the deepest in the region. Since we modeled only long-period data, we did not obtain an exact source time function, but the data can be well modeled by a triangle of 2 seconds duration.

5.3 Relocations of Historic Events

Teleseismic Data

We relocated the historic earthquakes by comparing the travel time difference between two phases, such as S-P and R(or L)-S, to that of recent events recorded at the same station. The variation in travel time with distance for body waves was determined using the *Jeffreys-Bullen* [1940] travel time tables. For surface waves, we determined the velocity directly from recent events. By locating each historic event with respect to recent events at as many stations as possible, we obtain the absolute location of the historic event. This technique can be used only if the waveforms being compared are very similar to ensure that we are aligning the same phases. Some judgement in the aligning of phases is involved as the waveforms, while similar, are not identical from one event to another. Some of the uncertainty can be removed by filtering the records to equalize the frequency content. Introducing some redundancy into the measurements also helps. For example, we can align the P-waves and measure the S-wave offset and then align the S-waves and measure the P-wave offset. Our overall uncertainty in timing is less than 1 sec for long-period records.

To test the resolution of this method, we relocated the 1987 event with respect to the 1968 earthquake. Figure 5.3 shows the tangential component of these two events recorded at STJ. Depending upon how we align the records, the SS-S times give us a source separation of 15-20 km. The source separation according to the short-period catalog locations is 22 km. Our uncertainty at worst is about 10 km for a single station relocation. As the number of stations increases, the uncertainty decreases.

1954. Both *Richter* [1958] and *Sanders et al.* [1986] locate the 1954 earthquake at the southern end of the San Jacinto fault. *Hanks et al.* [1975] place the event about 14 km northeast of the other locations. Both the 1954 and 1969 earthquakes were well recorded at SLM. If we line up the SV waves (Figure 5.4), we find that the Rayleigh waves are offset by 4 sec, implying that the 1954 event occurred 26 km west of the 1969 earthquake. If we align the Rayleigh waves and filter the 1969 event with a triangle of 4 sec duration to equalize the frequency content (Figure 5.4b), we obtain the same result. This location places the 1954 event much further to the west than expected. Part of the travel time difference between the two events may be due to differences in depth rather than epicenter locations. The Coyote Mountain earthquake is quite deep with a hypocenter at 16-18 km, while the depth of the Arroyo Salada earthquake is in the 6 to 10 km range. When the depth difference is considered most of the travel time difference disappears and the events are located the same distance (within 5 km) from St. Louis. This would still place the 1954 event west of previous locations. Studies of other earthquakes in the Imperial Valley have shown that the bulk of the long-period energy does not necessarily come from the point of the initiation of rupture as determined from short-period data. The 1979 Imperial Valley earthquake was

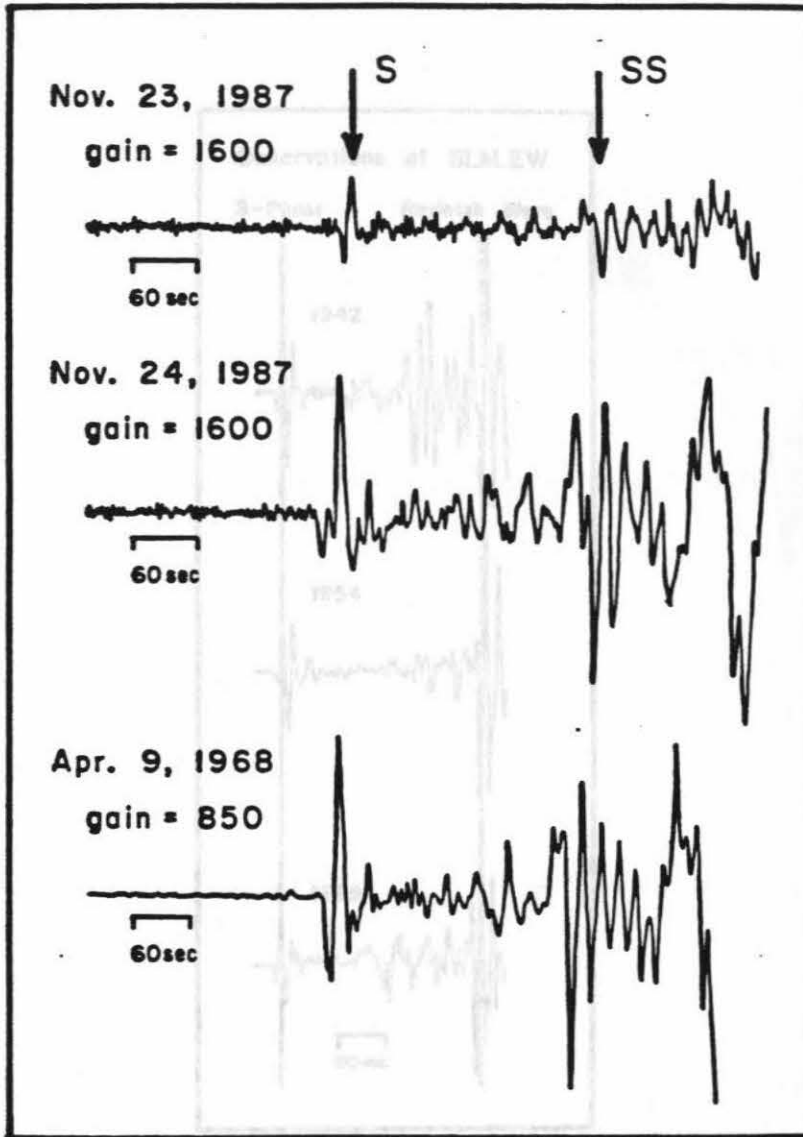


Figure 5.3

Tangential component of the 1987 and 1968 earthquakes recorded at STJ. The spatial separation of these events with respect to STJ is determined from the difference in the SS-S times (from *Bent et al., 1989*).

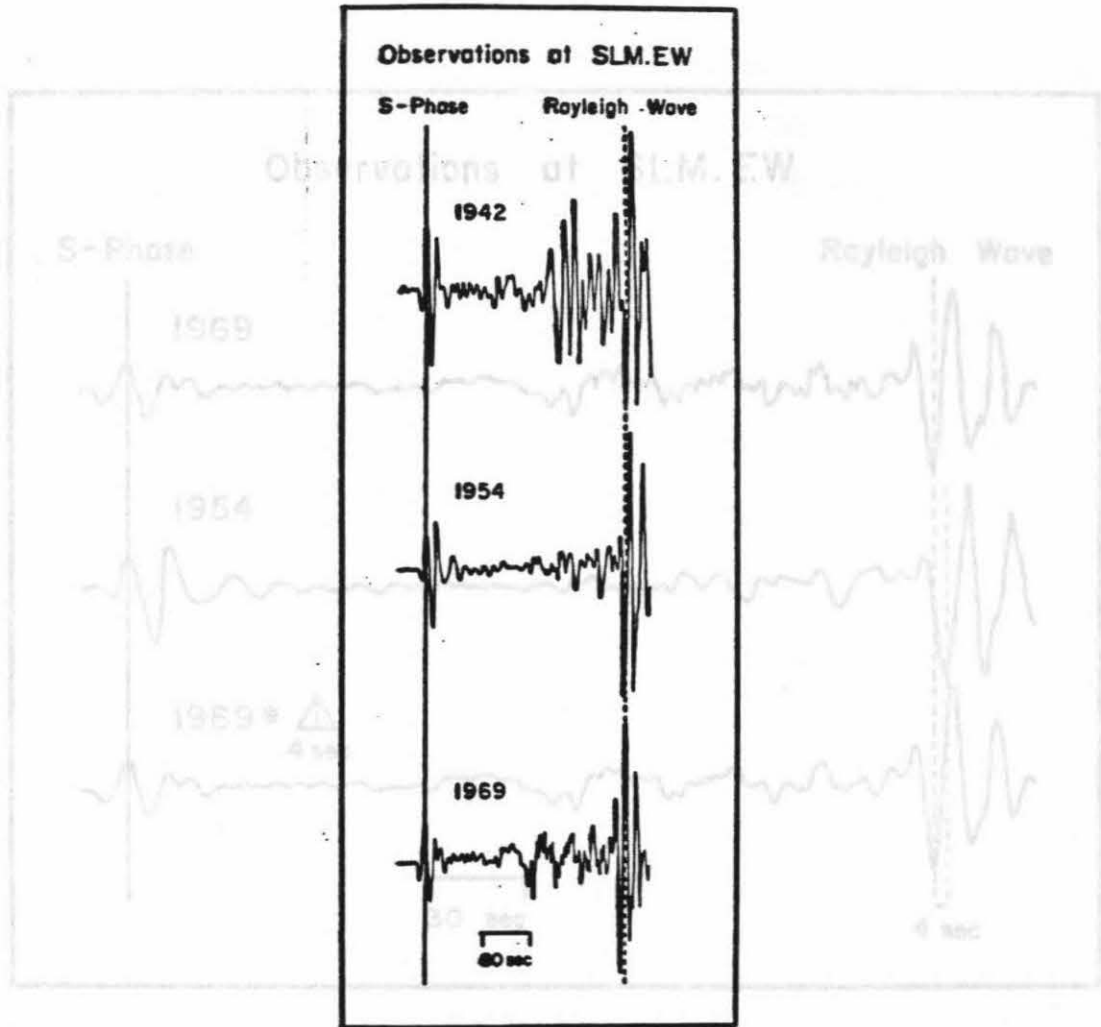


Figure 5.4a

EW (radial) component of S and R waves for the 1942, 1954 and 1969 earthquakes recorded at SLM. The difference in timing between the solid and dashed lines was used to determine the difference in distance from SLM.

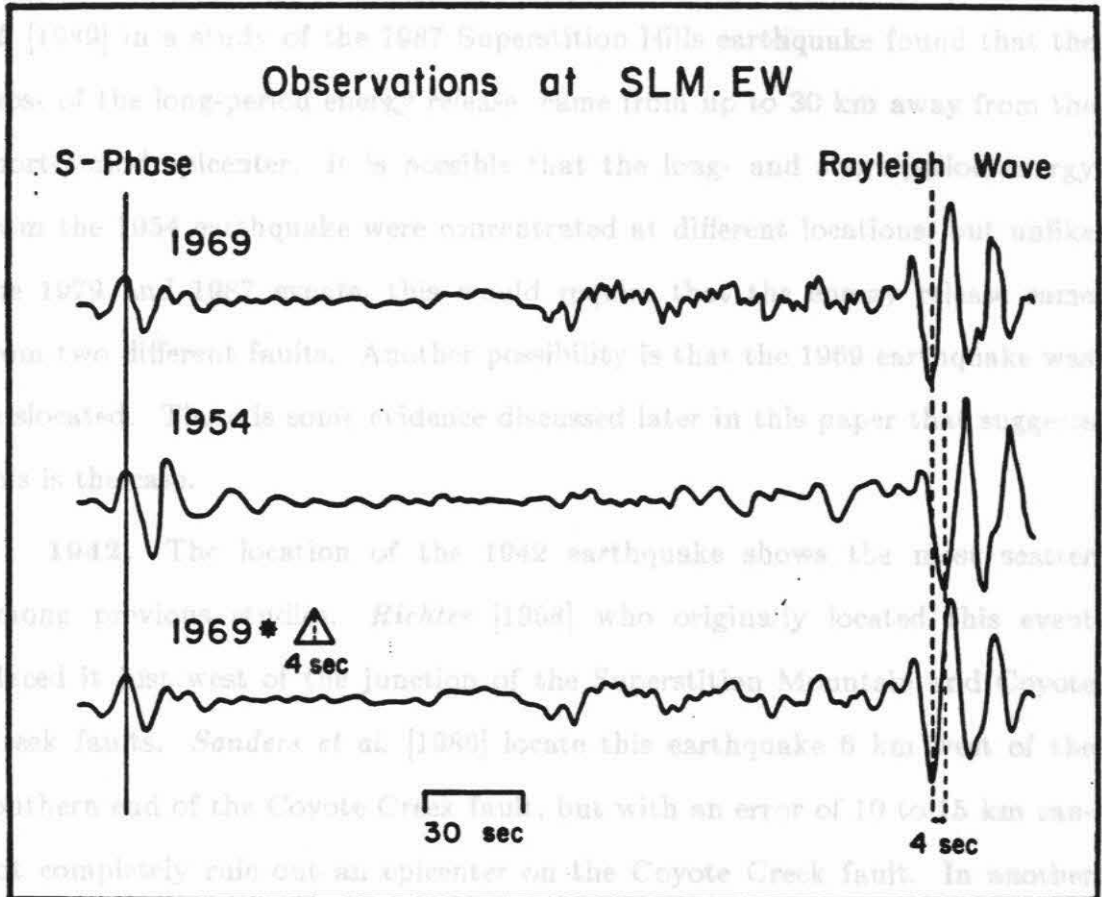


Figure 5.4b

The 1969 and 1954 events at SLM plotted at a larger scale. In the bottom trace the 1969 record has been convolved with a 4 sec triangle to equalize the frequency content of the surface waves of the two events.

The 1942 event was well recorded teleseismically. The 1942 and 1969 events have similar waveforms at SLM (Figure 5.4). Using the R-S times we locate the 1942 event 75 km further away from St. Louis than the Coyote Mountain event. Comparing the 1942 and 1954 events also at St. Louis we obtain a source separation of 18 km along the R-S time (Figure 5.4) and 8 km

located just south of the international border, but a detailed study of the long-period body waves showed that most of the long-period energy came from a location 25 km further north [Hartzell and Helmberger, 1982]. Bent et al. [1989] in a study of the 1987 Superstition Hills earthquake found that the most of the long-period energy release came from up to 30 km away from the short-period epicenter. It is possible that the long- and short-period energy from the 1954 earthquake were concentrated at different locations, but unlike the 1979 and 1987 events, this would require that the energy release came from two different faults. Another possibility is that the 1969 earthquake was mislocated. There is some evidence discussed later in this paper that suggests this is the case. *the Coyote Creek fault.*

1942. The location of the 1942 earthquake shows the most scatter among previous studies. Richter [1958] who originally located this event placed it just west of the junction of the Superstition Mountain and Coyote Creek faults. Sanders et al. [1986] locate this earthquake 6 km west of the southern end of the Coyote Creek fault, but with an error of 10 to 15 km cannot completely rule out an epicenter on the Coyote Creek fault. In another study, Doser and Kanamori [1986] relocated the 1942 earthquake a few km east of the junction of the Superstition Mountain and Coyote Creek faults with error estimates of 10 km. When the error bars are taken into account, all of these epicenters overlap. *moderate to large earthquakes occurred within in*

the The 1942 event was well recorded teleseismically. The 1942 and 1969 events have similar waveforms at SLM (Figure 5.4). Using the R-S times we locate the 1942 event 25 km further away from St. Louis than the Coyote Mountain event. Comparing the 1942 and 1954 events also at St. Louis we obtain a source separation of 16 km using the R-S time (Figure 5.4) and 8 km

using the S-P time (Figure 5.5), with the 1942 event being further from the station in both cases. Comparing the 1942 and 1987 events at OTT (Figure 5.6) we locate the 1942 earthquake 19 km further away than the 1987 event. In this case, there is some difficulty in accurately aligning the phases since the 1942 earthquake was recorded on a low gain instrument and the S-wave is only slightly above the noise level. If we assume that the 1969 event is correctly located there is very little overlap of the locations determined from the individual stations (Figure 5.7a). However, if we use the catalog location for the 1954 event instead, and combine it with the 1987-1942 results, the locations coincide (Figure 5.7b). These results place the 1942 event on or slightly west of the Coyote Creek fault.

1942b. The 1942 earthquake was followed 9 hours later by a secondary event which we will refer to as 1942b. Both were well recorded at FLO (Figure 5.8). Both the S-P and R-S times locate 1942b 51-52 km closer to St. Louis than the 1942 event. Assuming our preferred location for the 1942 event, the 1942b earthquake would be located a few km east of the Salton Sea, and possibly but not necessarily on the San Andreas fault. The original location of the 1942b event beneath the Salton Sea is within the error bars of our location.

Figure 5.5

EW The 1942 sequence of earthquakes was similar to the 1987 Superstition Hills sequence in that two moderate to large earthquakes occurred within in twelve hours of each other and not on the same fault. The aftershock zones of the 1987 earthquakes imply that the two events occurred on conjugate faults [Magistrale et al., 1989]. The similar source separations for the 1942 events raises the possibility that they also occurred on conjugate faults. Unfortunately the aftershock locations do not provide the answer. The

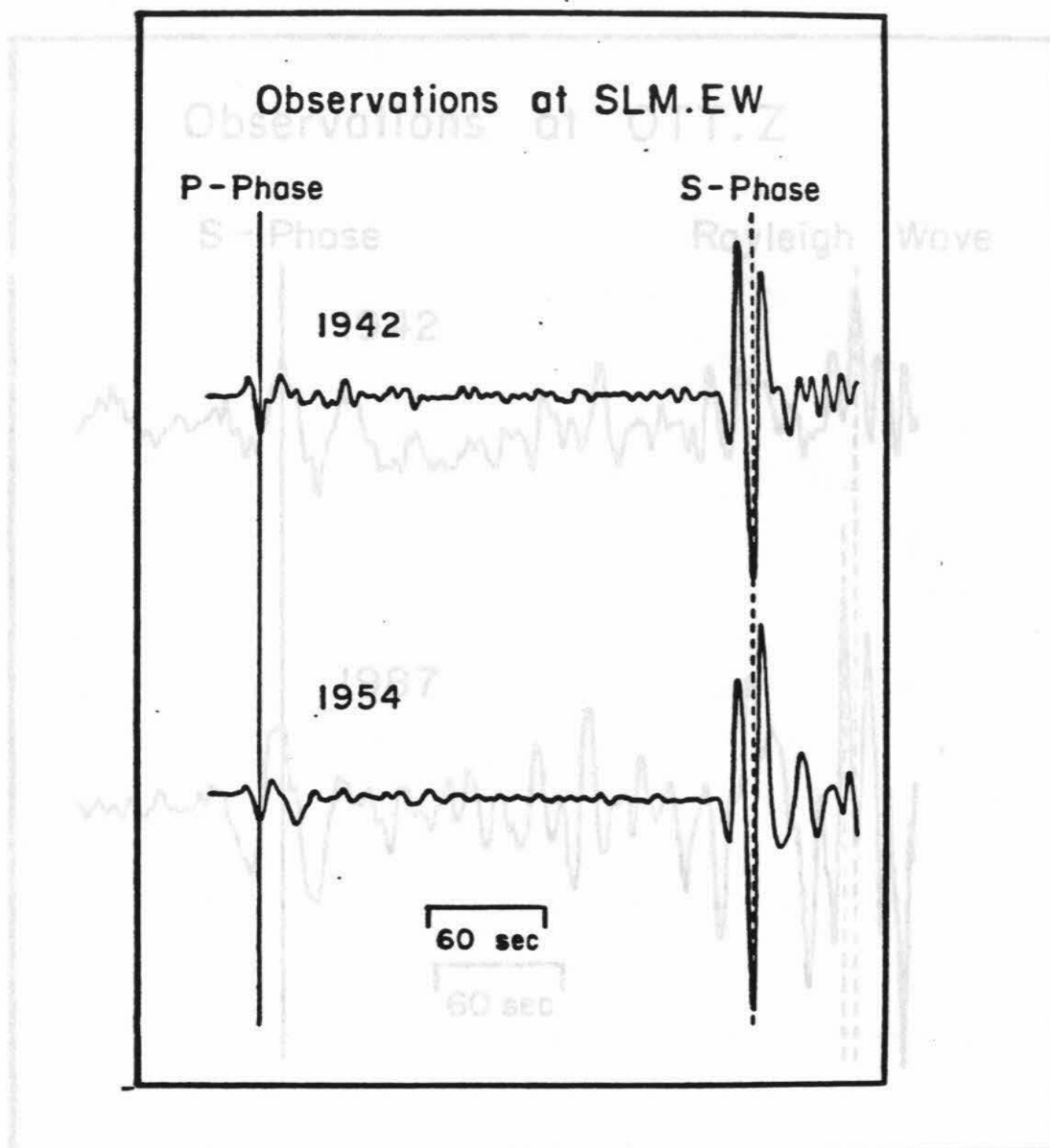


Figure 5.5

EW (radial) component of body waves for the 1942 and 1954 events recorded at SLM. The offset is determined as in previous figures. The spatial offset is determined from the offset of the dashed lines.

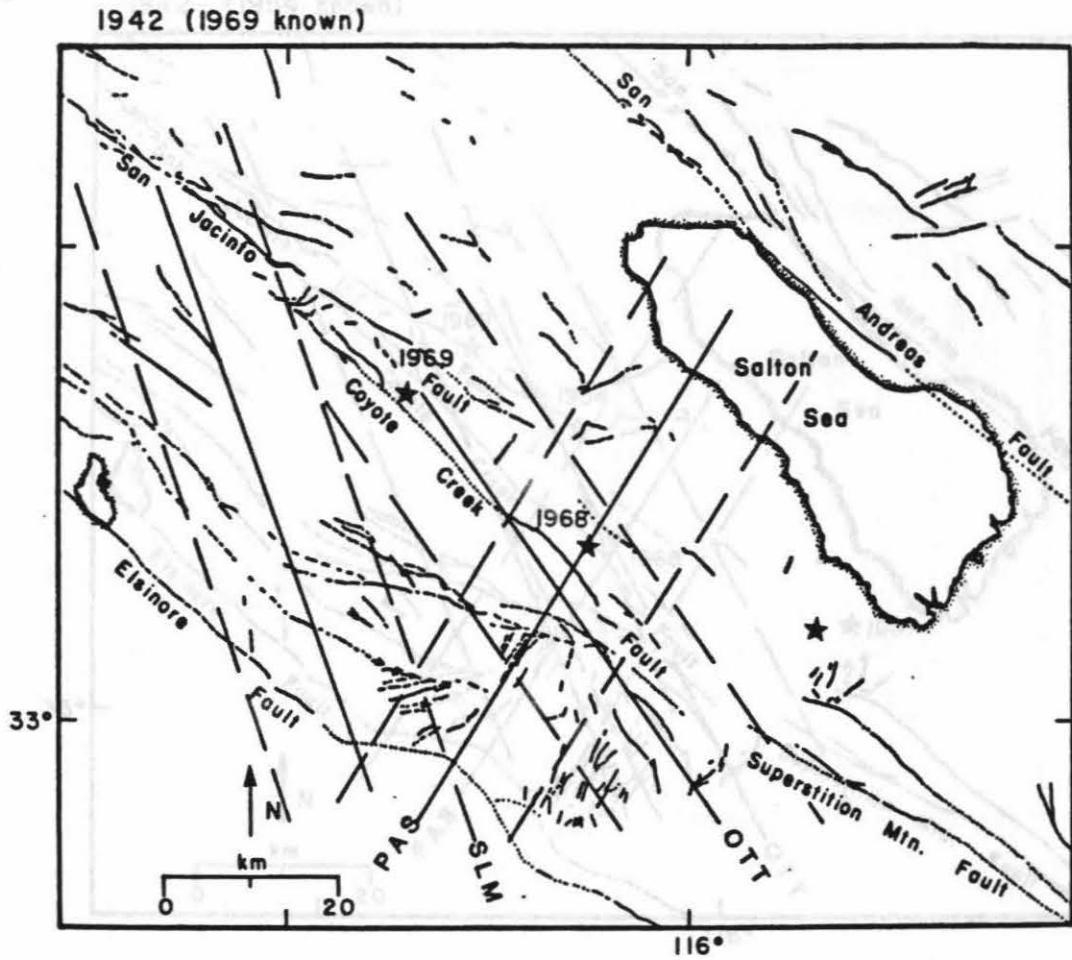


Figure 5.7a

Map showing the results of the relocation of the 1942 earthquake assuming the 1969 event was correctly located. The dashed lines indicate the uncertainty.

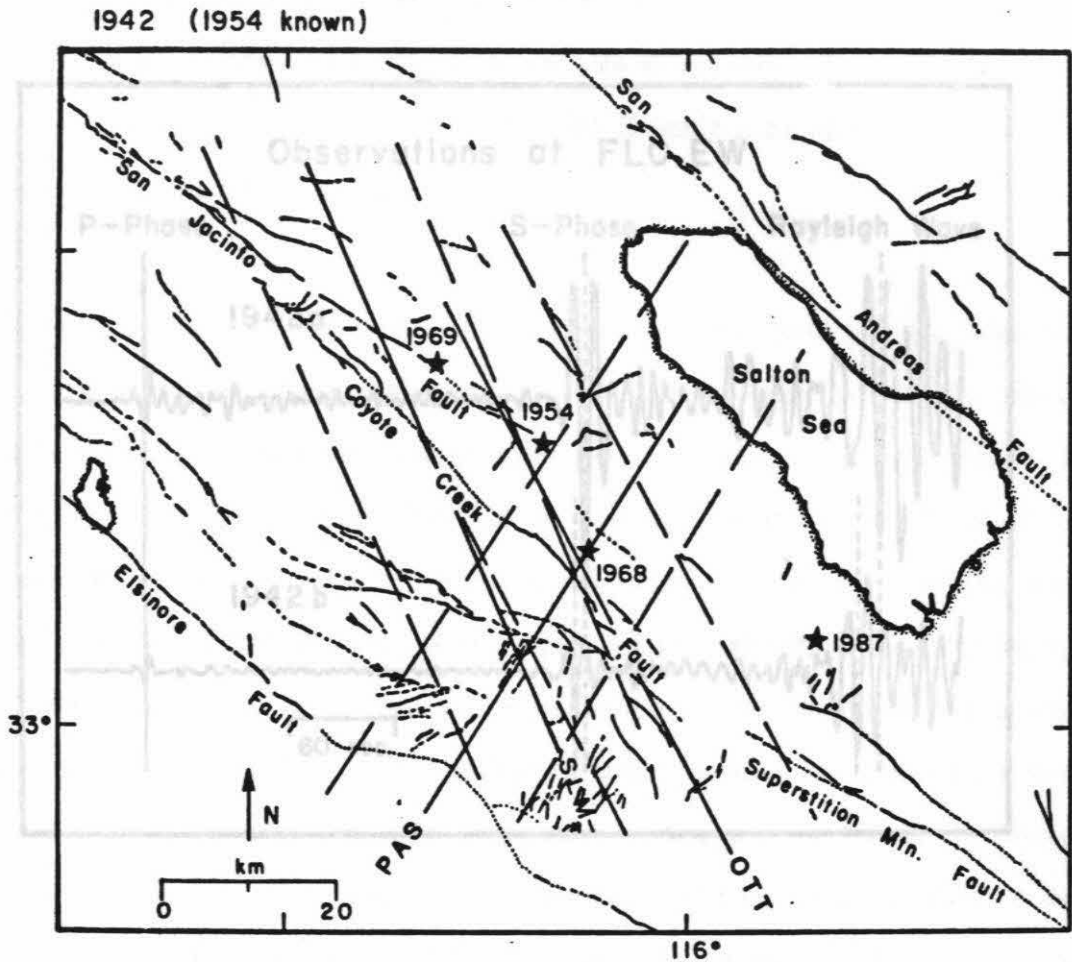
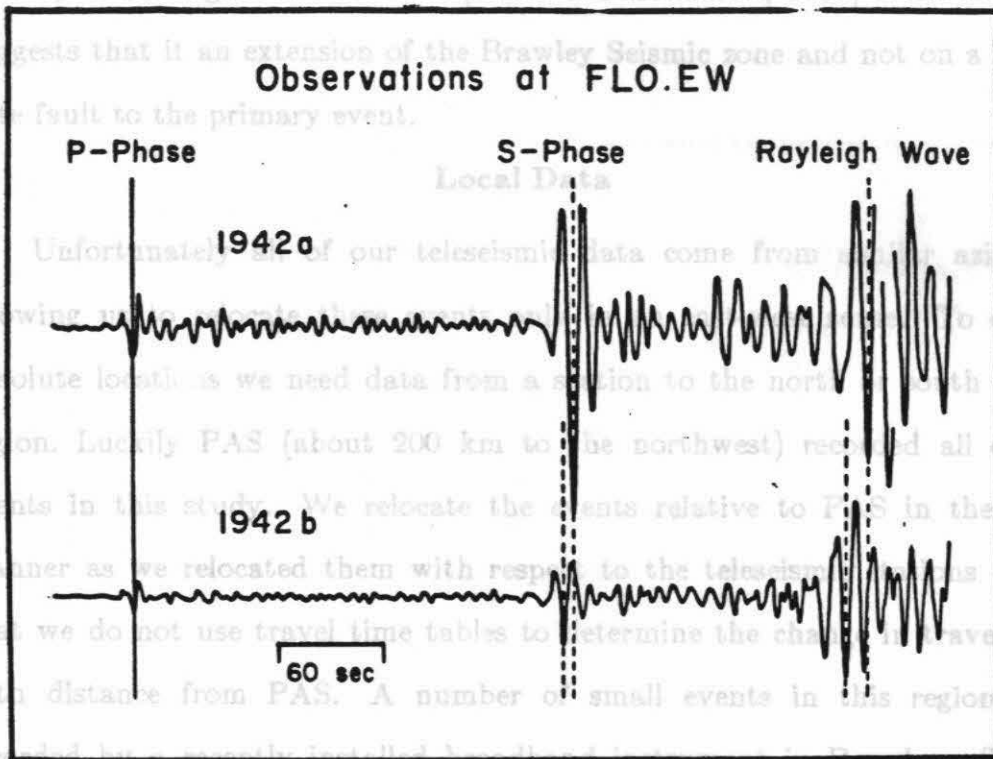


Figure 5.7b

Map showing the results of the relocation of the 1942 earthquake assuming that the 1954 event was correctly located.

aftershock zone of the first event is rather diffuse [Sanders et al., 1986] and there are few aftershocks located for the second event. A plot of recent activity in the region of the 1942b [Dozer and Kanamori, 1986] event however, suggests that it an extension of the Brawley Seismic zone and not on a conjugate fault to the primary event.



Unfortunately, our teleseismic data come from a wide azimuth allowing us to determine the location of the events. To obtain absolute locations we need data from a station to the north and south of the region. Luckily PAS (about 200 km to the northwest) recorded all of the events in this study. We relocate the events relative to PAS in the same manner as we relocated them with respect to the teleseismic stations except that we do not use travel time tables to determine the change in travel time with distance from PAS. A number of small events in this region were recorded by a nearby station that is well instrumented in Pasadena (Figure

5.1). These events were used to calibrate the S-P time as a function of distance from Pasadena. The calibration curve is shown in Figure 5.9. The larger events were then added to this curve. The 1968 and 1987 events lie on the curve suggesting that their locations with respect to PAS are good. The

Figure 5.8

EW (radial) component of the 1942 earthquakes recorded at FLO. Spatial separation is determined from both the S-P and R-S times.

The 1954 event also lies to the right of the curve but to a lesser extent than the 1969 event. The 1942 event lies close to but to the left of the curve suggesting that it should be located closer to PAS. The PAS locations combined with the teleseismic results are shown in Figures 5.7a, 5.7b and 5.10.

aftershock zone of the first event is rather diffuse [Sanders et al., 1986] and there are few aftershocks located for the second event. A plot of recent activity in the region of the 1942b [Doser and Kanamori, 1986] event however, suggests that it is an extension of the Brawley Seismic zone and not on a conjugate fault to the primary event.

Local Data

Unfortunately all of our teleseismic data come from similar azimuths allowing us to relocate these events only in an east-west sense. To obtain absolute locations we need data from a station to the north or south of the region. Luckily PAS (about 200 km to the northwest) recorded all of the events in this study. We relocate the events relative to PAS in the same manner as we relocated them with respect to the teleseismic stations except that we do not use travel time tables to determine the change in travel time with distance from PAS. A number of small events in this region were recorded by a recently installed broadband instrument in Pasadena (Figure 5.1). These events were used to calibrate the S-P time as a function of distance from Pasadena. The calibration curve is shown in Figure 5.9. The larger events were then added to this curve. The 1968 and 1987 events lie on the curve suggesting that their locations with respect to PAS are good. The 1969 event is located noticeably to the right of the curve implying that the earthquake occurred further from PAS than indicated by the catalog location. The 1954 event also lies to the right of the curve but to a lesser extent than the 1969 event. The 1942 event lies close to but to the left of the curve suggesting that it should be located closer to PAS. The PAS locations combined with the teleseismic results are shown in Figures 5.7a, 5.7b and 5.10.

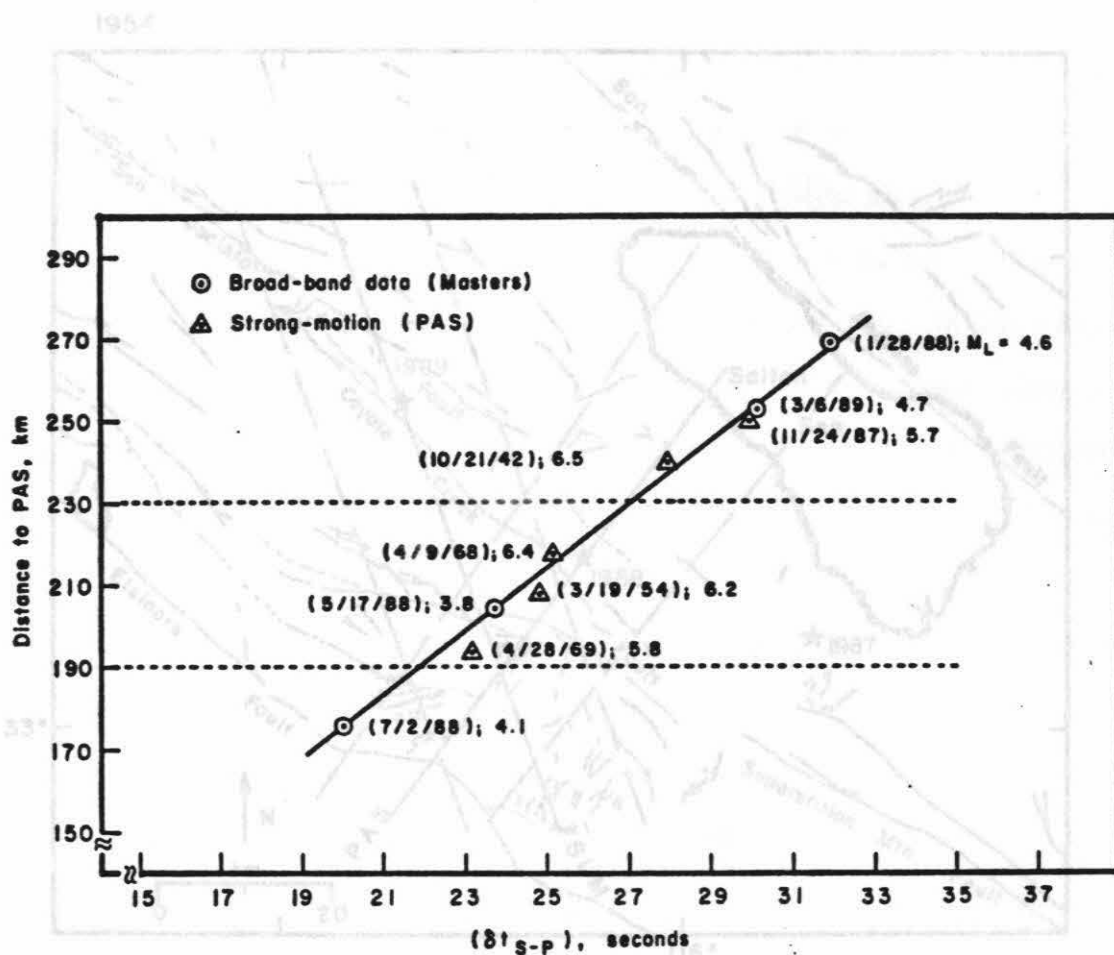
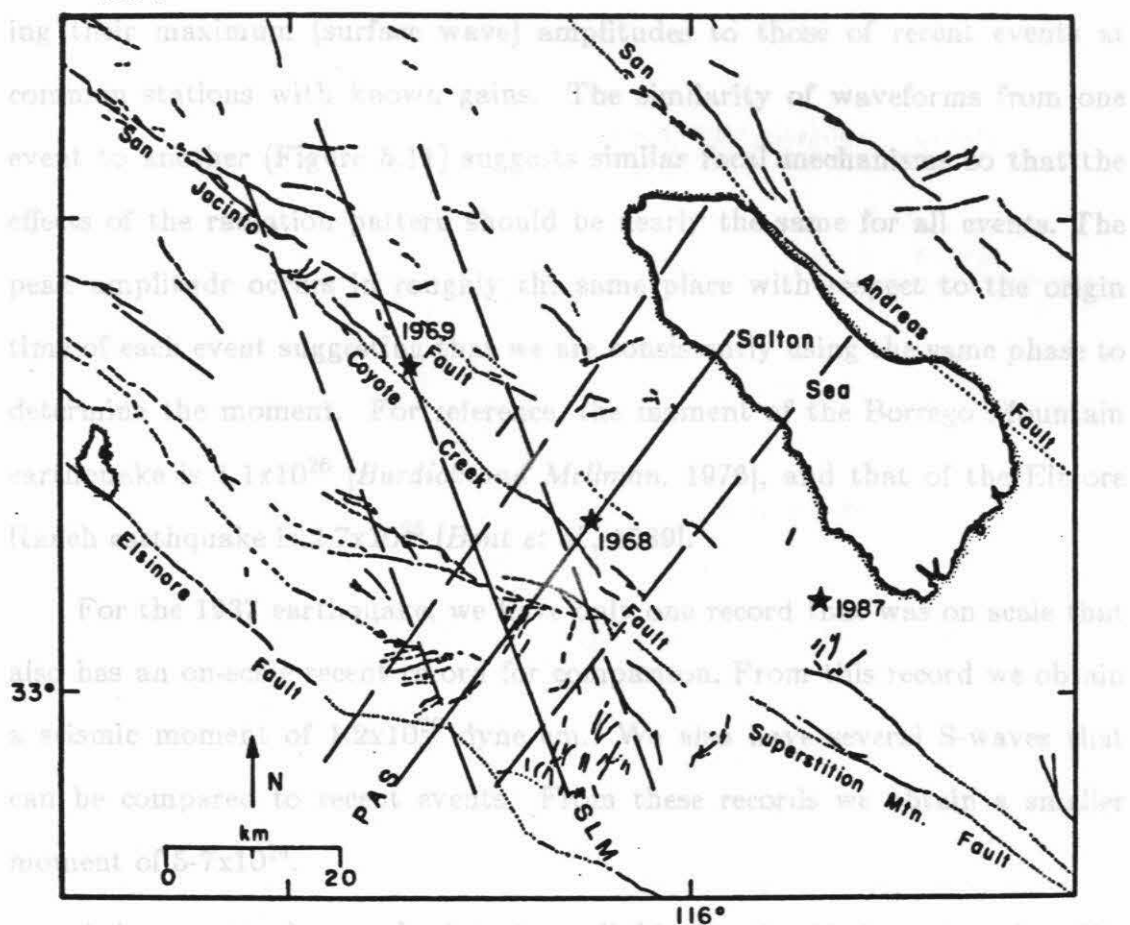


Figure 5.9

Calibration curve for variations in S-P time with distance from PAS. Events used in the calibration are shown as circles. Other events are shown as triangles.

5.4 Moment Estimates

We obtained moment estimates for the historic earthquakes by comparing



A larger volume of on-scale data is available for the 1942 earthquake. We obtain a moment of 3.3×10^{25} , which is about 1/3 that of the 1968 Borrego Mountain event.

Figure 5.10
Map showing the results of the location of the 1954 earthquake.

Some previous estimates had suggested that the magnitude of 6.3 in the Caltech catalog while that of the Borrego Mountain event is 6.4. Other studies however, give the 1942 and 1968 magnitudes as 6.3 [Sandrey et al., 1966] and 6.8 [Kanamori and Jennings, 1973] and are in better agreement with our moment estimates.

Although the secondary 1942 event is relatively small, we have a lot of amplitude data because in addition to comparing it with recent events we can

5.4 Moment Estimates

We obtained moment estimates for the historic earthquakes by comparing their maximum (surface wave) amplitudes to those of recent events at common stations with known gains. The similarity of waveforms from one event to another (Figure 5.11) suggests similar focal mechanisms so that the effects of the radiation pattern should be nearly the same for all events. The peak amplitude occurs in roughly the same place with respect to the origin time of each event suggesting that we are consistently using the same phase to determine the moment. For reference, the moment of the Borrego Mountain earthquake is 1.1×10^{26} [Burdick and Mellman, 1976], and that of the Elmore Ranch earthquake is 2.7×10^{25} [Bent et al., 1989].

For the 1937 earthquake, we have only one record that was on scale that also has an on-scale recent record for comparison. From this record we obtain a seismic moment of 1.2×10^{25} dyne cm. We also have several S-waves that can be compared to recent events. From these records we obtain a smaller moment of $5-7 \times 10^{24}$.

A larger set of on-scale data is available for the 1942 earthquake. We obtain a moment of 3.3×10^{25} , which is about 1/3 that of the 1968 Borrego Mountain event. Some previous magnitude estimates had suggested that the 1942 event was larger. The 1942 earthquake has an estimated M_L of 6.5 in the distance from PAS. To equalize the frequency content of the records, those Caltech catalog while that of the Borrego Mountain event is 6.4. Other studies however, give the 1942 and 1968 magnitudes as 6.3 [Sanders et al, 1986] and 6.8 [Kanamori and Jennings, 1978] and are in better agreement with our moment estimates.

Although the secondary 1942 event is relatively small, we have a lot of amplitude data because in addition to comparing it with recent events we can

also compare the amplitudes to the first 1942 event at stations for which the gain is unknown, assuming that we have an accurate estimate for the first event. We obtain a moment of 1.5×10^{23} suggesting that the magnitude is larger than the Caltech catalog magnitude of 5.5.

A good data set is also available for the 1954 earthquake. We obtain a moment of 1.9×10^{23} dyne cm. The expected size of this earthquake is about that of the 1987 event, but the high-frequency attenuation suggests that it may be smaller.

5.5 Discussion and Conclusions

Our relocated epicenters based on the combined PAS and teleseismic results are shown in Figure 5.11. We obtain a location 15 km east of the catalog location and tentatively place it on the southern end of the Coyote Creek fault. The 1954 earthquake remains at or slightly south and west of the catalog location, but may have had a significant amount of long-period

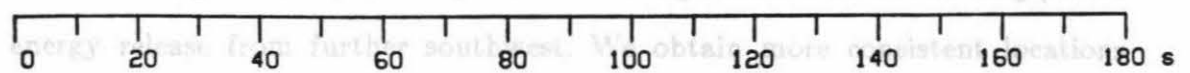


Figure 5.11

North-south component of the Pasadena records shown in order of increasing distance from PAS. To equalize the frequency content of the records, those recorded on short-period instruments were convolved with a long-period instrument response and vice versa.

potential seismic gap on the northern end of the Coyote Creek fault, it would be desirable to use some additional stations to decrease the uncertainty in relocating this event. With the current data set the original location is within the uncertainty of the relocated epicenter.

also compare the amplitudes to the first 1942 event at stations for which the gain is unknown, assuming that we have an accurate estimate for the first event. We obtain a moment of 1.5×10^{25} suggesting that the magnitude is larger than the Caltech catalog magnitude of 5.5.

A good data set is also available for the 1954 earthquake. We obtain a moment of 1.9×10^{25} dyne cm. The expected size of this earthquake is about that of the 1987 event, but the moment determination suggests that it may be smaller.

5.5 Discussion and Conclusions

Our relocated epicenters based on the combined PAS and teleseismic results are shown in Figure 5.12. We move the 1942 event north and east of the catalog location and tentatively place it on the southern end of the Coyote Creek fault. The 1954 earthquake remains at or slightly south and west of the catalog location, but may have had a significant amount of long-period energy release from further southwest. We obtain more consistent locations teleseismically for the historic events if we move the 1969 event to the San Jacinto fault. There were an approximately equal number of aftershocks of the Coyote Mountain earthquake on both the Coyote Creek and San Jacinto faults [Thatcher and Hamilton, 1973] suggesting that a location on the San Jacinto fault is possible. Because moving the Coyote Mountain earthquake to the San Jacinto fault results in a potential seismic gap on the northern end of the Coyote Creek fault, it would be desirable to use some additional stations to decrease the uncertainty in relocating this event. With the current data set the original location is within the uncertainty of the relocated epicenter.

Our error bars from long-period teleseismic data are about the same as those from local short-period data. These results suggest that, at least for earthquakes recorded by only a few local stations, the events can be equally well located by long-period teleseismic data and by local array data. For some historic events the teleseismic data may provide better azimuthal coverage and therefore better locations. Since we are measuring the relative timing of phases, we can avoid the problems that occur in trying to pick the absolute arrival times of phases coming from the Imperial Valley. One source of uncertainty may be the dispersive nature of Rayleigh waves. What appears to be an offset in time could actually be due to a phase difference. However, the source separations of the earthquakes are very small with respect to the total distance traveled and the part of the wavetrain we are using to determine the offset is not noticeably dispersive so this effect should not be significant. The problems associated with dispersion could be avoided by using only body waves, but many of the older instruments had low magnifications which resulted in P waves too small to time accurately.

The 1968 Borrego Mountain earthquake was the largest event to have occurred in the western Imperial Valley since the 1930's based on our moment calculations. The 1942 event was the second largest, with a seismic moment roughly 1/3 that of the 1968 event. The 1987 Elmore Ranch earthquake was third largest of the events studied. The 1937, 1942b and 1954 earthquakes all have similar moments suggesting that the 1937 and 1954 events are smaller than previously assumed and the 1942b event is significantly larger. The 1969 earthquake had the smallest moment of the events studied.

The similarity of waveforms from one event to another suggest that all have similar source mechanisms. Recent well-studied events in this region all

exhibit either right-lateral slip on northwest striking faults or left-lateral slip on northeast striking faults, both of which have the same radiation patterns teleseismically, so it is not surprising that the historic events look similar. Without better azimuthal coverage we cannot obtain exact fault plane solutions or source time functions for the historic events.

Summary

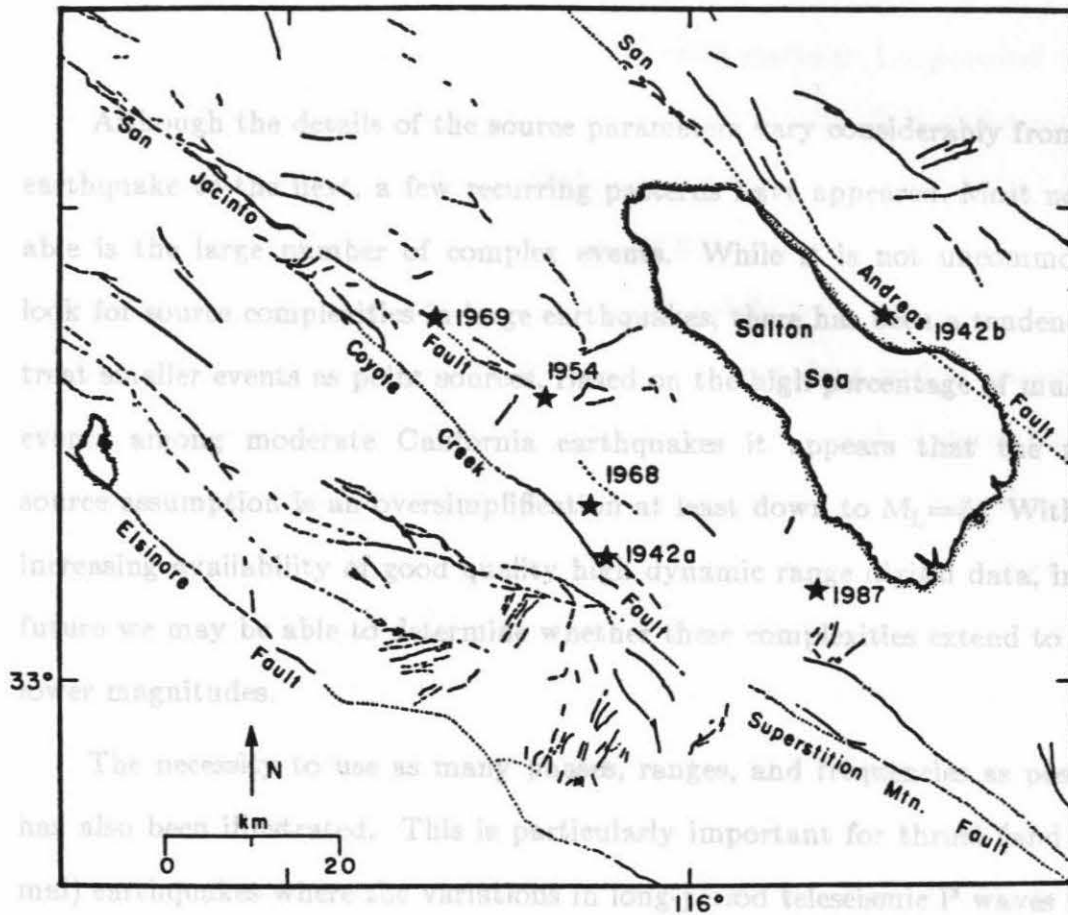


Figure 5.12

Relocated epicenters for the earthquakes in this study.

While the details of the source parameters vary considerably from one earthquake to another, a few recurring parameters appear to be feasible. While the largest number of complex events is not known, it is not unreasonable to look for more complex events. The percentage of multiple events in moderate California earthquakes appears that the point source assumption is a oversimplification. Most down to $M_L = 0$. With the increasing availability of good dynamic range data, in the future we may be able to determine whether our estimates extend to even larger magnitudes.

The necessity to use as many phases, ranges, and stations as possible has also been stressed. This is particularly important for the short-period waves where the variations in long-period teleseismic P waves from one station to another are negligible. Local first motion focal mechanisms, while useful as starting points, can be misleading in cases where the first subsequent is not the largest. For determining the focal mechanism, P₂ waves have proven to be the most useful. SH waves, when not obscured by PL waves, help provide tighter constraints. For depth determination, teleseismic waves provide the most information. Short-period waves are necessary to constrain the source time history. To determine the seismic moment it is desirable to use as many phases and records as possible.

Summary

Although the details of the source parameters vary considerably from one earthquake to the next, a few recurring patterns have appeared. Most noticeable is the large number of complex events. While it is not uncommon to look for source complexities in large earthquakes, there has been a tendency to treat smaller events as point sources. Based on the high percentage of multiple events among moderate California earthquakes it appears that the point source assumption is an oversimplification at least down to $M_L=5$. With the increasing availability of good quality high dynamic range digital data, in the future we may be able to determine whether these complexities extend to even lower magnitudes.

The necessity to use as many phases, ranges, and frequencies as possible has also been illustrated. This is particularly important for thrust (and normal) earthquakes where the variations in long-period teleseismic P waves from one station to another are negligible. Local first motion focal mechanisms, while useful as starting points, can be misleading in cases where the earthquake consists of subevents with different focal mechanisms especially if the first subevent is not the largest. For determining the focal mechanism, P_{nl} waves have proven to be the most useful. SH waves, when not obscured by PL waves, help provide tighter constraints. For depth determination, teleseismic waves provide the most information. Short-period waves are necessary to constrain the source time history. To determine the seismic moment it is desirable to use as many phases and records as possible.

The source parameters for historic earthquakes with sparse data sets can be determined by comparing the waveforms and amplitudes to recent well studied events which were recorded at the same stations. Long-period waves are not traditionally used in earthquake locations because it is easier to accurately pick the start times using short-period records. Although start times are sometimes difficult to measure on long-period records, the difference between two phases can be determined with much more precision. By calibrating travel time differences to well located events, long-period records can be used to locate historic earthquakes within the same level of uncertainty as the short-period locations. Relocating southern California earthquakes using teleseismic data has proven interesting and shown that it can be done. For regions of the world that had no seismic stations in the past, teleseismic records may be the only method by which to study historic earthquakes.

South-central California is dominated by thrust faulting on roughly east-west trending faults implying that the stress field is dominated by north-south compression. The offshore region does not exhibit San Andreas type behavior, but rather seems to be an extension of the Transverse Ranges. The Imperial Valley region, as expected, is dominated by strike-slip faulting on northwest trending faults. This type of behavior is also consistent with north-south compression.

Cipar, J., Broadband time domain modeling of earthquakes from Friuli, Italy. *Bull. Seism. Soc. Am.*, 71, 1215-1231, 1981.

Colla, S. N., T. Hong, and D. V. Helmberger, The Oroville earthquakes: A study of source characteristics and site effects. *J. Geophys. Res.*, 87, 4583-4594, 1982.

Corbett, F. J., Seismicity and crustal structure studies of southern California:

References

- Ben-Menahem, A., S. W. Smith, and T. L. Teng, A procedure for source studies from spectra of long-period seismograms, *Bull. Seism. Soc. Am.*, **55**, 203-235, 1965.
- Bent, A. L. and D. V. Helmberger, Source complexity of the October 1, 1987 Whittier Narrows earthquake, *J. Geophys. Res.*, **94**, 9548-9556, 1989.
- Bent, A. L., D. V. Helmberger, R. J. Stead, and P. Ho-Liu, Waveform modeling of the November 1987 Superstition Hills earthquakes, *Bull. Seism. Soc. Am.*, **79**, 500-514, 1989.
- Boatwright, J., A spectral theory for circular seismic sources: Simple estimates of source dimension, dynamic stress drop, and radiated seismic energy, *Bull. Seism. Soc. Am.*, **70**, 1-27, 1980.
- Burdick, L. J. and D. V. Helmberger, The upper mantle P velocity structure of the western United States, *J. Geophys. Res.*, **83**, 1699-1712, 1978.
- Burdick, L. J. and G. R. Mellman, Inversion of body waves from the Borrego Mountain earthquake to the source mechanism, *Bull. Seism. Soc. Am.*, **66**, 1485-1499, 1976.
- Byerly, P., The California earthquake of November 4, 1927, *Bull. Seism. Soc. Am.*, **20**, 53-66, 1930.
- Choy, G. L., Source parameters of the Coalinga, California earthquake of May 2, 1983 inferred from broadband body waves, *USGS Open-File Rep. 83-511*, 83-131, 1983.
- Cipar, J., Broadband time domain modeling of earthquakes from Friuli, Italy, *Bull. Seism. Soc. Am.*, **71**, 1215-1231, 1981.
- Cohn, S. N., T. Hong, and D. V. Helmberger, The Oroville earthquakes: A study of source characteristics and site effects, *J. Geophys. Res.*, **87**, 4585-4594, 1982.
- Corbett, E. J., Seismicity and crustal structure studies of southern California:

- Tectonic implications from improved earthquake locations, *Ph. D. thesis*, California Institute of Technology, 231 pp., 1984. *Am.*, 79, 515-541, 1980.
- Corbett, E. J. and C. E. Johnson, The Santa Barbara earthquake of 13 August 1978, *Bull. Seism. Soc. Am.*, 72, 2201-2226, 1982. *Imperial Valley, California, earthquake of October 15, 1979, U. S. Geol. Surv. Prof. Pap.*
- Davis, T. L. and K. Hayden, A retrodeformable cross section across the Los Angeles basin and implications for seismic risk evaluation (abstract), *Eos* *Trans. AGU*, 68, 1502, 1988. *Body waves, J. Geophys. Res.*, 67, 5279-5291, 1982.
- Doser, D. I., and H. Kanamori, Spatial and temporal variations in seismicity in the Imperial Valley (1902-1984), *Bull. Seism. Soc. Am.* 76, 421-438, 1986. *Calif. Div. of Mines and Geology, Special Report 137*, 45-55, 1978a.
- Eaton, J. P., Regional seismic background of the May 2, 1983 Coalinga earthquake, *USGS Open-File Rep. 83-511*, 44-60, 1983.
- Eaton, J. P., The May 2, 1983 Coalinga earthquake and its aftershocks: A detailed study of the hypocenter distribution and of the focal mechanisms of the larger aftershocks, *USGS Open-File Rep 83-511* 132-201, 1983. *Gutenberg, B. and C. F. Richter, Magnitude and energy of earthquakes. Am.*
- Ebel, J. E. and D. V. Helmberger, P-wave complexity and fault asperities: The Borrego Mountain, California, earthquake of 1968, *Bull. Seism. Soc. Am.*, 72, 413-437, 1982. *San Jacinto, California, earthquake (November 4, 1927; $m=7.3$) and its aftershocks, Bull. Seism. Soc. Am.* 69, 451-482, 1979.
- Ebel, J. E., L. J. Burdick, and G. S. Stewart, The source mechanism of the August 7, 1966 El Golfo earthquake, *Bull. Seism. Soc. Am.*, 68, 1281-1292, 1978. *of the southern California region, Geol. Soc. Am. Bull.*, 86, 1131-1139, 1975.
- Ellsworth, W. L., R. H. Campbell, D. P. Hill, R. A. Page, R. W. Alweine, T. C. Hanks, T. H. Heaton, J. A. Hileman, H. Kanamori, B. Minster, and J. H. Whitcomb, Point Mugu, California, earthquake of 21 February 1973 and its aftershocks, *Science*, 182, 1127-1129, 1973. *Hauksson, E. and L. Jones, The 1987 Whittier Narrows earthquake sequence*
- Frankel, A. and L. Wennerberg, Rupture process of the November 24, 1987 Superstition Hills earthquake determined from strong motion recordings (abstr.), *Seism. Res. Lett.*, 59, 48-49, 1988. *Hauksson, E., L. M. Jones, T. L. Davis, L. K. Hutton, A. G. Bebout, P. A.*
- Frankel, A. and L. Wennerberg, Rupture process of the M_s 6.6 Superstition

- Hills earthquake determined from strong-motion recordings: Application of tomographic source inversion, *Bull. Seism. Soc. Am.*, **79**, 515-541, 1989.
- Fuis, G. S., W. D. Mooney, J. H. Healey, G. A. McMechan, and W. J. Lutter, Crustal structure of the Imperial Valley region, in *The Imperial Valley, California, earthquake of October 15, 1979, U. S. Geol. Surv. Profess. Paper 1254*, 25-50, 1982.
- Futterman, W. I., Dispersive body waves, *J. Geophys. Res.*, **67**, 5279-5291, 1962.
- Gawthrop, W. H., Seismicity and tectonics of the central California coastal region, *Calif. Div. of Mines and Geology, Special Report 137*, 45-55, 1978a.
- Gawthrop, W. H., The 1927 Lompoc, California, earthquake, *Bull. Seism. Soc. Am.*, **68**, 1705-1716, 1978b.
- Geller, R. J. and H. Kanamori, Magnitudes of great shallow earthquakes from 1904 to 1952, *Bull. Seism. Soc. Am.*, **67**, 587-598, 1977.
- Gutenberg, B. and C. F. Richter, Magnitude and energy of earthquakes, *Ann. Geophys. (Rome)*, **9**, 1-15, 1956.
- Hanks, T., The 1927 Lompoc, California, earthquake (November 4, 1927; $m=7.3$) and its aftershocks, *Bull. Seism. Soc. Am.*, **69**, 451-462, 1979.
- Hanks, T. C., J. A. Hileman, and W. Thatcher, Seismic moments of the larger earthquakes of the southern California region, *Geol. Soc. Am. Bull.*, **86**, 1131-1139, 1975.
- Hartzell, S. and D. V. Helmberger, Strong-motion modeling of the Imperial Valley earthquake of 1979, *Bull. Seism. Soc. Am.*, **72**, 571-596, 1982.
- Hauksson, E. and L. Jones, The 1987 Whittier Narrows earthquake sequence in Los Angeles, southern California: Seismological and tectonic analysis, *J. Geophys. Res.*, **94**, 9569-9590, 1989.
- Hauksson, E., L. M. Jones, T. L. Davis, L. K. Hutton, A. G. Brady, P. A. Reasenberg, A. J. Michael, R. F. Yerkes, P. Williams, G. Reagor, C. W.

- Stover, A. L. Bent, A. K. Shakal, E. Etheredge, R. L. Porcella, C. G. Bufe, M. J. S. Johnston, and E. Cranswick, The 1987 Whittier Narrows earthquake in the Los Angeles metropolitan area, *Science*, **239**, 1409-1412, 1988.
- Helmberger, D. V., Theory and application of synthetic seismograms, in *Earthquakes: Observations, Theory and Interpretation*, pp.174-222, Societa Italiana di Fisica, Bologna, Italy, 1983.
- Helmberger, D. V. and G. R. Engen, Modeling the long-period body waves from shallow earthquakes at regional ranges, *Bull. Seism. Soc. Am.*, **70**, 1699-1714, 1980.
- Helmberger, D., G. Engen, and S. Grand, Upper-mantle cross-section from California to Greenland, *J. Geophys.*, **58**, 92-100, 1985.
- Helmberger, D. V., P. G. Somerville, J. P. McLaren, L. J. Burdick, E. Garnerio, A. Bent, and L. S. Zhao, The location and source parameters of the Lompoc, California earthquake of November 4, 1927, to be submitted to *Bull. Seism. Soc. Am.*, 1990.
- Ho-Liu, P. and D. V. Helmberger, Modeling regional Love waves: Imperial Valley to Pasadena, *Bull. Seism. Soc. Am.*, **79**, 1194-1209, 1989.
- Hutton, L. K., C. R. Allen, and C. E. Johnson, Seismicity of southern California: Earthquakes of ML 3.0 and greater 1975 through 1983, *Seismological Lab., California Institute of Technology*, 142 pp., 1985.
- Hwang, L. J., H. Magistrale, and H. Kanamori, Teleseismic source parameters and rupture characteristics of the 24 November 1987, Superstition Hills earthquake, *Bull. Seism. Soc. Am.*, **80**, 43-56, 1990.
- Jeffreys, H. and K. E. Bullen, *Seismological Tables*, British Association for the Advancement of Science, Gray-Milne Trust, London, 1940.
- Kanamori, H. and D. L. Anderson, Theoretical basis of some empirical relations in seismology, *Bull. Seism. Soc. Am.*, **65**, 1073-1095, 1975.
- Kanamori, H. and P. C. Jennings, Determination of local magnitude, M_L ,

- Wald, D. J., from strong-motion accelerograms, *Bull. Seism. Soc. Am.*, **68**, 471-485, 1978.
- Keilis-Borok, V., On estimation of the displacement in an earthquake source and of source dimensions, *Ann. Geofis.*, **12**, 205-214, 1959.
- Langston, C. A., The February 9, 1971 San Fernando earthquake: A study of source finiteness in teleseismic body waves, *Bull. Seism. Soc. Am.*, **68**, 1-29, 1978.
- Langston, C. A. and D. V. Helmberger, A procedure for modelling shallow dislocation sources, *Geophys. J. R. Astron. Soc.*, **42**, 117-130, 1975.
- Lin, J. and R. S. Stein, Coseismic folding, earthquake recurrence, and the 1987 source mechanism at Whittier Narrows, Los Angeles basin, California, *J. Geophys. Res.*, **94**, 9614-9632, 1989.
- Magistrale, H., L. Jones, and H. Kanamori, The Superstition Hills, California, earthquakes of 24 November 1987, *Bull. Seism. Soc. Am.*, **79**, 239-251, 1989.
- Richter, C. F., *Elementary Seismology*, W. H. Freeman and Co., San Francisco CA, 768 pp., 1958.
- Sanders, C., H. Magistrale, and H. Kanamori, Rupture patterns and preshocks of large earthquakes in the southern San Jacinto Fault Zone, *Bull. Seism. Soc. Am.*, **76**, 1187-1206, 1986.
- Satake, K. and P. G. Somerville, Location and size of the 1927 Lompoc, California earthquake from tsunami data, submitted to *Bull. Seism. Soc. Am.*, 1990.
- Thatcher, W. and R. M. Hamilton, Aftershocks and source characteristics of the 1969 Coyote Mountain earthquake, San Jacinto fault zone, *Bull. Seism. Soc. Am.*, **63**, 647-661, 1973.
- Wald, D. J. and P. G. Somerville, Simulation of accelerograms of the 1987 Superstition Hills earthquake sequence, SSA Meeting, May 1988, Honolulu, Hawaii, 1988.

- Wallace, T. C., Long period regional waves, *Ph. D. thesis*, California Institute of Technology, Pasadena CA, 179 pp., 1983.
- Wallace, T. C. and D. V. Helmberger, Determining source parameters of moderate-sized earthquakes from regional waveforms, *Phys. Earth Planet. Interiors*, *30*, 185-196, 1982.
- Wallace, T. C., D. V. Helmberger, and J. E. Ebel, A broadband study of the 13 August 1978 Santa Barbara earthquake, *Bull. Seism. Soc. Am.*, *71*, 1701-1718, 1981.
- Williams, P. L. and H. W. Magistrale, Slip along the Superstition Hills fault associated with the 24 November 1987 Superstition Hills, California, earthquake, *Bull. Seism. Soc. Am.*, *79*, 390-410, 1989.
- Yeh, H. C., Mechanism of the 1927 Lompoc earthquake from surface wave analysis, *M. S. thesis*, University of Washington, Seattle WA, 1975.